

The Fabrication and Physics of High-Efficiency CdTe Thin-Film Solar Cells

**Annual Technical Report for the Period
September 1, 2001 to August 31, 2002**

Contract No. NDJ-1-30630-02

Alvin D. Compaan, principal investigator
Victor Karpov, co-principal investigator
Randy G. Bohn, co-investigator
Dean Giolando, co-investigator

NREL technical monitor: Ken Zweibel

Department of Physics and Astronomy
The University of Toledo
Toledo, OH 43606

Summary

There are three focus areas in this subcontract, cell structure and fabrication, cell modeling and accelerated life testing, and characterization of materials and devices.

Our efforts on cell fabrication have primarily involved the use of magnetron sputtering for deposition. During the first year of this award we have:

- achieved 12.6% efficiency in an all-sputtered cell on Tec-15 soda-lime glass,
- achieved 14.0% efficiency on aluminosilicate glass with sputtered ZnO:Al/CdS/CdTe,
- fabricated 9% cells on Tec-15 glass with CdTe thickness of only 0.68 μm
- related CdTe cell stability to grain boundary morphology controlled by sputter gas pressure,
- fabricated substrate configuration CdTe cells on Mo sheet and on polyimide, and
- showed that electrodeposited cells and sputtered cells optimize with essentially the same vapor CdCl_2 treatment parameters.

In addition, we studied some high-resistivity transparent (HRT) interfacial layers between Tec-15 and CdS, finding high variability and not much improvement for the use of thin CdS layers. We fabricated mixed targets of CdTe and Cd_3P_2 to examine the possibilities for doping of CdTe with phosphorous and found a small increase in carrier concentration but no improvement in cell performance with the mixed targets.

In the focus area of cell modeling we concentrated on nonuniformity effects. We have composed an extensive literature review on nonuniformities in the major thin-film PV technologies, which shows that lateral nonuniformities unambiguously affect thin-film device performance and degradation. Our original physical model relates lateral nonuniformities in a PV cell to that in a random diode array where the diodes are connected in parallel through resistive electrodes. The key parameters of the model are estimated in the terms of underlying semiconductor nonuniformities. Based on our new understanding we have suggested an explanation of the observed integral device properties, such as voltage, current, I/V characteristics, and fluctuations in the main photovoltaic parameters. We have also developed software to numerically model lateral nonuniformity effects in PV cells, including random parameter distributions, local fluctuations in current and voltage, and integral I/V characteristics. This software will be made available to the photovoltaic community soon. In addition, the results of our modeling suggested specific nontrivial ways of blocking the effect of nonuniformities, which are being implemented. In verifying our understanding we have observed several novel effects. One of them is the nonuniform degradation where we have shown that degradation is a bias-driven (not a directly light-driven) effect and that it evolves differently in different parts of the device. One other effect is nonlocal photovoltaic response, in which the device develops photovoltage far away from the laser beam spot. This effect was shown to become a potentially useful tool in nondestructive TCO characterization.

In the focus area of characterization we have continued our studies of light emission from completed devices using mainly photoexcitation for photoluminescence (PL) but also with current injection for electroluminescence (EL). Our electroluminescence studies have concentrated on low drive levels using direct photomultiplier detection. We have studied a variety of materials and devices ranging from ion-implanted crystals of CdTe to polycrystalline films made by vapor transport deposition (VTD), close-spaced sublimation, and magnetron sputtering as part of the National CdTe Team efforts. We have performed PL mapping studies on fresh and light-soaked cells, studied the degradation of “fatigue” of the PL signal during laser exposure, and participated in PL studies of VTD cells light-soaked under various temperature and bias conditions. Finally, we have: performed Hall measurements to characterize sputtered ZnO:Al, used admittance spectroscopy of VTD and sputtered cells over a wide frequency range, studied Cu k_α absorption edge spectroscopy with the Advanced Photon Source at Argonne, and compared laser scribing of stannate films with other TCOs. Much of this report covers work in progress and is therefore not complete. These efforts continue in Phase Two of this Contract.

Table of Contents

Cover page	
Summary	ii
Table of Contents	iii
List of Figures	v
List of Tables	vii
1. Introduction	
1.1 Background	1
1.2 Objectives of this subcontract	1
1.3 Technical Approach	1
2. Cell structure and fabrication	
2.1 12.6% sputtered cell on Tec-15 glass	3
2.2 14.0% sputtered cell with sputtered ZnO:Al for TCO	4
2.3 CdTe grain boundary morphology effect on cell stability	6
2.4 Substrate-configuration cells fabricated on Mo and Kapton	8
2.5 CdS/CdTe cells with HRT layers	10
2.6 Cells with varying thickness of CdTe	13
2.7 Doping studies of CdTe by reactive sputtering from CdTe/Cd ₃ P ₂	15
2.8 Chloride treatments and back contacts on electrodeposited CdTe	20
2.9 References (Section 2)	24
3. Cell modeling	
3.1 Lateral nonuniformities: survey and analytical results	25
3.1.1 Survey of mesoscale nonuniformity observations	25
3.1.2 Understanding laterally nonuniform devices	27
3.1.3 Mesoscale effects of micrononuniformities	29
3.1.4 Blocking the effects of nonuniformities	31
3.2 Numerical modeling of laterally nonuniform devices	32
3.2.1 Model	33
3.2.2 Model parameters	33
3.2.3 Numerical algorithm	34
3.2.4 Running the program	35
3.2.5 Examples	37
3.3 Nonuniform degradation	40
3.4 Nonlocal photovoltaic response	41
3.5 Conclusion	44
3.6 References (Section 3)	45
4. Characterization of materials and devices	
4.1 Photo- and electro-luminescence studies	47
4.1.1 PL mapping	47
4.1.2 PL decay measurements	52
4.1.3 Ion implantation and PL studies of CdTe	54

4.1.4	Defect chemistry studies	56
4.1.5	Electroluminescence at low drive levels and low temperature	61
4.2	Deposition and characterization of ZnO:Al	64
4.3	Admittance spectroscopy	65
4.4	Synchrotron x-ray studies of CdTe films	65
4.5	Laser scribing of stannate films	67
4.6	References (Section 4)	69
5.	Publications	
5.1	Refereed papers published or in press 9/1/01—8/31/02	71
5.2	Poster or oral presentations published on CDROM or Web site	71
5.3	Contributed oral or poster presentations (unpublished)	71
5.4	Annual subcontract summary	72
6.	Project personnel	
6.1	Faculty	73
6.2	Research professors	73
6.3	Postdoctoral Associates	73
6.4	Graduate students	73
6.5	Undergraduate students	74
6.6	Technical assistants	74

List of Figures

Fig. 2.1.1	I-V curve for sputtered cell (980A2#5) showing 12.6% efficiency at AM1.5	4
Fig. 2.1.2	QE curve for sputtered cell (980A2#5).....	4
Fig. 2.2.1	a) I-V tests of CdS/CdTe cell with ZnO:Al TCO b) Quantum efficiency of this cell ...	5
Fig. 2.3.1	SEM of CdTe films deposited with 10, 18 and 50 mTorr of gas pressure	6
Fig. 2.3.2	Parameter degradations of CdTe solar cells sputtered at different gas pressures	7
Fig. 2.4.1	Sketch of grain structure in superstrate (a) and substrate (b) cells	9
Fig. 2.4.2	Q-E response for substrate cells on Mo with different CdS layer thickness	9
Fig. 2.4.3	I-V curve of a 7.8% efficient cell with the structure Mo/ZnTe:N/CdTe/CdS/ITO	9
Fig. 2.5.1	I-V curves of cells with different HRT types and two different CdS thicknesses	10
Fig. 2.5.2	Comparison of I-V curves of devices prepared on HRTs.....	11
Fig. 2.5.3	Comparison of QE for devices with thin and thick CdS on HRTs	11
Fig. 2.6.1	Transmission through cell structures with different CdTe thicknesses	13
Fig. 2.6.2	Spectral quantum efficiencies of solar cells with different CdTe thicknesses.....	13
Fig. 2.6.3	Cell parameters (V_{OC} , I_{SC} , FF, Eff.) vs. CdTe thickness before and after light soak...14	
Fig. 2.7.1	Comparative I-V plots for devices made from home-made and commercial CdTe targets	
Fig. 2.7.2	I-V plots of devices from CdTe:P, Cerac, and home-made targets; Au-only contacts17	
Fig. 2.8.1	(a) Light and dark I-Vs of electrodeposited cells with UT contacts (b) comparison of QE between electrodeposited and sputtered devices	21
Fig. 3.1	Top: equivalent circuit of random microdiodes; Bottom: equivalent two-diode circuit and I/V characteristics of the weak diode	27
Fig. 3.2	Simulated open circuit voltage, electric potential, and transverse electric current distributions in an open-circuit system of random diodes.	29
Fig. 3.3	Equivalent circuit representing laterally nonuniform photovoltaics.....	32
Fig. 3.4	Electric potential distribution in a shunted 1D diode circuit for different resistors.....	34
Fig. 3.5	Data Flow and execution in the computer program solving a random diode circuit...36	
Fig. 3.6	Spatial distributions of V_{OC} and V in a linear system of random diodes.....	37
Fig. 3.7	Spatial distributions of V_{OC} fluctuations and electric current in system fo Fig. 3.6....38	
Fig. 3.8	Statistical distribution of recombination currents in linear circuit of random diodes..38	
Fig. 3.9	Equivalent circuit for modeling I/V characteristics of nonuniform photovoltaics	39
Fig. 3.10	Simulated I/V curves of small cells with and without lateral nonuniformities.....	39
Fig. 3.11	Simulated I/V curves of large cells with and without lateral nonuniformities	40
Fig. 3.12	Degradation of different parameters in a set of artificially nonuniform cells.....	41
Fig. 3.13	Setup for measuring voltage vs. distance from the laser beam.....	42
Fig. 3.14	Nonlocal V_{OC} vs. distance from laser beam in 1D cell	42
Fig. 3.15	V_{oc} vs distance from the 2D cell edge	42
Fig. 3.16	V_{oc} spatial decay vs distance from laser beam for dot and linear cells	43
Fig. 3.17	Spatial decay of surface voltage in the case of back wall excitation	43
Fig. 3.18	V_{oc} vs. distance from laser beam for ambient light on and off, sputtered cell.....	43
Fig. 3.19	Same as in Fig. 3.18 for a vapor-transport deposited sample	43
Fig. 3.20	PL maps for two different excitation powers a) 2 sun, and b) 20 sun	44
Fig. 4.1.1	Typical PL spectra (a) and integrated PL intensities (b) for VTD samples.....	48

Fig. 4.1.2	PL scan of “unusual” VTD fresh sample (a) and typical light soaked sample	49
Fig. 4.1.3	Built-in electric field suppression by back-contact (BC) metal in a device with shunting pathways.....	49
Fig. 4.1.3	Built-in electric field suppression by back-contact (BC) metal in a device with shunting pathways.....	49
Fig. 4.1.4	PL mapping of sputtered samples before (a) and after (b) light soak	50
Fig. 4.1.5	PL spectra from CdTe single crystal before and after Cu diffusion	51
Fig. 4.1.6	PL maps of VTD cells with UT contact before (a) and after (b) light soak	51
Fig. 4.1.7	Relative Standard Deviation (SD) for each scan line as a measure of nonuniformity	52
Fig. 4.1.8	Typical PL fatigue from under-contact area for three temperatures	53
Fig. 4.1.9	Normalized PL fatigue in a CdTe solar cell for four temperatures	54
Fig. 4.1.10	Normalized relative degradation PL, EBIC, and solar cell efficiency	54
Fig. 4.1.11	PL at 1.2 mW from crystalline CdTe from regions with and without implantation.....	55
Fig. 4.1.12	Power-dependent PL on $2 \times 10^{13} \text{ cm}^{-2}$ Cu-implanted sample.....	56
Fig. 4.1.13	10K junction PL spectra for VTD samples stressed at different conditions.....	57
Fig. 4.1.14	10K junction PL from cells unstressed; and light-soaked	58
Fig. 4.1.15	Low-temperature PL spectra for sample stressed for different times	59
Fig. 4.1.16	Sketch of a donor-acceptor pair in CdTe	61
Fig. 4.1.17	Sketch of a two-hole transition in CdTe	61
Fig. 4.1.18	Room temperature EL and PL spectra from a CdTe/CdS device	62
Fig. 4.1.19	EL intensity vs current density for a sputtered cell with ZnO TCO	63
Fig. 4.1.20	Exponent b and EL intensity at constant current for VTD and sputtered cells.....	63
Fig. 4.2.1	Resistivity, mobility, and carrier density of an rf-magnetron-sputtered ZnO:Al film.....	65
Fig. 4.2.2	A typical ZnO:Al XRD pattern from an as-deposited, sputtered film.....	65
Fig. 4.4.1	Cu k_{α} fluorescence spectra from a sputtered film, Cu foil, and CdTe target.....	67
Fig. 4.4.2	XANES absorption spectra of Cu foil, CuO, Cu ₂ Te, and a CdTe:Cu film.....	67

List of Tables

Table 2.5.1	IV data of best devices on new HRT (as received HRT).....	10
Table 2.5.2.	IV data of devices on good HRT (C-24).....	10
Table 2.5.3	I-V data of best devices on new HRT heat-treated at 550C	12
Table 2.5.4	IV data of best device on HRT 609/ VTD CdS/ RF sputtered CdTe structure.....	12
Table 2.7.1	I-V data for devices made from commercial and home-made CdTe targets	15
Table 2.7.2	I-V of devices with Au-only contacts prepared from different targets	16
Table 2.7.3	IV data of devices measured during stability study	18
Table 2.8.1	Effect of CdCl ₂ treatment temperature on electrodeposited devices.....	20
Table 2.8.2	Effect of back contact diffusion on electrodeposited devices.....	20
Table 2.8.3	Stress-performance of sputtered and electrodeposited cells	22
Table 4.5.1	Surface damage thresholds for stannates	68
Table 4.5.2	Details on scribe lines in stannate films.....	69

1. Introduction

1.1 Background

The purpose of this subcontract, as part of the R&D Partners Category of the Thin Film Photovoltaics Partnerships Program (TFPPP) of NREL is to 1) extend research efforts on cell structure and fabrication mainly through the use of magnetron sputtering, including absorber layer doping, window and back contact buffer layers, alternative back contacts, and preparation of inverted cell structures; 2) perform CdTe-based cell modeling which goes beyond traditional numerical models to include electric potential and electric current distributions in cells, the effects of nonuniformities in cell performance, and the physics of buffer layers; 3) to extend efforts on materials and device characterization with emphases on the use of photoluminescence (PL) including bias-dependent PL, as well as Hall effect and photo-Hall effect measurements, performed in parallel with current-voltage (I-V) and spectral quantum efficiency (SQE) device measurements; and 4) to support workforce development through the education and training of undergraduate, graduate, and postdoctoral students in the PV area.

This annual report covers the first year of a three year, NREL thin-film partnership subcontract with the University of Toledo which has three task areas: 1) cell structure and fabrication, 2) cell modeling, and 3) characterization of materials and devices.

1.2 Objectives of this subcontract

The primary objectives of this research by this subcontractor as an R&D partner is to address fundamental issues especially related to:

- enhancing the total-area, thin-film cell efficiency through magnetron sputtering of novel materials and alloys,
- improving the understanding of micro-nonuniformities and their impact on device and module performance through novel experiments and modeling,
- improving the understanding of the materials and devices through the use of photoluminescence (PL), capacitance-voltage (CV), Hall and photo-Hall, Raman, absorption, and scanning electron microscopy (SEM) with energy dispersive x-ray spectroscopy (EDS),
- identifying materials and structural issues that can lead to improved cell stability, including interfacial layers and novel back contacts,
- identifying novel device structures to find pathways for reducing the utilization of CdTe, and development of substrate CdTe structures for comparison with standard superstrate devices and to determine possibilities for roll-to-roll manufacturing, and
- strengthening the thin-film PV infrastructure through education and training of undergraduate and graduate students as well as postdoctoral associates.

1.3 Technical Approach

The scope of work under this subcontract is divided into three primary efforts which are reflected in the three following Sections. The *first effort* is focused on the use of magnetron sputtering for fabrication of CdTe-based cell structures. This includes the doping of CdTe during sputtering, the use of interfacial layers in sputtered cell structures, and the fabrication of

(inverted structure) substrate cells on metal or metal-coated glass substrates. The *second effort* is focused on cell modeling. We seek to model quantitatively the effects of two-dimensional non-uniformities in electric potentials and current distributions in thin-film CdTe cells including the effects of buffer, absorber, and window layer parameters. The modeling effort includes comparison with cell and materials measurements, such as described in the third effort. The *third effort* is focused on the characterization of CdTe-based PV materials and devices. This effort includes studies of photoluminescence (PL) and electroluminescence (EL) of magnetron-sputtered (MS) and vapor-transport-deposited (VTD) materials and cells before and after stressing. The effort also includes small-spot PL (PL mapping) on standard cells and bias-dependent PL for direct comparison with the cell modeling efforts. We also have performed Hall, x-ray diffraction, Raman, SEM, capacitance-voltage, and synchrotron x-ray absorption studies on these materials.

2. Cell structure and fabrication

In the first of the three focus areas of this subcontract, cell structure and fabrication, we have made significant advances in the performance of our all-sputtered cells over the past year. First, we have reached 12.6% efficiency on Pilkington Tec-7 substrates (3mm soda-lime glass with $\text{SnO}_2\text{:F}$ and no interfacial layers). Second, we have used sputtered ZnO:Al on Corning 1737 aluminosilicate glass to reach 14.0% efficiency. We have studied also 3) the effects of grain boundary morphology on stability, 4) substrate configuration cells on Mo and on Kapton, 5) cells with HRT (high resistivity transparent) layers, 6) how 10% efficient cells can be fabricated with CdTe layers as thin as 0.68 μm , 7) doping of CdTe by sputtering, and 8) comparisons of chloride treatments on electrodeposited vs. sputtered cells. Each of these is described more fully in the eight subsections below.

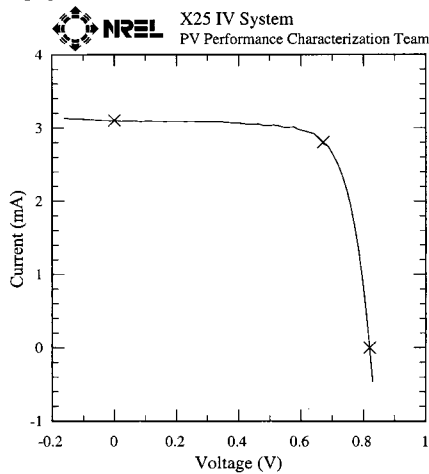
2.1 12.6% sputtered cell on Tec-15 glass

In February, 2002, we forwarded several cells to NREL for testing. These cells were deposited on Pilkington Tec-7 glass substrates. The cells were prepared by our standard process¹ using sputtered CdS, sputtered CdTe, vapor CdCl_2 , and evaporated Cu (3 nm) and Au (20 nm). No interfacial layer was used between the $\text{SnO}_2\text{:F}$ and our sputtered CdS. After the 150°C heat treatment in air for the diffusion of Cu, the CdTe surrounding the 0.15 cm^2 contact was scraped off and the CdS etched off with HCl. Indium was applied to the $\text{SnO}_2\text{:F}$ for the contact to the front electrode.

The best cell performance is given in Figs. 2.1.1 and 2.1.2. The I-V curve (Fig. 2.1.1) gives $V_{\text{OC}} = 820 \text{ mV}$, $J_{\text{SC}} = 20.7 \text{ mA/cm}^2$, and $\text{FF} = 73.96\%$ for an efficiency of 12.6%. This improves on our earlier best cell which was measured at 11.6%.¹ This cell shows improvements in voltage and fill factor that account for the increased performance. The quantum efficiency (Fig. 2.1.2) shows poor conversion below 500 nm due to the CdS layer, which was 130 nm thick as-deposited. We have fabricated cells with decreased CdS thickness and improved QE in this region, but the overall cell performance always decreases. In previous work² with high resistivity interfacial layers, we have seen evidence of improved blue-green performance and high open circuit voltage but the supply of substrates with high quality HRT layers has not been consistent enough to allow us to optimize the process. We will continue these studies as the availability of suitable bi-layer coated substrates improves. Some additional studies of HRT layers were carried out with material supplied by First Solar (See Section 2.5.)

University of Toledo
CdS/CdTe Cell

Device ID: 980A2#5 Device Temperature: 25.0 ± 1.0 °C
Mar 19, 2002 11:46 Device Area: 0.150 cm^2
Reporting Spectrum: AM1.5 Global Irradiance: 1000.0 W/m^2



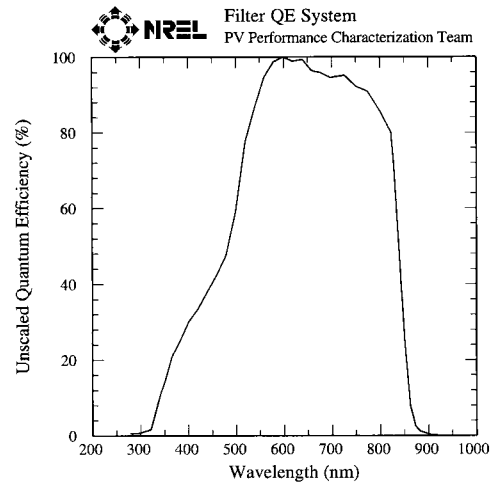
$V_{oc} = 0.8204 \text{ V}$
 $I_{sc} = 3.1036 \text{ mA}$
 $J_{sc} = 20.702 \text{ mA/cm}^2$
Fill Factor = 73.96 %
 $I_{max} = 2.8036 \text{ mA}$
 $V_{max} = 0.6717 \text{ V}$
 $P_{max} = 1.8833 \text{ mW}$
Efficiency = 12.6 %

Storage state.
With conductive rubber to protect cell.

Fig. 2.1.1 I-V curve for sputtered cell (980A2#5) showing 12.6% efficiency at AM1.5.

University of Toledo
CdS/CdTe Cell

Device ID: 980A2#5 Device Temperature: 25.0 ± 1 °C
Feb 28, 2002 12:33 PM Device Area: 0.1499 cm^2



Voltage Bias: 0.0 V
Light bias for 5.06 mA
Light Bias region area: 0.1499 cm^2
Light Bias Density: 33.73 mA/cm^2
 I_{sc} Estimate:
 $I_{sc} \text{ (Global)} = 23.8 \text{ mA/cm}^2$

Fig. 2.1.2 QE curve for sputtered cell (980A2#5).

2.2 14.0% sputtered cell with sputtered ZnO:Al for TCO

During the first year we have developed the capability for rf magnetron sputtering of high quality films of ZnO doped with Al from a target of ZnO:Al₂O₃ (2%). Most of this work was carried out as part of our project under the High Performance PV program and we will not report details of this work here. However, we do report here the use of this doped ZnO:Al as a front window/electrode layer for our sputtered CdS/CdTe cells. We are aware of other attempts to use doped ZnO^{3,4} as a window layer for superstrate CdTe cells, but these reports indicated limited success. It has been suggested that the ZnO deteriorates under subsequent processing steps during the deposition of CdS and/or CdTe, during the subsequent CdCl₂ processing, or perhaps during the back-contact processing. At least part of the ZnO deterioration may be due to the high temperature processing steps (>500°C) needed for most CdTe cell fabrication. Since ZnO:Al can be very transparent and very conductive, and since our fabrication process does not use any temperatures above 390°C, we decided to fabricate an (almost) all-sputtered cell using sputtered ZnO:Al. It was also convenient to use the somewhat more transparent aluminosilicate (Corning 1737) glass for the superstrate.

The Al-doped ZnO front contact/window layer was deposited on aluminosilicate glass by RF magnetron sputtering from a ZnO:Al₂O₃ target. The ZnO:Al film has ~95% average transmission in visible spectrum with ~3 ohm/square sheet resistance. The CdS and CdTe thin

films were also deposited by RF magnetron sputtering following our usual method.¹ Devices were completed with a vapor CdCl₂ treatment at 387 °C and with our usual evaporated Cu (3 nm)/Au (20 nm) back contact. A 30 min diffusion step in air at 150 °C was used after the metallization. No wet chemical or water rinses were used after the initial glass cleaning. No etches of any kind were used.

A device was tested at NREL and an efficiency of 14.0 % was confirmed for this all sputtered CdS/CdTe solar cell. (See Fig. 2.2.1 below.) The improved performance, over the Tec-7/SnO₂:F is almost entirely due to higher current. The ZnO-based cell had J_{SC} of 23.6 mA/cm² compared to 20.7 mA/cm² for our recent 12.6% cell on a commercial SnO₂:F TCO substrate. (See Section 2.1 above.) Other parameters of the 14% ZnO-based cell are: FF = 73.25% and V_{OC} = 814 mV. We believe that this is the first time that ZnO has been used very successfully as a window layer for CdS/CdTe thin film solar cells. The key to using the ZnO:Al appears to be to keep the temperature of the subsequent processing steps low enough, in our case, below 390 °C.

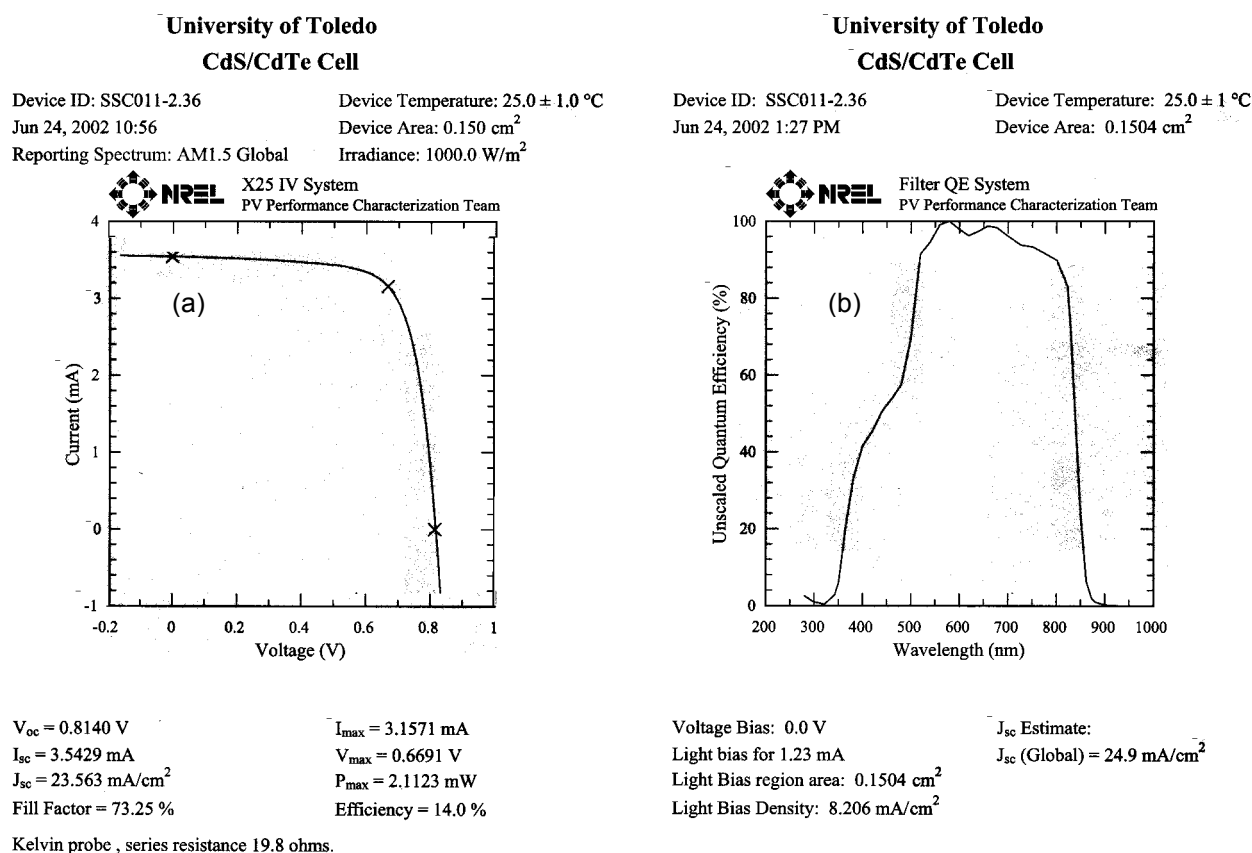
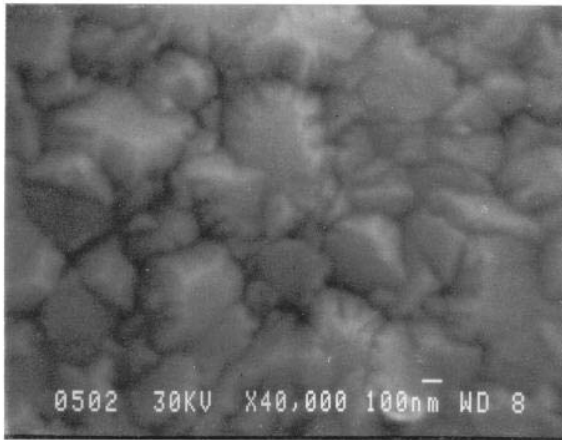


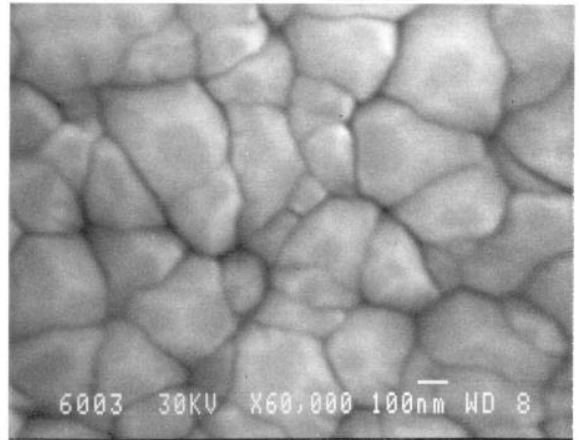
Fig. 2.2.1 a) I-V tests of CdS/CdTe cell (# SSC011-2.36) with ZnO:Al TCO (all layers sputtered) with evaporated Cu/Au back contacts. b) Quantum efficiency of this cell.

2.3 CdTe grain boundary morphology effect on cell stability

The sputter gas pressure has considerable effect on the grains and grain boundaries of CdTe. Figure 2.3.1 shows the SEM of CdTe films deposited at 10, 18 and 50 mTorr gas pressure. Changes in CdTe grain morphology with pressure have been discussed previously,⁵ and some changes in initial cell performance have been noted. However, we have not previously studied the effect of these grain morphology differences on the long-term stability of the CdTe cells. Note from Fig. 2.3.1 that the grain boundaries are much more compact at lower sputter gas pressure. This results from increased ion bombardment effects. Here we present data on the effect of grain boundary morphology on stability.

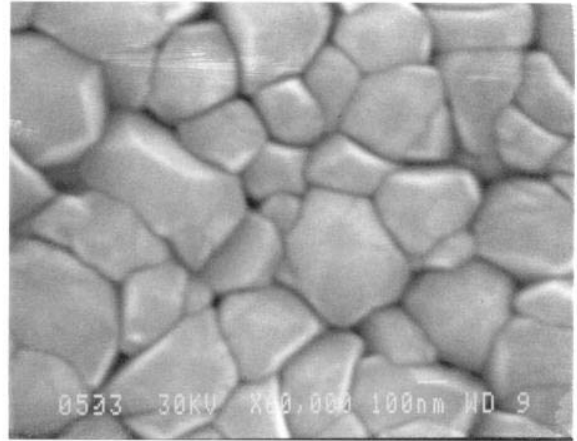


CdTe on SnO₂, 10mT, 26w, 360°C ($T_s/T_m = 0.48$), UM: 39/3



CdTe on SnO₂, 18mT, 26w, 360°C ($T_s/T_m = 0.48$), UM: 39/3

Fig. 2.3.1: Scanning electron micrographs of CdTe films deposited with 10, 18 and 50 mTorr of gas pressure.



CdTe on SnO₂, 50mT, 26w, 360°C ($T_s/T_m = 0.48$), UM: 39/3

For the current study, we prepared CdS/CdTe devices with CdTe deposited at 9, 18 and 36 mTorr, while the rest of the device fabrication, post-deposition treatment and Cu/Au back contact recipe was kept the same in all three sets of devices. The main purpose of this study was to examine the differences in stability due to grain boundary morphology. The completed devices were stressed at open-circuit condition under one-sun illumination at about 60-65°C.

Figure 2.3.2 shows the average (3-5 devices) change in device parameters with stress time. The major difference in degradation was observed in V_{oc} and FF, and therefore efficiency. The initial V_{oc} of the devices with CdTe deposited at 36 mTorr was highest (average: 824 mV, best cell: 835 mV) but the 36 mTorr cells degraded faster than cells deposited at 18 or 9 mTorr. We suggest this is probably due to more diffusion/electromigration of Cu along the less compact grain boundaries in cells deposited at 36 mTorr.

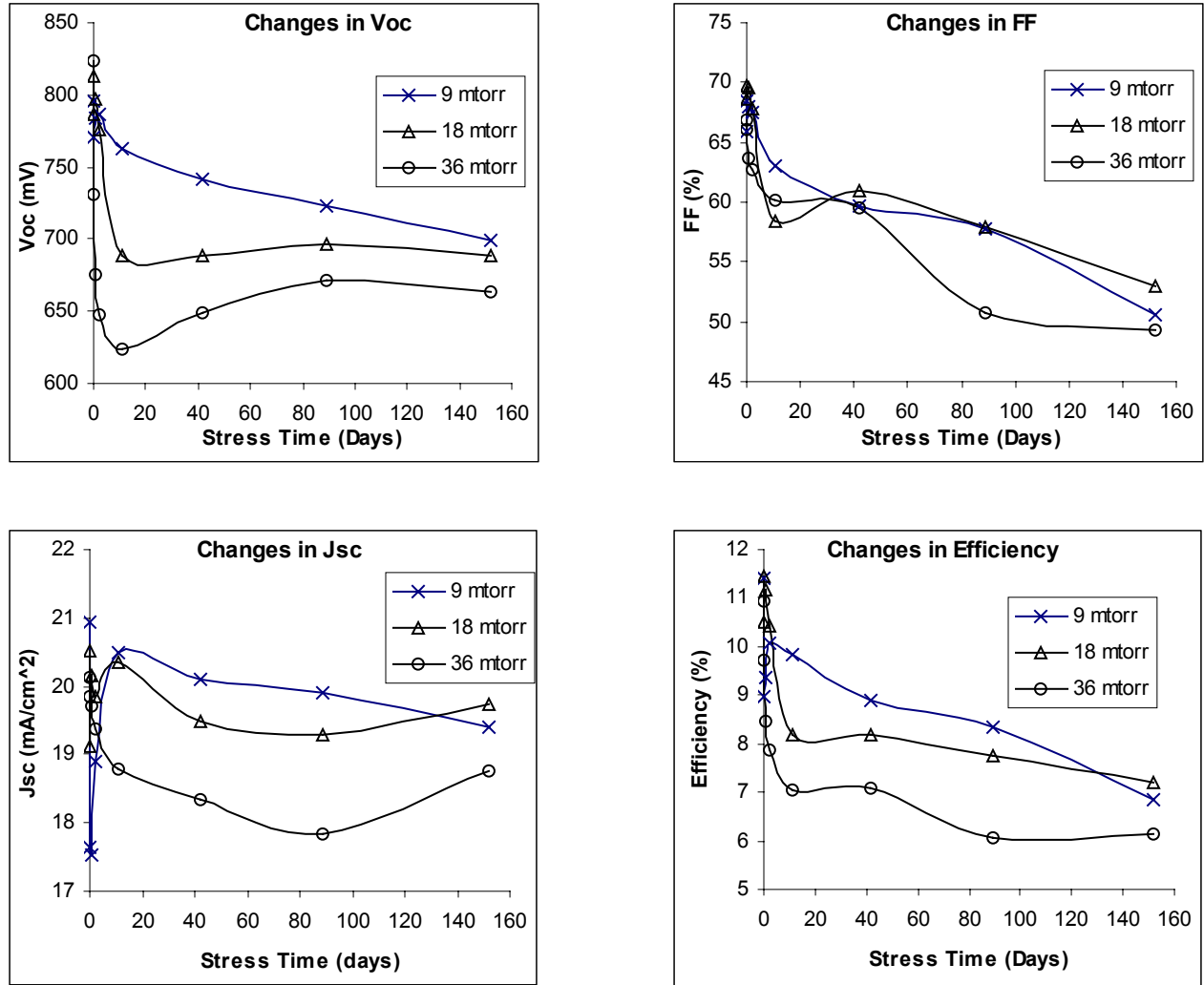


Fig. 2.3.2: Parameter degradations of CdTe solar cells sputtered at different gas pressures.

One general observation is that the parameters of different devices tend to converge after a considerable degradation time. This is consistent with the above suggestion of Cu diffusion along grain boundaries combined with the existence of a limited Cu source, which dwindles sooner or later depending on Cu effective diffusivity. Further studies are in progress to characterize the differences among these sets of devices.

2.4 Substrate-configuration cells fabricated on Mo and Kapton®

In order better to understand some of the properties of the junction region of CdS/CdTe cells, we think it would be useful to have better access to the junction region by fabricating substrate configuration CdTe cells. Again, we anticipate that the relatively low temperature processing of magnetron sputtering may provide advantages for this fabrication geometry. One anticipates fewer problems with diffusion from the substrate into the CdTe when processing is done at lower temperature and certainly for using flexible polymer substrates it would be necessary to limit the maximum temperature. The disadvantage is the inaccessibility of the back contact which is known to be critical to the performance of CdTe cells. Thus in a substrate device it is not possible to etch the CdTe just prior to the back contact application. Also, creation of a heavily-doped back-contact layer may be difficult when the CdTe/metal interface is produced at the beginning of the CdTe deposition.

Substrate configuration CdTe-based solar cells on TCO-coated glass were investigated by Birkmire *et al.*⁶, 5.5% efficiencies were achieved. Singh *et al.*⁷ and Seth *et al.*⁸ used a metal foil/CdTe/CdS/TCO structure and achieved 5.3% efficiencies. Along with manufacturing and applications advantages, the substrate/CdTe/CdS/TCO structure is also interesting because the CdTe-CdS junction is not buried under the thick CdTe layer and presents an unconventional access/morphology situation for fundamental studies. The choice of molybdenum was suggested by a close match of its thermal expansion coefficient and work function to those of CdTe. The thermal expansion coefficient of Mo is $5.0 \times 10^{-6} \text{ K}^{-1}$ and that of CdTe is $4.8 \times 10^{-6} \text{ K}^{-1}$.⁹ The work functions of Mo and CdTe are 4.3 eV¹⁰ and 5.7 eV¹¹ respectively.

We fabricated substrate-type CdTe cells on 100 μm thick molybdenum, on 125 μm stainless steel sheet, and on 10 μm thick molybdenum-coated polyimide (Kapton®). Approximately 2 μm of CdTe and 0.13 μm of CdS were sputtered in the same chamber at $\sim 250^\circ\text{C}$. The films were then processed through our vapor CdCl_2 treatment at $385 - 390^\circ\text{C}$. Front contacts consisted of 70 nm or 210 nm thick sputtered indium tin oxide (ITO). Some cells were finished with ZnO:Al instead of the ITO. Other cells included an interfacial layer of ZnTe:N between the CdTe and Mo. This ZnTe:N was about 0.15 μm thick with a resistivity of 5-10 $\Omega\text{-cm}$ and carrier concentration of $\sim 5 \times 10^{18} \text{ cm}^{-3}$. (See Figure 2.4.1.)

The substrate cells were fabricated with 100, 150, and 200 nm of CdS. The cells exhibit fairly low QE (Fig. 2.4.2) in the 400 to 500 nm region which is consistent with no CdS consumption (S interdiffusion into CdTe or TCO) during CdCl_2 treatment. This is in contrast to our usual superstrate cells which showed better QE in the blue than expected based on the as-deposited CdS thickness. This arises from interdiffusion at the CdS/CdTe interface. In addition, superstrate cells show some loss of response in the 550 to 600 nm region which indicates absorption in a CdS-rich alloyed layer CdS(Te). The QE curves of substrate cells (Fig. 2.4.2) with thicker CdS (150 nm and 200 nm) show little evidence of interdiffusion but the cell with thinner CdS (100 nm) shows a response similar to the superstrate cells. The differences in the QE data lead to a conclusion that the presence of a CdS layer more than about 100 nm thick inhibits interdiffusion during the CdCl_2 treatment. We suggest that this difference may result from the fact that the CdS is grown on fully formed CdTe grains (Fig. 2.4.1(b)) rather than being adjacent to the small-grain nucleation layer of CdTe. For the 200 nm CdS layer, the QE also shows little shift to the red near 850 nm which implies little diffusion of S into the CdTe. The QE of cells with thinner CdS layers show the usual shift implying formation of the CdTe-rich alloyed layer of CdTe(S) at the top of the CdTe during the CdCl_2 treatment.

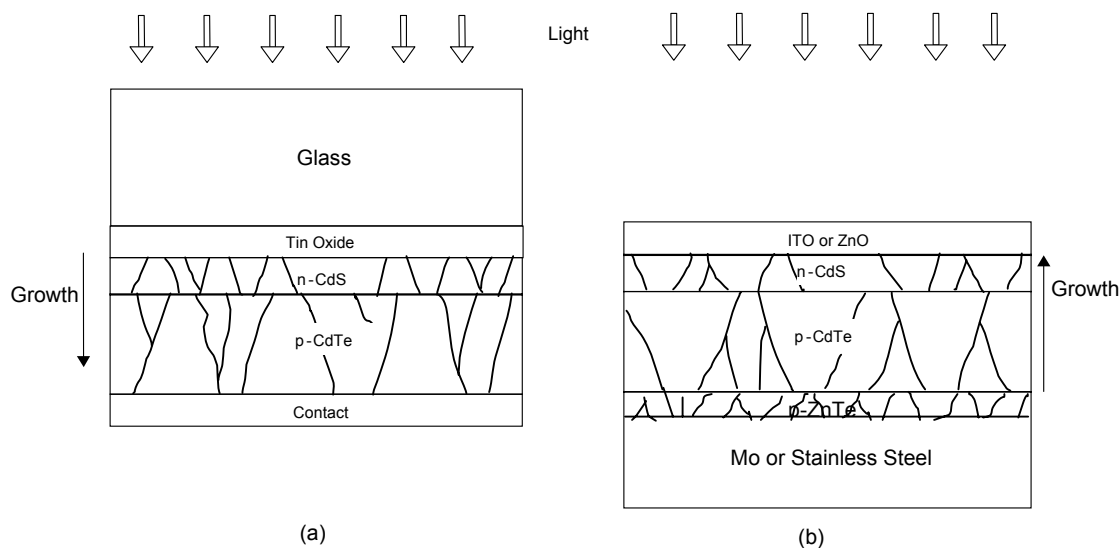


Fig. 2.4.1. Sketch of superstrate (a) and substrate (b) cells illustrating that for substrate cells the CdS grows on fully formed CdTe grains and suggesting a possible explanation for the smaller interdiffusion.

The conversion efficiency of our best CdTe-based substrate configuration solar cell is 7.8% (cell area 0.05 cm²). This is a significant increase over the earlier reported values. The I-V curve of the 7.8% efficient solar cell is shown in Fig. 2.4.3, this device has a ZnTe:N layer between Mo and CdTe. Our sputtered substrate-type solar cells with ZnO:Al top electrode (and ZnTe:N) were up to 5.8% efficient, cells on Mo-coated polymer or stainless steel were about 3% efficient. All current-voltage curves show severe roll-over in the first quadrant with effects extending into the third (power) quadrant. This is most probably due to a reverse (blocking) diode behavior at the metal-CdTe interface, although problems at the CdS-TCO interface cannot be excluded. Smoother substrates also might improve the overall performance of cells; for this work we used a fairly rough Mo foil (400 nm peak-to-valley roughness).

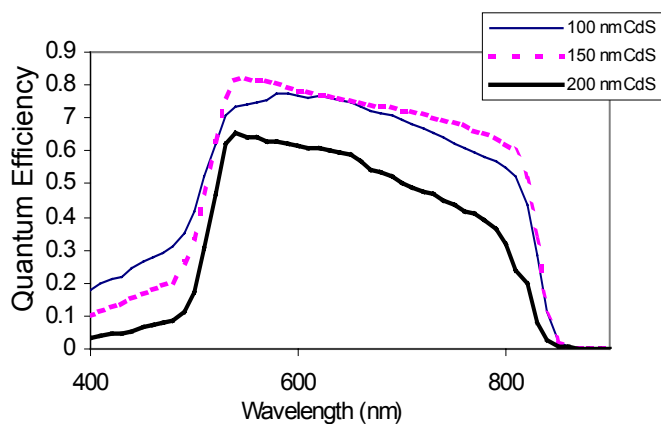


Fig. 2.4.2 Q-E response for substrate cells on Mo with different CdS layer thickness. Note apparent lack of interdiffusion for cell with 200 nm CdS.

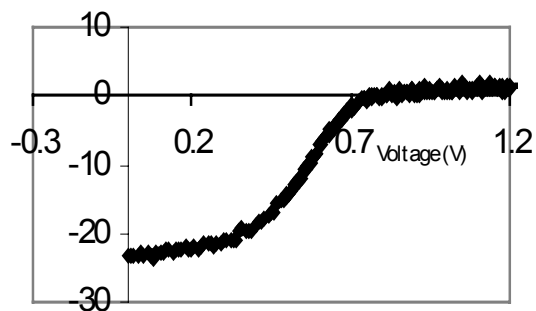


Fig. 2.4.3 I-V curve of a 7.8% efficient cell with the structure Mo/ZnTe:N/CdTe/CdS/ITO

2.5 CdS/CdTe devices with HRT layers

In our lab, we have not had the capability of depositing high resistivity interfacial layers between the TCO and CdS. However, we continue to study such layers in collaboration with First Solar. During the past year, we studied two different types of HRT layers on 3 mm Tec-15 glass (SLG/SnO₂:F/HRT) that were part of a production run of Pilkington and were made available to us through First Solar. The sheet resistance of the HRT was separately measured with one having $R_s=4500 \text{ } \Omega/\square$ (#609) and the other $R_s=1500 \text{ } \Omega/\square$ (#691). Complete devices were fabricated on both HRT/TCOs using 25 nm and 130 nm of CdS. The rest of the processing was standard. Table 2.5.1 shows the detailed I-V parameters obtained for the best devices. (For comparison, we have included the I-V parameters for the devices prepared on the “good” HRT “C24” from our final report of the previous contract² (Table 2.5.2).) In comparison to devices made on good HRT, the efficiency of devices on these new HRTs 609 & 691 was only 4-6%.

Table 2.5.1.: IV data of best devices on new HRT (as received HRT).

Sample No.	HRT No.	HRT R_s (Ω/\square)	CdS (nm)	Voc (mV)	Jsc (mA/cm ²)	FF (%)	Eff. (%)	Roc (ohm-cm ²)	Rsh (ohm-cm ²)
H1B	609	4500	25	553	17.88	47.65	4.71	7.01	134
938HB	609	4500	130	718	14.78	56.52	6	7.42	271
L1B	691	1500	25	631	18.85	48.22	5.74	8.86	157
938LB	691	1500	130	691	13.81	53.54	5.11	10.61	254

Table 2.5.2. : IV data of devices prepared on good HRT (C-24) and reported in last annual report.

Sample	CdS (nm)	Voc (mV)	Jsc (mA/cm ²)	FF (%)	Eff. (%)	Roc (ohm-cm ²)	Rsh (ohm-cm ²)
H920B	0	607	25.93	63.16	9.94	5.41	379
H921A	25	727	25.46	62.22	11.51	6.25	584
H922A	50	716	24.99	66.4	11.88	4.94	833
H923A	80	801	24.2	69.49	13.46	5.26	837
H924A	130	824	21.14	71.08	12.39	4.85	1014

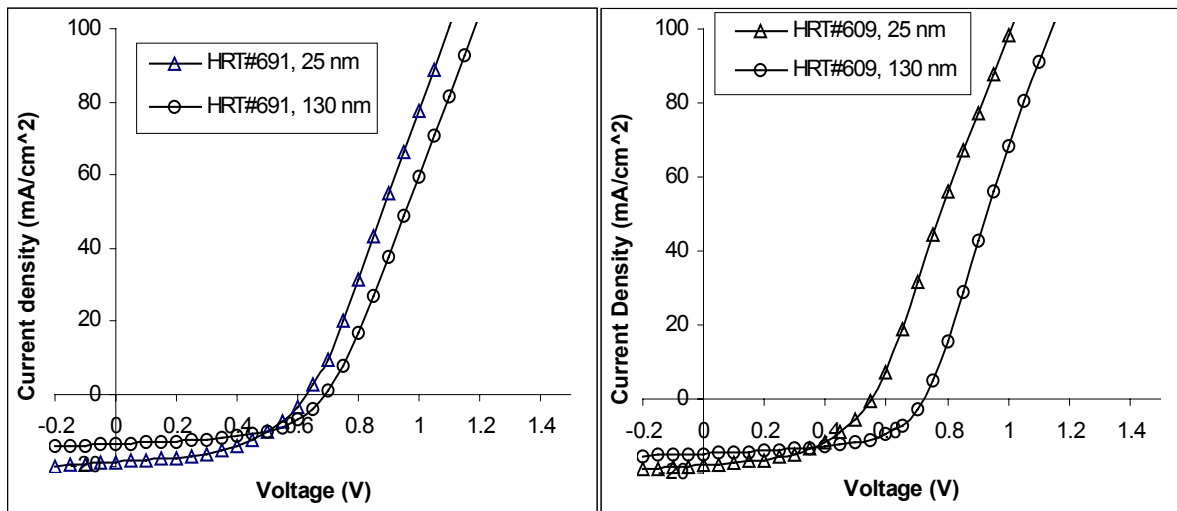


Fig. 2.5.1 I-V curves of cells with different HRT types and two different CdS thicknesses

The I-V plots of the best devices prepared on new HRTs with thin and standard CdS thickness are shown in Fig. 2.5.1. The effect of CdS thickness is clearly visible *i.e.* with the increase of CdS thickness, V_{oc} increases and J_{sc} decreases. However, the overall efficiency was very much lower than for devices on good HRT (Table 2.5.2.). The comparison of the I-V of the best cells on all three HRTs (Fig 2.5.2.) clearly shows higher V_{oc} , J_{sc} and FF for devices on good HRT (C24). The QE measurements (Fig. 2.5.3) show the increase in J_{sc} from the blue region of spectrum with the decrease in CdS thickness but also show the poor quality of the junction (lower QE overall). The figure also shows the QE of cells with the same thickness of CdS fabricated on good HRT (C-24) received from First Solar.

By contrast, devices processed by VTD at First Solar on HRT-609 substrates were very good ($\sim 12\%$ efficiency). We suspected that either the high temperature of the VTD processing was improving the HRT or the magnetron RF process was damaging the HRT layer. Therefore, we heat treated the HRT-609 and 691 in vacuum at 550°C , and then fabricated sputtered devices. This heat treatment did not improve the device performance (Table 2.5.3). As a second test, CdS (~ 70 nm) was deposited using the First Solar VTD process, and we fabricated the rest of the device using magnetron sputtered CdTe, our standard CdCl_2 treatment and back contact process. The V_{oc} on these devices was relatively low (770-790 mV) due to thin CdS but the efficiency was very good $\sim 12\%$ (Table 2.5.4). This showed that not only temperature but also CdS processing technique affected CdS/CdTe devices. This clearly indicates that the HRT deposition technique has to be compatible with the rest of the processing of the devices.

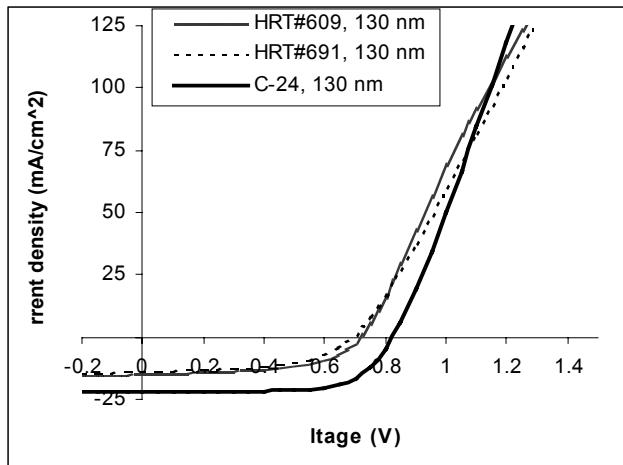


Fig. 2.5.2: Comparison of I-V curves of devices prepared on HRTs 691, 609 and C-24 with 130 nm CdS

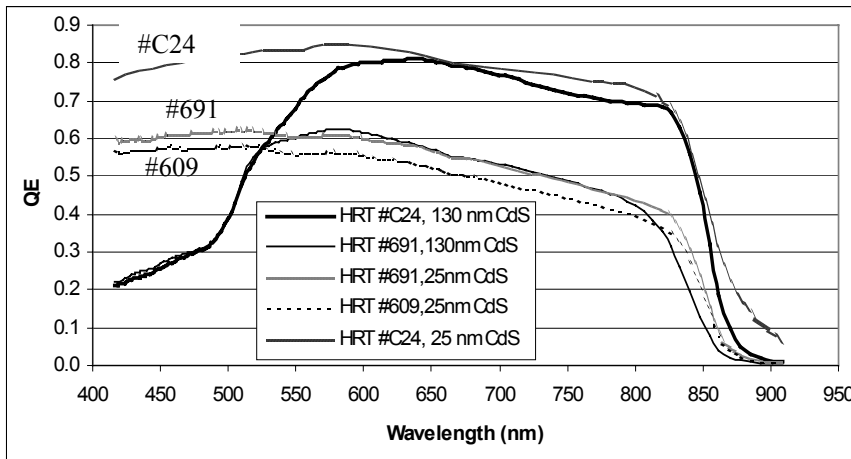


Fig: 2.5.3 Comparison of QE for devices with thin and thick CdS on HRTs C24, 691 and 609

Table 2.5.3.: I-V data of best devices on new HRT heat-treated at 550C, 200 mT for 2 min.

Sample	HRT No.	HRT R_s (Ω/\square)	CdS (nm)	Voc (mV)	Jsc (mA/cm^2)	FF (%)	Eff. (%)	Roc ($\Omega\text{-cm}^2$)	Rsh ($\Omega\text{-cm}^2$)
951A2	609	4500	50	688	14.74	55.5	5.63	10.86	291
951B2	691	1500	50	657	13.77	55.06	4.98	8.73	272

Table 2.5.4.: IV data of best device on HRT 609/ VTD CdS/ RF sputtered CdTe structure.

Sample	CdS (nm)	Voc (mV)	Jsc (mA/cm^2)	FF (%)	Eff. (%)	Roc ($\Omega\text{-cm}^2$)	Rsh ($\Omega\text{-cm}^2$)
983B1	~70 nm	789	23.07	68.11	12.4	3.59	1463

The question arises about the difference in performance of the various HRTs when used with subsequent VTD CdS and CdTe vs. rf sputtered CdS and CdTe. We think that during the deposition of VTD CdS at high temperature, the HRT layer improves, perhaps through grain growth, and inhibits the interdiffusion between the HRT and CdS which could have extended up to CdTe junction region in the RF sputtered CdS/CdTe devices. Or there could have been some interaction between HRT and CdS (similar to Zn_2SnO_4 and CdS^{12}) during VTD processing which is beneficial for devices. The results of Table 2.5.4 do show that a combination of VTD CdS and sputtered CdTe can work to achieve high efficiency devices.

Finally, we received several pieces of “good” HRT (“C-24”) from Dean Giolando which were made at First Solar. Akhlesh Gupta completed devices using, side-by-side in the sputtering chamber, 1/2 HRT & 1/2 TEC-7 and with separate runs of 25, 65 and 130 nm of CdS. The results were almost same as our earlier data which have been reported in last year’s annual report; that is, performance in the 11-12% range. Again, progress in this area is limited by variability in the quality of the HRTs available to us and the limited quantity available. We are working to resolve these issues.

2.6 Performance and stability of cells with thin CdTe

A study of cells with CdTe of different thickness was performed under the previous contract with extensive data given in that Final Report.² During the past year we have fabricated another set of cells on Tec-7 glass (which has no HRT layer) and with 0.13 μm sputtered CdS. The CdTe thicknesses were 0.45, 0.68, 0.9, 1.35, 1.8, 2.25, 2.7 μm . The specular optical transmission of the cells, completed except for the evaporated Cu/Au (3 nm/20nm) back contact, are shown in Fig. 2.6.1. Note that the transmission is affected not only by the CdTe absorption but also by the residual absorption in the glass, $\text{SnO}_2\text{:F}$, and CdS, as well as the scattering from the texture, mainly in the SnO_2 .

The quantum efficiency, with no light or voltage bias, of selected cells are shown in Fig. 2.6.2. For the thinnest cell (0.45 μm) there is more drop in the curve toward the red, but the major effect is the overall drop in collection over the entire spectrum. This implies that the junction quality is degraded by the thin CdTe and the collection loss near 800 nm, due to thin CdTe, is secondary. The rounded shoulder from 500 to 600 nm, due to Te diffusion into CdS to form the CdS-rich alloy during the vapor CdCl_2 process at 387 $^\circ\text{C}$, is little changed with the thinner CdTe layers. Furthermore the red shift of the long wavelength end of the QE, due to S diffusion into the CdTe is likewise little affected by the CdTe thickness.

The I-V device parameters are shown in Fig. 2.6.3 as a function of CdTe thickness for all seven CdTe thicknesses. In order to determine whether a decreased CdTe thickness impairs the stability, we show the device parameters taken at three different times. The first was taken immediately after the 45 minute 150 $^\circ\text{C}$ diffusion step following the Cu/Au evaporation. Each datum point is the average of the three best cells. Much of the variation in cell parameters with

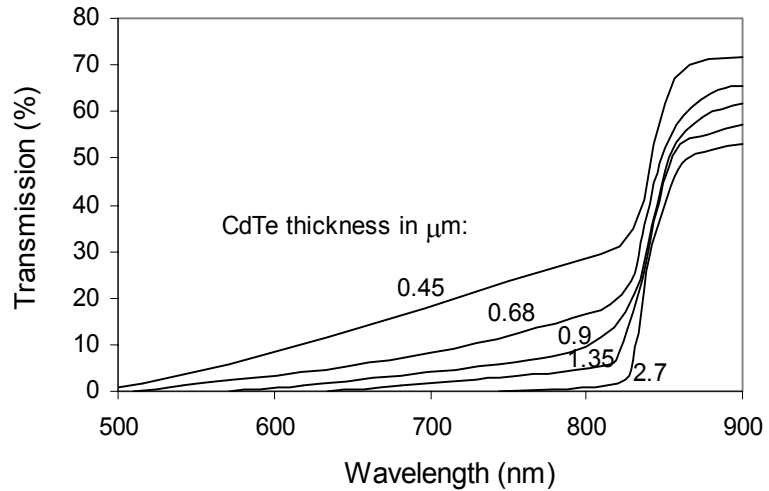


Fig. 2.6.1 Transmission through cell structures with different CdTe thicknesses.

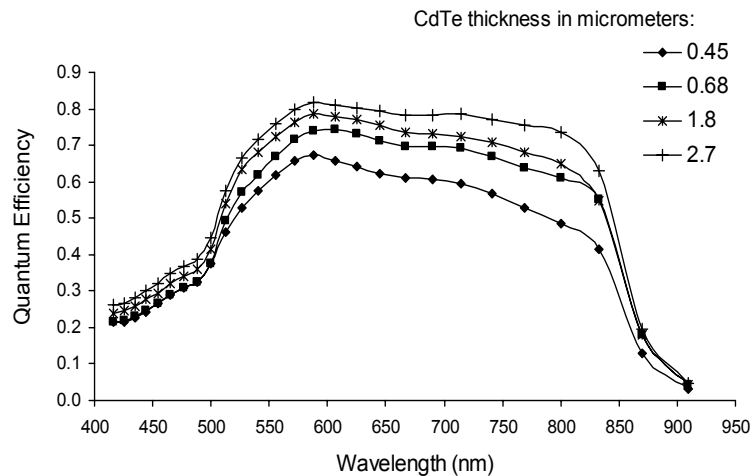


Fig. 2.6.2. Spectral quantum efficiencies of solar cells with different CdTe thicknesses.

thickness is related to process variability, but there is a gradual decrease in device parameters as the CdTe thickness decreases through 0.68 μm of CdTe. Large drops in performance parameters occur at 0.45 μm . Cells with all thicknesses of CdTe exhibit drops in performance after 24 hours and after 7 days of light soak at one-sun, $\sim 55^\circ\text{C}$. (After an additional 30 days of storage at room temperature and ambient light, the cell performance was essentially unchanged from the 7 day stress data.) These data show no evidence of greater degradation for thinner CdTe layers. In particular, for these evaporated Cu/Au contacts, degradation does not get worse in cells with the contact layer closer to the active junction, *i.e.*, in the cells with thinner CdTe.

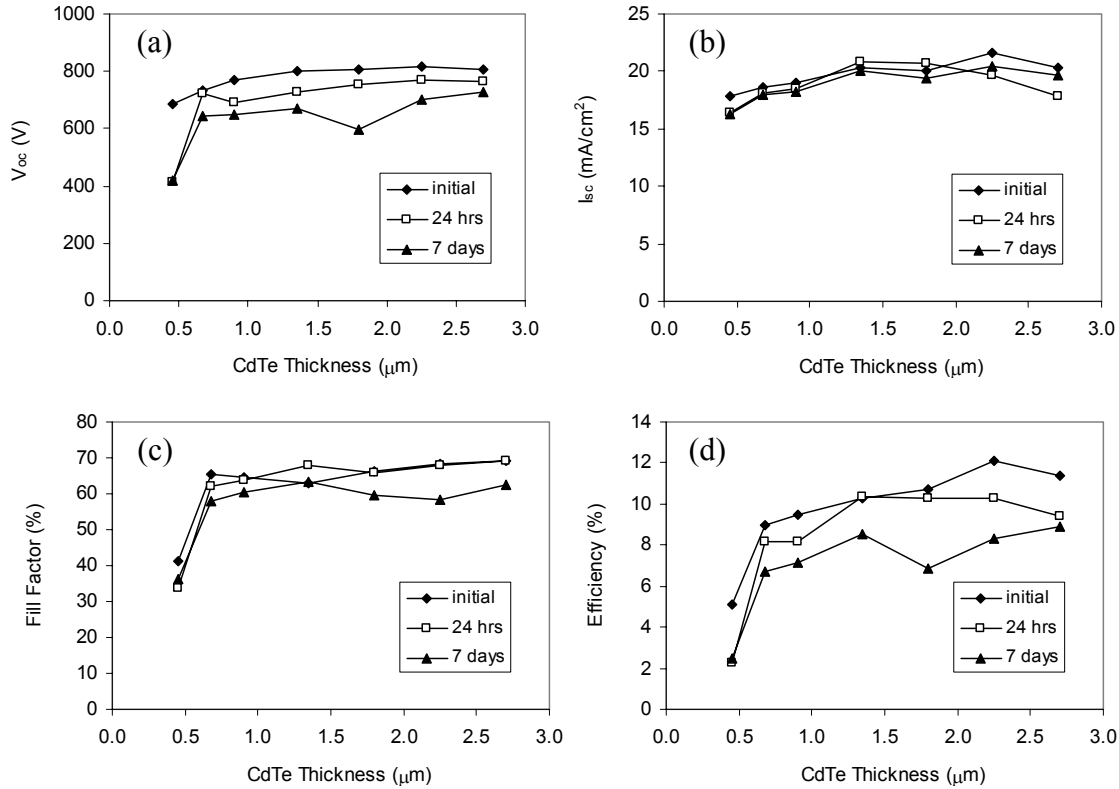


Fig. 2.6.3 Cell parameters (V_{OC} , I_{SC} , FF, Eff.) vs. CdTe thickness for average of three cells showing values initially, and after 1 and 7 days of light soak at 55°C , V_{OC} .

These results with sputtered CdS and CdTe show device efficiency dropping from about 12% for 2.5 μm of CdTe to about 9% for 0.68 μm of CdTe. This is at least as good as the results reported by Amin, et al,¹³ for close spaced sublimation of CdTe who reported efficiency dropping from 14.3% at 5 μm of CdTe to 10.2% at 1 μm . (Actually, as discussed in Section 2.2 above, we have achieved 14.0% efficiencies with 2.3 μm of CdTe using more transparent glass and ZnO:Al as the TCO. Since the ZnO is much smoother than the Tec-7 glass used for this study, we hope to show even better results with this combination of materials for thin CdTe structures.)

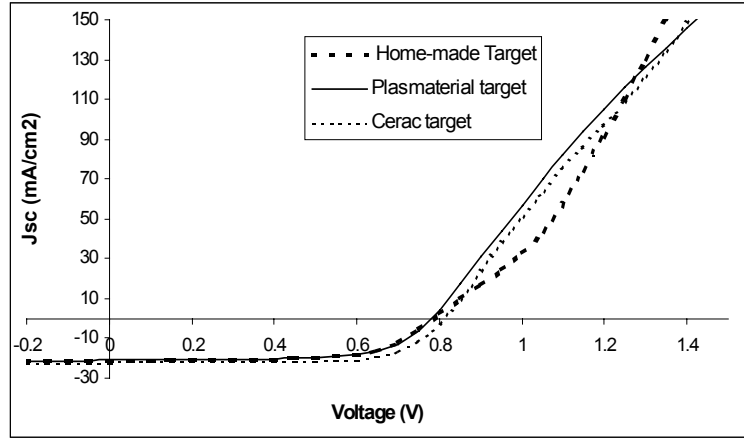
2.7 Doping studies of CdTe films by reactive sputtering from CdTe/Cd₃P₂

Our capability of fabricating two-inch sputter targets by cold pressing from powders has facilitated our studies of alloy films. To test the quality of these cold-pressed targets, a CdTe target was pressed from 99.999% powder from Alfa Aesar, and used in device fabrication with our standard CdS/CdTe thickness, CdCl₂ treatment and Cu/Au back contact. The CdS layer was deposited from a commercial Cerac target. Table 2.7.1 shows the comparative I-V device data for home-made and commercial (Cerac Inc., and Plasmaterials Inc.) CdTe targets, and Fig 2.7.1 shows I-V plots for the same devices.

Table 2.7.1: Comparative I-V data for devices made from commercial and home-made CdTe target

CdTe Target	Sample #	Voc(mV)	Jsc(mA/cm ²)	FF	Eff.(%)	Roc(Ω-cm ²)	Rsh(Ω-cm ²)
home-made	CH1-A, #3	786	21.26	65.85	11	9.01	640
Plasmaterials	945B1, #8	779	21.08	67.17	11.04	6.33	712
Cerac	005A, #2	812	21.97	70.35	12.55	5.62	1267

Fig. 2.7.1: Comparative I-V plots for devices made from home-made and commercial CdTe targets.



Although the best devices were obtained from the commercial Cerac CdTe target, we were able to make an 11% device from a cold-pressed, home-made target without any optimization of CdTe layer thickness or back-contact processing. The devices made with the home-made target had almost the same performance as those from the other commercial (Plasmaterials) target. The devices from these two targets showed lower V_{oc} , which could be increased to more than 800 mV by diffusing the back contact at higher temperature but then the FF suffered. We believe that a better FF could also be obtained by optimizing the back-contact processing using a thicker Cu layer and better optimized diffusion temperature and duration. Since the Cerac target produced the best devices, it has since been used for further research and routine device fabrication. But we have used our target pressing facility for the fabrication of doped CdTe targets. (See below.)

Wei and Zhang¹⁴ have calculated p-type dopant energies in CdTe and have suggested that P should be one of the most attractive elements for extrinsic doping in CdTe. We fabricated a mixed target of the binaries CdTe and Cd₃P₂ in order to explore the possibility of doping CdTe during magnetron sputtering. The initial target was fabricated with an atomic ratio of P/Te of 3.6%. It is thought that the use of the Cd₃P₂ powder would maintain a sputtering flux that is slightly rich in Cd and thus might facilitate P locating on Te vacancy sites. We have not yet

done systematic studies of the material properties but did attempt to fabricate some devices using the CdTe:P for either part of, or the entire absorber layer.

The CdS layer of standard thickness was deposited from a commercial Cerac target, and if a partial CdTe layer was used, it was also sputtered from a commercial Cerac target. The devices were given UT's standard vapor CdCl₂ treatment after CdTe deposition(s). *Since the aim of this study was to use P for doping of CdTe, the devices were finished with a Au-only contact.* The detailed device results are given in Table 2.7.2, and I-V plots are shown in Fig 2.7.2. For comparison purposes, we have included the device results from home-made and commercial targets with Au-only back contacts. The cells with a complete CdTe:P(1.79%) layer showed good current densities (~20 mA/cm²) but V_{oc} and FF were only about 500 mV & 40% respectively for 2.3 µm thick CdTe:P (device 934A #17). These values were lower than those of cells made from similarly pressed pure CdTe (device CH2A2 #7). This might suggest problems with P doping near the junction. The increased V_{oc} and FF obtained by using a sandwich layer with pure CdTe at the junction (device 933A #16) supports this interpretation.

Table 2.7.2: I-V parameters of devices with Au-only contacts prepared from CdTe:P, Cerac and home-made targets

CdTe:P Target #1							
Atomic Wt. % of Cd3P2 in target: 1.79%; P/Te atomic % : 3.64%							
Device #	Structure	Voc	Jsc	FF	Eff	Roc	Rsh
934A, #17	CdS(0.13 µm)/CdTe:P(2.3 µm)/Au	492	19.83	40.51	3.95	19.48	75
933A, #16	CdS(0.13 µm)/CdTe(1.8 µm)	642	21.62	56.87	7.89	11.88	232
	+CdTe:P (0.4 µm)/Au						
CdTe:P Target #2							
At. Wt. % of Cd3P2 in target: 0.41%; P/Te atomic % : 0.82%							
Device #	Structure	Voc	Jsc	FF	Eff	Roc	Rsh
CTP4B1, #12	CdS(0.13 µm)/CdTe:P(2.5 µm)/Au	719	19.86	56.44	8.06	14.38	471
SSC963B1 #2	CdS(0.13 µm)/CdTe(1.8 µm)	759	19.07	59.04	8.54	12.72	725
	+CdTe:P (0.7 µm)/Au						
Home-made CdTe Target							
Device #	Structure	Voc	Jsc	FF	Eff	Roc	Rsh
CH2A2 # 7	CdS(0.13 µm)/CdTe(2.5 µm)/Au	675	19.56	43.1	5.69	22.64	144
Commercial CERAC CdTe Target							
Device #	Structure	Voc	Jsc	FF	Eff	Roc	Rsh
SSC005E, #6	CdS(0.13 µm)/CdTe(2.3 µm)/Au	739	20.65	50.27	7.67	19.31	468

In fact, the FF of this device was much better than obtained using pure CdTe (and Au-only contacts) either from a home-made (CH2A2#7) or a commercial Cerac target (SSC005E# 6).

Therefore, a second target with less P was pressed (0.41 at. % P/Te), and devices were fabricated with similar thickness and processing. The two devices, one with a 2.5 µm CdTe:P absorber and one with a 1.5 µm CdTe layer at the junction followed by 0.7 µm CdTe:P, showed much better performance than those from the heavier-doped home-made target, and also better than from the commercial Cerac target with Au-only contacts. Both, FF & Voc were improved.

A direct comparison between two Au-only contacted devices, 1) one prepared with a uniform, undoped 2.5 μm CdTe absorber layer from the UT pressed target (CH2A2 #7), and 2) the other prepared from the more lightly doped home-made target (CTP4B1 #12) shows clearly the effect of CdTe doping in improving all device parameters including R_{oc} & R_{sh} . This shows that doping of phosphorous into CdTe films by sputtering improves not only the junction

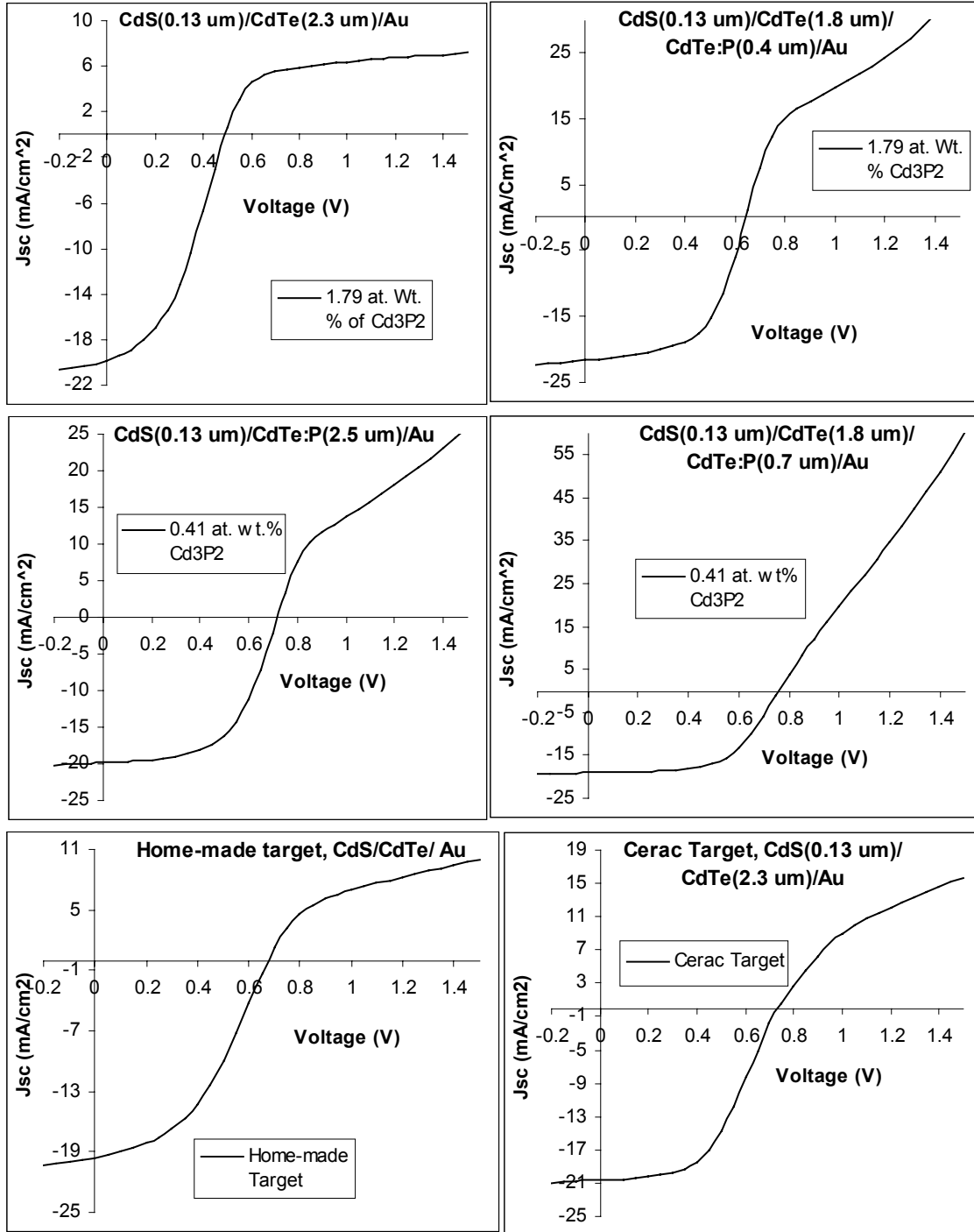


Fig. 2.7.2: I-V plots of devices from CdTe:P, Cerac, and home-made targets; Au-only contacts

properties but also the back contact. Thus we have established the capability of fabricating devices from the extrinsically doped CdTe, but we have not yet quantified the optimum doping level or other materials properties. This effort continues.

We have studied the stability of devices with CdTe:P absorber layer and Au-only contact, under 1 sun continuous illumination and open-circuit condition at $\sim 55^{\circ}\text{C}$ temperature. The samples were taken out from the stress station and cooled down for ~ 20 min to room temperature before taking the I-V measurements. The detailed I-V parameters of devices (including Cu/Au contacted) are shown in Table 2.7.3.

Table 2.7.3: I-V stability data of P-doped devices with Au-only contacts

Device: CTP4B1, **Structure:** CdS (0.13 μm)/CdTe:P (2.5 μm)/Au

Average data of 10 cells

Stress time	Voc	Jsc	FF	Eff	Roc	Rsh
0 days	691	19.31	54.64	7.29	16.94	388
28 hrs	660	19.36	53.14	6.79	15.99	262
10 days	666	18.71	54.45	6.78	14.58	237
77 days	576	17.24	48.6	4.82	16.43	146

Device: SSC 963B1, **Structure:** CdS (0.13 μm)/CdTe (1.8 μm)/ CdTe:P (0.7 μm)/Au

Average data of 8 cells

Stress time	Voc	Jsc	FF	Eff	Roc	Rsh
0 days	725	19.00	55.09	7.6	17.67	628
28 hrs	698	20.92	56.05	8.19	11.96	385
10 days	713	21.00	59.33	8.89	13.33	594
77 days	626	20.13	43.54	5.51	16.87	133

Standard Structure from CERAC target but with Au-only contact

Device: SSC956B2, **Structure :** CdS (0.13 μm)/ CdTe (2.3 μm)/Au

Average data of 2-4 cells

Stress time	Voc	Jsc	FF	Eff	Roc	Rsh
0 days	707	18.76	53.79	7.14	12.42	270
28 hrs	593	18.1	56.16	6.02	8.09	437
10 days	583	19.63	56.69	6.5	6.77	367
77 days	523	18.31	54.38	5.19	6.9	198

Standard Structure from CERAC target (with Cu/Au contacts)

Device: SSC970A, **Structure :** CdS (0.13 μm)/ CdTe (2.3 μm)/Cu-Au

Stress time	Voc	Jsc	FF	Eff	Roc	Rsh
0	810	21.37	69.44	12.03	5.51	1433
105d on table	808	21.18	69.32	11.86	5.08	1230
1 day	773	18.56	68.34	9.81	4.78	1018
12 days	692	20.18	62.19	8.67	7.69	594
122 days	649	19.33	45.22	5.67	16.99	204

The uniformly doped CdTe:P absorber device (CTP4B1) showed the poorest stability due to degradation in both J_{sc} & FF, while the bilayer absorber CdTe/CdTe:P (SSC961) and the

single layer CdTe (SSC956B2 prepared from the commercial Cerac target) devices showed almost the same stability. However, the mechanism of degradation could be different because the bilayer absorber device showed decreases in both V_{oc} & FF, whereas the pure CdTe absorber device with Au-only contacts showed major degradation in V_{oc} while the FF was stable. Although the initial efficiency of Cu/Au contacted, pure CdTe absorber devices (SSC970A, prepared from a commercial Cerac target) was very high in comparison with CdTe/CdTe:P bilayer devices with Au-only contacts, the percentage decrease in efficiency from the initial value in 77 days of light soak stress is much more than that of CdTe:P device (CTP4B1). This is because the Cu/Au contacted CdTe device showed degradation in all device parameters similar to Au-contacted CdTe:P devices. To a large extent, therefore, degradation seems much higher in devices with Cu doping rather than P doping. These studies are continuing.

2.8 Chloride treatments and back-contact application on electrodeposited CdTe

As part of the National CdTe Team activities, we participated in studies of chloride processing, specifically using our vapor CdCl₂ process on plates from BP Solar with their CdS and CdTe process. We and BP were particularly interested in whether the vapor process as optimized for our magnetron sputtered material would require adjustment for materials deposited by very different processes but almost similar grain size. We have earlier observed that high-temperature-deposited (VTD) films from First Solar 3 - 4 μm thick can be treated successfully with our vapor treatment process with slight adjustment in the treatment (using a treatment temperature of 395 °C instead of 387 °C that we use for our 2 - 2.5 μm thick CdTe).

Effect of CdCl₂ treatment temperature: BP Solar supplied a plate (ID3144) of their standard as-deposited CdS/CdTe structure. The isothermal CdCl₂ treatment (film and source at the same temperature) on pieces of this plate was carried out at 375, 387 and 400°C in dry air for 30 min. Several 0.15 cm² devices were made on each sample by evaporation of a 3 nm Cu/20 nm Au back contact, with no surface treatment before or after the CdCl₂ processing, similar to sputtered cells. The devices were characterized using I-V measurements (Table 2.8.1).

Table 2.8.1 : Effect of CdCl₂ treatment temperature (average IV data of six devices)

Sample No.	CdCl ₂ treatment T	V _{oc} (mV)	J _{sc} (mA/cm ²)	FF (%)	Eff. (%)	R _{oc} ($\Omega\text{-cm}^2$)	R _{sh} ($\Omega\text{-cm}^2$)
BPS3A	375C	688	23.74	66.45	10.85	4.45	698
BPS1A	387C	726	24.36	69.21	12.24	5.13	1548
BPS2A	400C	716	24.41	66.86	11.68	6.3	1368

The best efficiency devices were obtained at a CdCl₂ treatment temperature of 387°C which is also best for sputtered CdTe devices. Apparently the optimum CdCl₂ treatment temperature is not affected by the deposition technique for material of essentially the same grain size. The efficiency of optimally treated devices was about 12% with higher current density, and lower V_{oc} than our sputtered devices. Since the CdTe layer thickness of the BP material is typically about 1.8 μm compared with our sputtered devices of 2.3 μm , we further studied the effect of back contact diffusion temperature. The detailed I-V parameters, given in Table 2.8.2, clearly show that by increasing the diffusion temperature, the V_{oc} can be increased to 771 mV at 170 °C diffusion, but the FF decreases significantly from its maximum of 68.4% at 150° C.

Table 2.8.2: Effect of back contact diffusion (387°C vapor CdCl₂ treated sample)

Sample No.	Diff. temp & duration	V _{oc} (mV)	J _{sc} (mA/cm ²)	FF (%)	Eff. (%)	R _{oc} ($\Omega\text{-cm}^2$)	R _{sh} ($\Omega\text{-cm}^2$)
BPS1CA	137C/ 25min	688	24.68	65.44	11.13	4.58	662
	150C/ 25min	740	23.94	68.54	12.13	5.8	1117
	170C/25 min	771	23.74	64.25	11.75	5.75	565
	190C/25 min	760	22.89	58.75	10.22	9.64	294

Therefore, there is a trade off between V_{oc} and FF, with the best efficiency obtained for a diffusion temperature of 150C, again the same as for sputtered cells. Fig. 2.8.1a shows the changes in the I-V curve with increasing diffusion temperature. All light I-V showed some roll-

over well above V_{oc} in the forward direction irrespective of diffusion temperature. The dark IV is almost flat for a diffusion temperature of 150° C, which improved at 170° C, although the light I-V is slightly poorer.

Figure 2.8.1b shows a comparison of the QE between the BP Solar and a UT standard device. The QE of BP Solar cells shows much better transparency and current collection in the blue region indicating a thinner CdS final thickness. The lower V_{oc} in these devices is also consistent, in our experience, with thinner CdS.

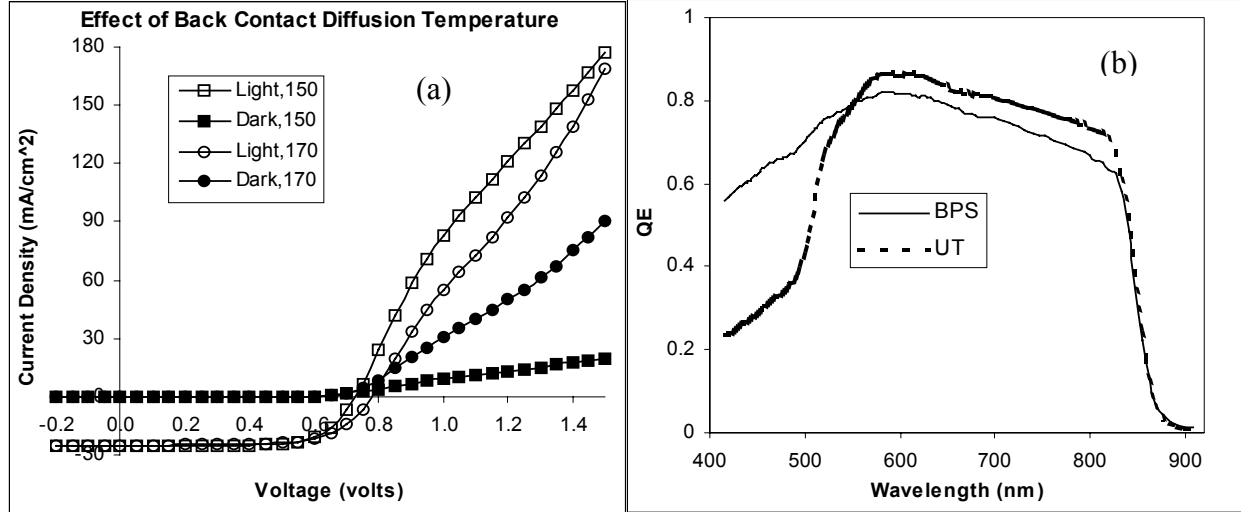


Fig. 2.8.1 : (a) Light and dark I-Vs of BP Solar cells for two different contact diffusion temperatures; (b) comparison of QE between BP Solar and UT devices

We have done some stability studies of BP Solar-supplied CdS/CdTe structures completed with UT's CdCl₂ treatment and UT's Cu/Au back contact. We have stressed five BP Solar samples along with UT's standard sputtered device. The details of the samples are:

SSC970A: UT's standard CdS/CdTe structure, CdCl₂ treated at 387° C for 30 min. The back contact is 3nm Cu/200nm Au. The sample remained on the table for 105 days before initiating the stress.

BPS1A: CdCl₂ treatment at 387° C for 30 min. The back contact is 3nm Cu/20nm Au. The back contact was diffused at different temperature successively. The sample remained on the table for 110 days before initiating the stress.

BPS1F: CdCl₂ treatment at 387° C for 30 min. The back contact is 3nm Cu/20nm Au. The back contacts were prepared just before initiating the stress.

BPS1DA: CdCl₂ treatment at 387° C for 30 min. The back contact is 3nm Cu/20nm Au. The sample remained on the table for 110 days before initiating the stress.

BPS2A: CdCl₂ treatment at 400° C for 30 min. The back contact is 3nm Cu/20nm Au. The sample remained on the table for 115 days before initiating the stress.

BPS3A: CdCl₂ treatment at 375° C for 30 min. The back contact is 3nm Cu/20nm Au. The sample remained on the table for 115 days before initiating the stress.

All the samples were stressed together at ~ 55° C under ~1 sun illumination at open circuit condition. The samples were taken out at intermediate times, cooled down to room

temperature for 10-20 min, measured and put back for continued stressing. After 122 days of stressing, the samples were kept in a plastic box on the table (room light). These were measured again after 42 days to check the recovery. The detailed stability IV performance data is given in Table 2.8.3. The purpose of this stressing was to make:

- 1) a stability comparison between UT & BP material (SSC970A & BPS1DA),
- 2) a stability comparison of successively diffused contacts (BPS1A & BPS1DA),
- 3) a stability comparison between fresh contacts and old contacts (BPS1F & BPS1DA), and
- 4) observations of the effect of CdCl₂ treatment temperature on stability (BPS1DA, BPS2A & BPS3A).

Table 2.8.3: Comparisons of stress-performance of sputtered and electrodeposited cells

UT: 970A (std material & back contact): (CdCl₂ @387C, 30 min. no etch or rinse, std 3 nm Cu/20 nm Au diffused at 150 °C for 45 min.)

Stress (days)	Voc (mV)	Jsc (mA/cm ²)	FF (%)	Eff. (%)	Roc (Ω-cm ²)	Rsh (Ω-cm ²)
0	810	21.37	69.44	12.03	5.51	1433
105d on table	808	21.18	69.32	11.86	5.08	1230
1 day	773	18.56	68.34	9.81	4.78	1018
12 days	692	20.18	62.19	8.67	7.69	594
122 days	649	19.33	45.22	5.67	16.99	204
+42d on table	666	19.49	47.28	6.14	20.77	256

BPS1F (CdCl₂ @387 °C, 30 min. no etch, std Cu/Au diffused at 150C for 45 min.)

Stress (days)	Voc	Jsc	FF	Eff	Roc	Rsh
0	767	24.62	69.64	13.15	4.06	1351
1 day	676	24.53	68.17	11.31	3.11	454
12 days	703	24.22	65.85	11.22	3.53	556
122 days	701	23.51	56.43	9.31	7.53	341
+42d on table	689	23.73	56.17	9.17	9.1	361

BPS3A (CdCl₂ @ 375 °C, 30 min. no etch. std Cu/Au diffused at 150C for 60 min.)

Stress (days)	Voc	Jsc	FF	Eff	Roc	Rsh
0	688	23.74	66.45	10.85	4.45	698
115d on table	674	24.94	65.38	10.99	3.95	521
1 day	655	23.15	57.06	8.65	3.25	159
12 days	664	23.85	67.55	10.69	2.78	384
122 days	673	23.6	58.51	9.3	5.09	240
+42d on table	700	24.39	59.81	10.22	6.57	470

BPS1DA (CdCl_2 @387 °C, 30 min. no etch, std Cu/Au diffused at 200C, 25 min)

Stress day	Voc	Jsc	FF	Eff	Roc	Rsh
0	760	23.6	61.49	11.04	6.44	478
110d on table	746	25.13	64.91	12.17	5.04	879
1 day	729	25.09	67.83	12.41	3.98	916
12 days	708	24.6	61.92	10.78	5.69	488
122 days	654	23.98	58.71	9.21	9.9	426
+42d on table	671	23.46	56.93	8.96	9.1	310

BPS2A (CdCl_2 at 400 °C, 30 min. no etch. std Cu/Au diffused at 150C for 60 min)

Stress day	Voc	Jsc	FF	Eff	Roc	Rsh
0	716	24.41	66.86	11.68	6.3	1368
115d on table	725	25.91	67.4	12.66	4.02	1347
1 day	728	25.46	63.97	11.85	4.29	464
12 days	616	24.56	50.58	7.65	7.62	122
122 days	557	23.26	48.95	6.35	7.69	104
+42d on table	551	22.72	51.67	6.46	8.33	133

The main conclusions of this study are:

1. UT devices degrade faster due to large degradation in FF, and some degradation in V_{oc} & J_{sc} .
2. For BPS cells, successively diffused contacts are better than one-temperature diffused & fresh contact but poorer than the old contact. This is mainly due to a larger change in FF.
3. The CdCl_2 treatment temperature has great effect on stability. The highest temperature (400°C) treated devices (BPS2A) are least stable due to large degradation in V_{oc} and FF. Surprisingly, the stability of the lower-temperature (375 and 387 °C) treated devices is almost the same due to quite stable V_{oc} in one case (only ~2% decrease for 375°C devices) and FF in other (less than 5% decrease for 387°C devices). These devices are the most stable too, still holding ~83% of initial efficiency after 122 days of stress.
4. Similar to degradation, the recovery (42 days in room light) is not consistent in all samples. Some samples (BPS1DA & BPS1A) show further degradation even though their V_{oc} is recovered, due to a decrease in the FF. The devices with 375°C CdCl_2 treatment show highest recovery (~9%) due to recovered V_{oc} & J_{sc} (larger than initial value!!).

References

- ¹ M. Shao, A. Fischer, D. Grecu, U. Jayamaha, E. Bykov, G. Contreras-Puente, R.G. Bohn, and A.D. Compaan, "Radio-frequency-magnetron-sputtered CdS/CdTe solar cells on soda-lime glass," *Appl. Phys. Lett.* **69**, 3045-3047 (1996); A.D. Compaan, M. Shao, C.N. Tabor, Z. Feng, A. Fisher, I. Matulionis and R.G. Bohn, "RF sputtered CdS/CdTe solar cells: effect of magnetic field, RF power, target morphology and substrate temperature", First WCPEC, Hawaii, Dec. 5-9, 1994, pp.111-114.
- ² A.D. Compaan, X. Deng, and R.G. Bohn, "High efficiency thin film CdTe and a-Si based solar cells", Final technical report, 2001, submitted to NREL.
- ³ A. Romeo, A.N. Tiwari, H. Zogg, M. Wagner and J.R. Gunter, "Influence of transparent conducting oxides on the properties of CdTe/CdS solar cells", 2nd WCPEC, Vienna, July 6-10, 1998, pp.1105-1108
- ⁴ G. Gordillo, M. Grizzle, L.C. Moreno and F. Landazabal, "Influence of optical window on the performance of TCO/CdS/CdTe solar cells", *phys. stat. sol (b)*, **220** (2000) 215
- ⁵ M. Shao, U. Jamayaha, E. Bykov, C.N. Tabor, and A.D. Compaan, "Performance vs. Microstructure in RF Sputtered CdS/CdTe Solar Cells," 25th IEEE Photovoltaic Specialists Conference-1996, pp. 869-872.
- ⁶ R.W. Birkmire, L.C. DiNetta, S.C. Jackson, P.G. Lasswell, B.E. McCandless, J.D. Meakin, and J.E. Phillips, "CdTe/CdS devices for tandem solar cells based on CuInSe₂," 18th IEEE PVSC Conf. Proc., 1985, p 1413.
- ⁷ V.P. Singh, J.C. McClure, G.B. Lush, W. Wang, X. Wang, G.W. Thompson, E. Clark, "Thin film CdTe-CdS heterojunction solar cells on lightweight metal substrates," *Solar Energy Materials & Solar Cells* **59** (1999) 145-161.
- ⁸ A. Seth, G.B. Lush, J.C. McClure, V.P. Singh, D. Flood, "Growth and characterization of CdTe by close spaced sublimation on metal substrates," *Solar Energy Materials & Solar Cells*, **59** (1999) 35-49.
- ⁹ J.C. McClure, V.P. Singh, G. Lush, "Foil mounted thin-film solar cells for space and terrestrial applications," *Sol. En. Mater. Sol. Cells*, **55**, 141-8 (1998).
- ¹⁰ M.A. Lieberman and A.J. Lichtenberg, "Principles of Plasma Discharges and Materials Processing", Wiley 1994, p. 283.
- ¹¹ R.H. Bube, "Photovoltaic Materials", Imperial College Press, 1999.
- ¹² X. Wu, R. Ribelin, R.G. Dhere, D.S. Albin, T.A. Gessert, S. Asher, D.H. Levi, A. Mason, H.R. Moutinho and P. Sheldon, "High efficiency Cd₂SnO₄/Zn₂SnO₄/Zn_xCd_{1-x}S/CdS/CdTe polycrystalline thin film solar cells", 28th IEEE photovoltaics specialists conference, Anchorage, Alaska, Sept. 17-22, 2000.
- ¹³ N. Amin, T. Okamoto, A. Yamada, and M. Konagi, "New approaches on thinner CdTe thin-film solar cells," 2nd WCPEC, Vienna, 1998, pp. 1081-1084.
- ¹⁴ Presented in National CdTe Team meeting, Oct. 31-Nov. 1, 2002, NREL, Golden, Colorado.

3. Cell modeling

3.1 Lateral nonuniformities: survey and analytical results

In this chapter we show how the intrinsic polycrystalline character of the films together with electronic transport that is exponentially sensitive to fluctuations in local materials parameters, leads to strong fluctuations in electronic properties. Controlling or blocking the effects of these fluctuations can be the key not only to the fabrication of a high performance device, but is often critically important to reducing the performance deterioration over time.

Our emphasis is on the lateral device nonuniformities. These originate from relatively weak local fluctuations in the materials parameters such as grain size, chemical composition and film thickness, but they translate into strong fluctuations in the electronic properties. The amplification comes from the fact that electronic transport through the potential barriers is exponentially sensitive to the local parameter fluctuations in both the temperature-activated and tunneling modes. Indeed, for a barrier of height V_B and width a , the corresponding barrier transmission probabilities, $\exp(-V_B/kT)$ and $\exp(-2a\sqrt{2mV_B}/\hbar)$ typically have exponents much greater than one. Hence, their relatively small variations cause significant effects. Here k is Boltzmann's constant, T is the temperature, and \hbar is Planck's constant. The barriers in PV cells are associated with the device junctions (p-n, semiconductor/TCO, and semiconductor/metal) and grain boundaries. The current density vs. bias voltage V is specified in the ideal diode model as ¹

$$j = j_0 \left\{ \exp \left[\frac{e(V - V_{oc})}{kT} \right] - 1 \right\}, \quad (1)$$

where V_{oc} is related to the junction barrier height, whose fluctuations become exponentially significant if they exceed kT .

Experimentally, lateral nonuniformities are often masked by low resistance contacts that level out the electric potential variations across the cell through lateral current flow in the contacts. As explained in detail below, lateral currents cause resistive losses and nonuniform device degradation. Therefore, although low resistance contacts make the nonuniformities less visible, they contribute detrimental side effects. To circumvent this masking effect, the nonuniformities are best studied either in unfinished devices (without metal contact), in devices with intentionally high resistance contacts, or via processes that are relatively independent of metal contacts, such as charge carrier recombination or collection.

Lateral nonuniformities can also show up in parameter variations among nominally identical devices. For example, it is typical to observe noticeable ($\sim 10\%$) experimental differences between cells ~ 1 cm apart on the same substrate. This observation is not often addressed in academic reports and remains mostly folklore. However, the issue of such variations becomes commercially important in large-scale production.²

3.1.1 Survey of mesoscale nonuniformity observations

Published reports on nonuniformities in thin-film devices are rare, and to our knowledge have never been reviewed. Yet, the available data show significant V_{oc} and electric current variations among nominally identical devices in noncrystalline thin-film structures. They

typically represent the results of device mapping using either direct electrical measurements or more sophisticated techniques, such as optical-beam-induced current (OBIC), electron-beam-induced current (EBIC), and scanning-tunneling microscopy (STM). Below we briefly review the results for several major materials.

For local microscopic V_{oc} measurements (also termed surface photovoltage for the case of devices without a metal contact), drastic lateral variations ranging from 0.2 to 0.7 V between different grains were detected by STM for a Cu(In,Ga)Se₂ polycrystalline PV device.³ These fluctuations were attributed to observed local variations in the film chemical composition. For similar devices, OBIC revealed microregions of reduced photovoltaic efficiency.⁴ The latter do not correlate with visible irregularities and were described as low V_{oc} regions. In large-area CuInSe₂ PV modules, long length scale (millimeter to centimeter) inhomogeneities were found to correlate with lower device performance.⁵ In particular, mapping of V_{oc} and other parameters revealed nonuniformities in average modules which were not present in the best modules. They were attributed to macroscopic imperfections such as defects in the glass substrate or contaminants in the film.

For CdS/CdTe polycrystalline PV cells, OBIC⁶ and EBIC^{7,8,9} showed strong inhomogeneities dependent on postdeposition treatments with length scales ranging from microns to millimeters. For CdTe PV modules, OBIC indicated considerable inter- and intra-cell variations,¹⁰ with the exception of some cases where cells were laterally quite uniform.¹¹ Time-resolved photoluminescence in CdS/CdTe solar cells revealed variations in recombination lifetime, by a factor of two to three across one cm distances.¹² Photoluminescence mapping¹³ also showed considerable nonuniformities on a large (~ 1 mm) scale whose topology depends on the excitation laser-beam power. Scanning ballistic electron emission spectroscopy (a variation on STM) revealed the barrier height dispersion of approximately 0.1 eV across an area of ~ 10 μm^2 in a crystalline CdTe/metal junction.^{14, 15} For the polycrystalline CdTe/CdS cell our STM mapping leads to results¹⁶ similar to those for CIGS in Ref. 3. Mapping of a polycrystalline CdTe cell fabricated with a high resistance contact¹⁷ showed ~ 0.3 eV electric potential variations over a 1 cm length scale and lateral nonuniformities in the temperature field distribution under 1 sun irradiation. Nonuniform degradation of short-circuit current in CdTe cells was noticed in Refs.¹⁸ and ¹⁹.

For the case of a-Si:H, changes in photoinduced degradation, defect density and PV parameters were found to depend on nano- and longer length scales of structural inhomogeneity.^{20,21} Lateral nonuniformities in V_{oc} , j_0 and other parameters were identified in micro-, multi-, and polycrystalline silicon.^{22,23,24, 25, 26} In particular, it was shown^{27, 28, 29} that forward current through a multi-crystalline cell does not flow homogeneously and is dominated by local sites of diode nature different from the standard ohmic shunts.

Schottky diodes have proven to be inhomogeneous even when based on crystalline semiconductors.^{30, 31, 32, 33, 34} This implies again that barrier-controlled electron transport is exponentially sensitive to local fluctuations in materials parameters. Existing theories attribute such fluctuations either to electric charge density (which affects the barrier height)³⁵ or to fluctuations in defect concentration that affect the barrier tunneling transparency.³⁶ Highly nonuniform charge flow induced by ionized defects within a crystalline semiconductor junction is evidenced also in the pitted submicron morphology obtained by photoetching.³⁷

Technologically, nonuniformity length scales ranging from microns to tens of centimeters can originate from different process steps. For example, polycrystalline film growth kinetics is generically nonuniform.³⁸ The dispersion in grain sizes translates into variations in the

curvature-dependent impurity gas pressure at grain boundaries which affects their doping levels and leads to micron-scale nonuniformities. Submicron nonuniformities originate then from the intragrain fluctuations in doping and stoichiometry.³⁹ Variations with length scales longer than the grain size are likely to be due to the postdeposition grain coarsening treatment.⁴⁰ Wet treatments and droplet dry-up can lead to nonuniformities with 100 μm to 1 cm scales governed by surface tension. Module-size length scales originate from nonuniformities in the deposition device. During the complete fabrication cycle, from deposition to final product, nonuniformities of different nature and length scales superimpose. We emphasize that the processes involved are intrinsically nonuniform and thus lateral inhomogeneities of the material parameters in large-area, thin-film devices are unavoidable.

3.1.2 Understanding laterally nonuniform devices

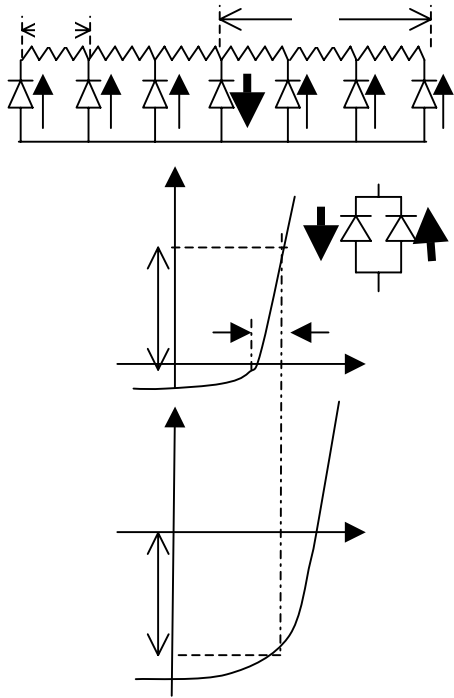


Fig. 3.1. Top: equivalent circuit of random microdiodes representing laterally nonuniform photovoltaic devices. Fat arrow shows shunting current (J_w) through the weak diode, with polarity opposite to that of the photogenerated currents supplied by the majority of diodes. L is the screening length. **Bottom:** The equivalent two-diode circuit (inset) and I/V characteristics of the weak diode (shunting the current J_w) and its more robust neighborhood (supplying the current $-J_w$). Because of the difference in the diode V_{oc} 's the weak diode finds itself under forward bias u .

The explanation of the lateral fluctuations under consideration lies in the device diode nature and in the presence of the resistive electrode. This is reflected in the equivalent circuit of random microdiodes of Fig. 2. The microdiode size is of the order of the nonuniformity length scale l .

In general, the effects of lateral micrononuniformities depend on the relationship between the nonuniformity length scale l and the screening length⁴¹

$$L(u) = \sqrt{u/\rho j_0} \quad , \quad (2)$$

where u is the local fluctuation of electric potential. The physical meaning of L is that the fluctuation u is supported by the resistive potential drop $j_0 L^2 \rho$. The latter applies to both the cases of $D=1$ and $D=2$. For $D=1$, ρL and $j_0 L$ represent the resistance and current, and ρ is understood as the resistance per unit length. For $D=2$, the resistance is represented by the sheet resistance ρ and the current is $j_0 L^2$.

The maximum screening length L_{\max} corresponds to a dead shunt ($u = V_{oc}$). The minimum screening length L_0 is defined by Eq. (2) with $u = kT/e$ (also derived in the study of lateral photoconductivity.⁴² Generally, the length L varies over a wide range depending on the sheet resistance and photocurrent. For example, a typical $L_0 \sim 1$ mm under 1 sun illumination, while under ambient room light (and correspondingly low current) L_{\max} can be as large as 1 m.

Eq. (2) describes screening of a point perturbation. For a system of multiple random diodes, we first point out a trivial case when the screening length is much shorter than the nonuniformity length scale ($l \gg L$) and the neighboring units are electrically insulated. The observed quantities then correspond to a locally tested microdiode. Note that because the regions at distances larger than L make no contribution, L sets the upper limit to the size of an efficient cell.

Given the range of L from $\sim 1\text{mm}$ to $\sim 1\text{m}$ and the much shorter fluctuation length scale l ($\sim 1\mu\text{m}$), the opposite limiting case of strongly interacting microdiodes, $l \ll L$ is practically important. This case is illustrated in Fig. 2 where two diodes in parallel mimic a weak element (low V_{oc}) and its more robust neighbors (high V_{oc}). The former finds itself under forward bias u and correspondingly strong positive current [cf. Eq. (1)]

$$j_w \approx j_0 \exp(eu / kT) \quad (3)$$

supplied by the diodes in the surrounding region within the screening length. A weak microdiode robs currents from a large number

$$N_L = j_w / j_0 = (L/l)^D \gg 1 \quad (4)$$

of its more robust neighbors, thereby significantly lowering the device efficiency. Such non-ohmic shunting does not affect the performance in reverse bias, as do the standard ohmic shunts.

Eq. (4) needs an obvious correction if there are several equally weak diodes in the region of the length L . More specifically, we note that, side by side with the above-defined L , there is another characteristic length describing the system of random diodes. This is the correlation radius R . Its standard physical meaning is that the system is macroscopically uniform on length scales longer than R . To estimate R we note that, in accordance with Eq. (1), the number of significantly different microdiodes in the system is $e\Delta/kT$, where Δ is the characteristic width of the V_{oc} distribution. Because each of the diodes has the linear dimension l , we find

$R = l(e\Delta/kT)^{1/D}$. The inequality $R \ll L$ is consistent with the available data. Replacing $L \rightarrow R$ and combining Eq. (4) with Eq. (3) gives the maximum local bias (across the weakest microdiodes) and the corresponding screening length in the system,

$$u_w = D \frac{kT}{e} \ln\left(\frac{R}{l}\right), \quad L_w = L_0 \sqrt{D \ln\left(\frac{R}{l}\right)}. \quad (5)$$

Thus, a weak diode is biased significantly, $u_w > kT/e$ and its screening length is macroscopically large, $L_w \gg l$.

In the above we have been assuming implicitly that the V_{oc} distribution has an effective cut-off width Δ . A conceivable alternative model assumes a probability distribution of open circuit voltages, $g(V_{oc})$, having a long exponentially decaying tail. In the latter case the situation is considerably different from that described by Eq. (5), that is, very rare but extremely weak diodes will rob the most current. The correlation length then becomes exponentially large and is

determined by the optimum fluctuation that finds the weakest diode with finite probability. This occurs when the product $g(V_{oc})\exp(-eV_{oc}/kT)$ is a maximum. Assuming, for example, the Gaussian distribution with the dispersion Δ^2 this model yields the correlation radius $R = l \exp\left[\left(\Delta e/kT\sqrt{D}\right)^2\right]$, which at low temperatures can be long enough to exceed both the screening radius and the linear dimensions of the device.

3.1.3 Mesoscale effects of micrononuniformities

Micrononuniformities have significant effects on the macroscopic voltage and current as well as the device degradation as discussed below.

Macroscopic voltage. The multi-diode circuit in Fig. 3.1 can be simulated by numerically solving the corresponding Kirchhoff's equations for a given random input parameter distribution (see more in detail below, Section 3.2). In Fig. 3.2 the calculated output parameter distributions show indeed weak microdiodes ($V > V_{oc}$) forcing strong

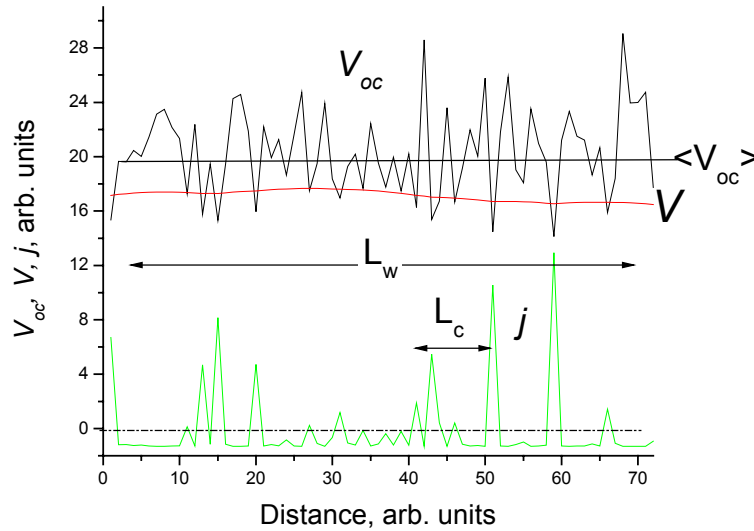


Fig. 3.2. Simulated open-circuit voltage (V_{oc}), electric potential (V), and transverse electric current (j) distributions in an open-circuit system of random diodes. Rare strong positive currents correspond to weak diodes balancing the majority of robust diode currents, which are negative. Note that the robust diode negative currents are practically the same as they would be under short-circuit conditions. The correlation radius (R) and the weak diode screening radius (L_w) are also shown.

positive currents. Under open circuit, they balance small negative currents flowing through the majority of microdiodes (with $V < V_{oc}$). The electric potential V varies much less than V_{oc} because its fluctuations are averaged out over $N \gg 1$ mutually interacting microdiodes.

For the case of $L \gg l$ it is possible to describe the macroscopic electric potential analytically. Consider $N \gg 1$ diodes occupying a volume of linear dimension $x \ll L$, but still macroscopically uniform in the sense $x \gg R$. Because $x \ll L$, the resistive potential drop

across the domain is relatively small and the diodes are under almost the same potential $\langle V \rangle$.

The latter can be found by setting to zero the sum of $N = (x/l)^D$ random currents [each given by Eq. (1) with $V = \langle V \rangle$],

$$\langle V \rangle = -\frac{kT}{e} \ln \left\langle \exp \left(-\frac{eV_{oc,i}}{kT} \right) \right\rangle_N. \quad (6)$$

Since $N \gg 1$, the above average is close to the true arithmetic average, which can be calculated based on the statistical distribution for V_{oc} . Following Eq. (6), the characteristic potential fluctuation is

$$\delta V = \frac{kT}{e\sqrt{N_L}} \frac{\delta [\exp(-eV_{oc}/kT)]}{\langle \exp(-eV_{oc}/kT) \rangle_{N_L}}. \quad (7)$$

where we have taken into account that independent fluctuations have a linear dimension $x = L_w$. Eqs. (6) and (7) agree well with the results of numerical simulations. For example, the uniform V_{oc} distribution with the lower bound $V_{oc,min}$ and width Δ is characterized by

$$\langle V \rangle = V_{oc,min} + (DkT/e) \ln(R/l), \quad \delta V = \Delta (l^2/L_w R)^{D/2}. \quad (8)$$

Note that since the balance of currents (rather than V_{oc}) determines the average macroscopic potential, the weak diode contribution is exponentially significant; in particular, a strong inequality $\langle V \rangle > \langle V_{oc} \rangle$ takes place, as is also illustrated in Fig. 3. In other words, under open-circuit conditions, the recombination of photogenerated electrons occurs mostly through weak diodes, as opposed to the ideal system where the recombination is spatially uniform. The degree of nonuniformity in local V_{oc} needed to cause the above qualitative difference is as low as several kT/e , well within the observed range of the V_{oc} fluctuation data.

Macroscopic current. Under working conditions, the current is partially consumed in the external circuit. Its flow corresponds to the electric field E_j , which is a maximum at the cell edge and vanishes at some point where the current is zero. For example, $E_j = 0$ at the open end in a 1D cell or at the center in a 2D round cell. At a point with coordinate $x \leq d$ one can estimate $E_j(x) \approx |j| \rho d(1 - x/d)$ for both the cases of $D=1$ and $D=2$, where j is the measured current density. In regions where the field is weak the conditions are close to that of open circuit. In such a quasi-open-circuit region weak microdiodes rob a significant amount of current. The size of that region is determined by the condition $E_j(x) = E_w$, where $E_w \approx u_w/L_w \approx \sqrt{u_w|j|\rho}$ is the weak microdiode field. Because the latter decreases with j slower than $E_j \propto j$, it is clear that the size of the quasi-open-circuit region increases and weak microdiodes become more important at low currents. More specifically, the dimension of the region is $\Delta x = L_w$. As seen from the definition of L_w in Eq. (5), Δx and the current loss decrease with $|j(V)|$ and are almost

minimum under short-circuit conditions where the current is close to its maximum value. Forward bias decreases $|j(V)|$, thus increasing L_w and the current loss. As a result the curvature of the I/V becomes more gradual than that of the ideal diode. The latter feature is often observed and referred to as low fill factor (FF).

Degradation. Another significant effect is nonuniform degradation,^{17, 18} caused by the electric current localization in a weak microdiode. This entails a corresponding increase in the carrier concentration, local surface charge, and Joule heat. The related degradation mechanisms are (i) electromigration of impurity ions; (ii) accelerated defect creation by excessive local carrier concentration; (iii) local electrochemical modification (corrosion, *etc.*) induced by ions from the ambient attracted to the excessive electric charges in the weak microdiode ends; (iv) direct action of locally increased current or heat. All the above mechanisms will make the originally weak microdiodes degrade still more, thus increasing the degree of nonuniformity and accelerating the degradation: the laterally nonuniform system turns out to be unstable under light-induced or other bias. This issue will be more in detail discussed in Section. 3.4 below.

3.1.4 Blocking the effects of nonuniformities

As a semiconductor thin-film device is deposited, not much can be done to improve its disordered structure. The known remedies are chemical treatments (such as CdCl_2 for CdTe photovoltaics) and anneals,⁴³ which increase and equalize grain sizes and otherwise promote uniformity.

Here we would like to point toward other remedies, which, while keeping the semiconductor structure intact, can significantly reduce the device nonuniformity. As is seen from Fig. 2, the steeper the I/V curve in the forward bias region $V > V_{oc}$, the stronger the impact of a weak diode. (In particular, the exponential bias dependence in Eq. (1) led to the exponentially strong weak diode effects as discussed above.) The exponential steepness is known to reduce to a linear bias dependence when there is a considerable series resistance added to the elemental diode. Hence, increasing the series resistance will mitigate the detrimental effects on micrononuniformities. We verified the latter argument by numerically simulating the circuit in Fig. 2 with series resistances added to each of the random diodes: a significant suppression of the electric current and electric potential lateral fluctuations was indeed observed.

The above prediction of the beneficial role of series resistance has two practical implications. First, the general quest for decreasing the device series resistance may not be justified in all cases. While this minimizes the ohmic loss, it can simultaneously promote losses due to micrononuniformity effects. The analysis above shows that the series resistance should be carefully optimized to compromise between the ohmic and the micrononuniformity-related losses. Such optimization should open opportunities in thin-film device engineering.

The second implication has to do with buffer-layer effects, which, while proven generally positive, remain poorly understood. We recall that the buffer layer is generally a resistive, thin layer placed between the semiconductor and TCO. Because of its small thickness, it does not add much to the device series resistance. In the mean time it is known to minimize current losses in the device and in some cases to improve the device stability. From the perspective of this paper, a beneficial effect of the buffer layer is that it adds series resistances to the weak diodes (or shunts). In understanding this effect it is crucial to take into account the characteristic micrononuniformity size l . The series resistance of the “clog” added by the buffer layer to a

weak diode or shunt, $r_{bl} \propto l^{-2}$ is significant for small size micrononuniformities, but may have no effect on nonuniformities of considerable lateral dimensions. Hence, the same buffer layer may or may not have positive impact on the device performance and stability, depending on details of the device technology affecting the micrononuniformity length scale. We believe that the buffer layer should be optimized based on the device uniformity characteristics.

Finally, we note that the above-discussed physics not only explains how nonuniformities are detrimental to device performance and stability, but also suggests a certain way of leveling them out. Namely, because the surface potential (local V_{oc}) under the light varies across a semiconductor film, electrochemical treatments sensitive to the electric potential will act differently at different spots. When properly chosen they should deposit clogs onto the weak diode spots while leaving the robust parts of the film practically intact, thus eliminating the most significant sources of nonuniformity effects. It is likely that in some cases such treatments have already been found in several cases by trial and error. In particular, that might explain why different pre-contact treatments, including weak etches and exposure to organics have a profound effect on device parameters. We believe that our present consideration provides the understanding to search effectively for the desired treatments.

3.2 Numerical modeling of laterally nonuniform devices

3.2.1 Model

Our model of laterally nonuniform photovoltaics (Fig. 3.3) consists of a set of random diodes connected in parallel through a resistive electrode. Each microdiode is described by a non-ideal I/V characteristic

$$\ln \left(\frac{I + I_L}{I_S} - \frac{V - IR_S}{I_S R_{sh}} + 1 \right) = \frac{q}{kTA} (V - IR_S). \quad (9)$$

I_L and I_S are the light-generated and saturation currents, R_S and R_{sh} are the series and shunt resistances, q is the electron charge, k is the Boltzmann's constant, and T is the temperature. The resistive connectors between the diodes mimic the TCO. The resistor resistance R is one other model parameter. The diode parameters are random and are characterized by their probabilistic distributions. The random parameters are not correlated spatially.

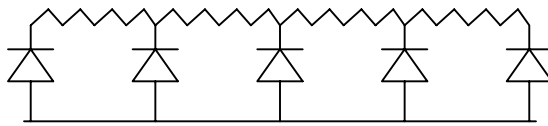


Fig. 3.3. Equivalent circuit representing laterally nonuniform photovoltaics

The model can represent either one-dimensional (1D) or 2D systems. In what follows we concentrate on the 1D case. Note that the model does not specify the number N of microdiodes per device length (or area) in Fig. 3.3. The number N remains arbitrary and can be set depending on desired spatial resolution.

To make Eq. (9) dimensionless we adopt the following units

$$\begin{aligned}
\frac{kTA}{q} &\equiv u \quad \text{for } V \text{ and } V_{oc}, \\
I_L + I_S &\equiv i \quad \text{for } I, \\
\frac{kTA}{q(I_L + I_S)} &= \frac{u}{i} \equiv r \quad \text{for } R_S \text{ and } R_{sh}
\end{aligned} \tag{10}$$

We also take into account the relation

$$V_{oc} = \frac{AkT}{q} \ln \left(\frac{I_L + I_S}{I_S} \right), \tag{11}$$

which defines the open circuit voltage for a nonleaky ($R_{sh}=0$) diode.

As expressed in the latter units, Eq. (1) becomes

$$\ln \left[I + 1 - \frac{(V - IR_S)}{R_{sh}} \right] = V - V_{oc} - IR_S. \tag{12}$$

3.2.2 Model parameters

Diode parameters. The units defined in Eq. (10) and the CdTe photovoltaics measured parameters have the following characteristic values.

$$\begin{aligned}
u &= 0.025 - 0.1 \text{ V (depending on } T \text{ and } A) \\
i &= 0.02 \text{ A/cm}^2, \quad r = 1 \Omega * \text{cm}^2, \\
V_{oc} &= 0.8 \text{ V}, \quad V \sim V_{oc}, \\
R_S &= 2 - 10 \Omega * \text{cm}^2 \text{ (depending on device quality),} \\
R_{sh} &\sim 10^4 \Omega * \text{cm}^2 \text{ (depending on device quality)}
\end{aligned} \tag{13}$$

The presence of cm^2 in the above units reflects the fact that the available data on I_L and I_S are measured in A/cm^2 . From the modeling point of view, it reflects the model discreteness. Taking into account that R_S and R_{sh} enter the equations in a product (with i), which does not contain the dimensionality of length, it is possible to omit in the estimates in Eq. (13) the units of cm^2 . With that in mind, the characteristic dimensionless parameters become

$$V_{oc} \sim 10 \div 30, \quad R_S \sim 1, \quad R_{sh} \sim 10^4. \tag{14}$$

Resistor parameter. The above-mentioned uncertainty in the number N of the microdiodes per device length or area translates into the uncertainty in the resistor parameter R , which should be set based on desired spatial resolution. The latter can be conveniently defined in comparison with the natural lateral dimension in the system, which is the screening length L ,

$$L = \sqrt{\frac{V_{oc}}{j_L \rho}} \quad (15)$$

where ρ is the TCO sheet resistance. Its physical meaning is the characteristic length, over which the system “feels” the presence of a point perturbation (e. g. shunt) [44]. Varying R to give a desired number of microdiodes (and thus the number of data points) over the length L will tune the spatial resolution. This is practically done by setting disorder to zero and shunting one of the circuit ends while leaving the opposite end of the circuit open. The computer program (described below) will then generate voltages across each of the microdiodes starting from zero at the shunted end and then saturating to V_{oc} far from that end. The desired number of diodes in the region of varying voltage determines the resistor parameter R . This is illustrated in Fig. 3.4, which shows indeed that choosing R too small (Fig. 3.4b) gives too much spatial resolution, such that the potential does not saturate across the sample (which turns out to be shorter than L); on the other hand, higher R (Fig. 3.4a), makes L short enough to let the potential saturate and thus to catch the main qualitative features in the system behavior. In particular, choosing R of the order of or even larger than in Fig. 3.4a seems to be appropriate if we wish to model electric potential and current fluctuations in the system.

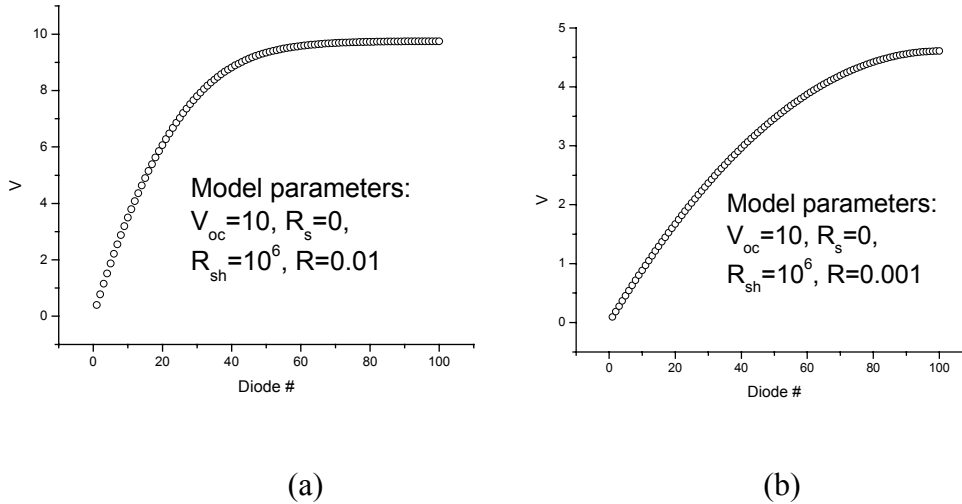


Fig. 3.4. Electric potential distribution in a shunted 1D diode circuit for two different resistor parameters.

3.2.3 Numerical algorithm

Our software⁴⁵ utilizes the standard Kirchhoff's rules for the electric circuit in Fig. 3.3: (1) the sum of potential differences encountered in a round-trip around a closed loop is zero and (2)

the sum of the currents toward the branch point is equal to the sum of the currents away from the same point. This reduces to the equations

$$\begin{aligned}
 I_R(n) &= \frac{V(n) - V(n+1)}{R(n)}, \\
 I_R(n) + I(n) - I_R(n+1) &= 0, \\
 \ln \left[I(n) + 1 - \frac{(V(n) - I(n)R_s(n))}{R_{sh}(n)} \right] &= V(n) - V_{oc}(n) - I(n)R_s(n)
 \end{aligned} \tag{16}$$

Here $I_R(n)$ is the current through the n -th R -resistor, which by convention is to the right of the n -th branch point belonging also to the n -th diode in the circuit.

The parameters $V_{oc}(n)$, $R_s(n)$, $R_{sh}(n)$ [and if necessary $R(n)$] are generated as random numbers uncorrelated between different elements with probabilistic distributions of either Gaussian or uniform shapes. The system in Eq. (16) is then solved by iterations [by the Newton's algorithm] to give as the output the bias $V(n)$ and current $I(n)$ for each of the diodes and the current $I_R(n)$ through each of the resistors.

The following boundary conditions are made possible in solving the above system: (1) Fixing either I or V at each of the two ends, or (2) Cyclic boundary conditions when the two ends are connected. For example, setting $V=0$ implies the shunted end while $I=0$ corresponds to an open end.

The number N of diodes in the system is also considered a parameter, whose value is determined by desired spatial resolution and technical parameters of a computer at hand (the computing time increases roughly as N^2).

3.2.4 Running the program

The program consists of two blocks, the first one to generate the individual circuit element parameters, and the second one to solve the system in Eq. (16) with the parameters generated and thus to create the output (Fig. 3.5).

To start the program:

the following files need to be copied into the same directory: DDG.exe, Input.txt, DDV.exe, PrgPrm.txt, NewtPrm.txt.

To run the program:

1. Double click on Input.txt. This will open a text file where several setting should be defined.
 - a) Number of diodes: simply type into the number (by default is 100), ranging from 100 to 3600 (Note, computing time will increase!)
 - b) Boundary conditions: examples are given in the table below

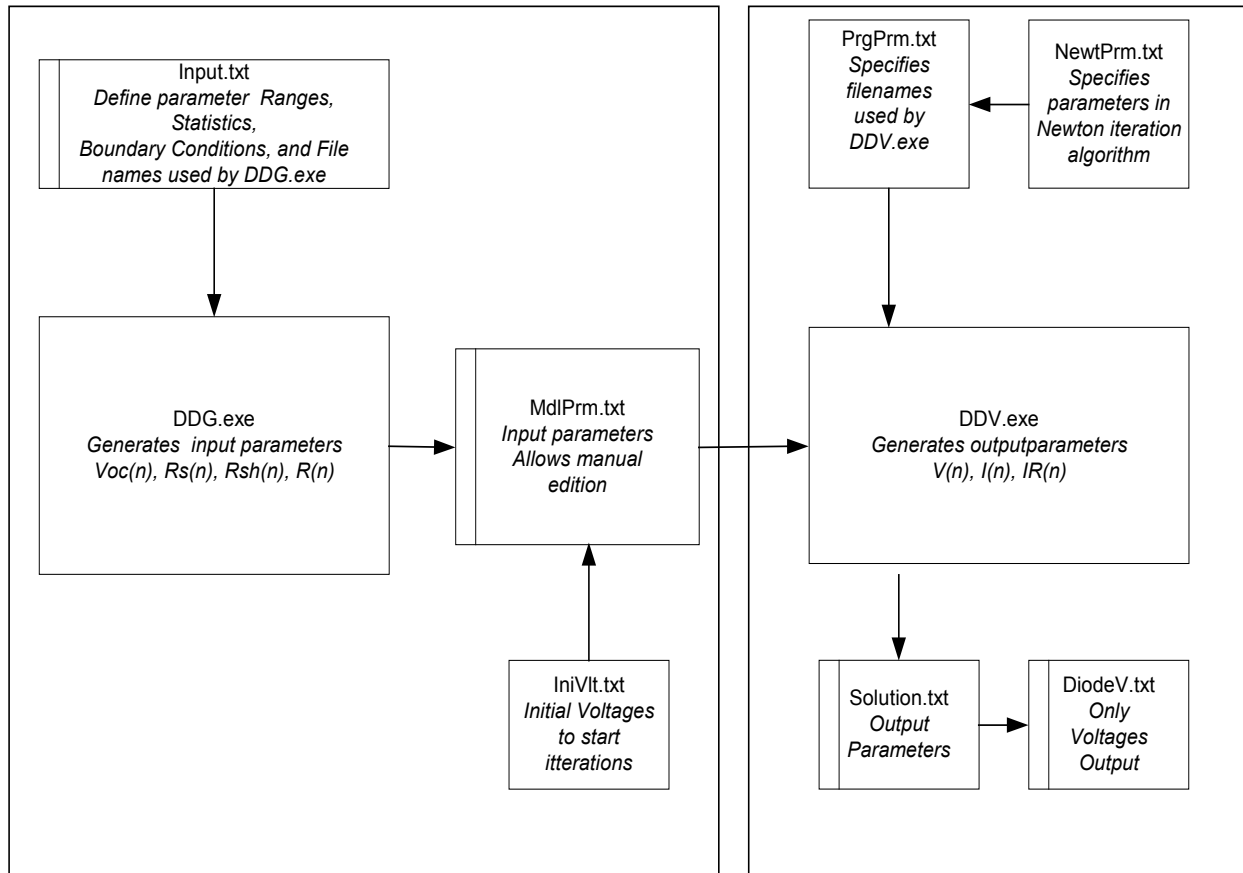


Fig. 3.5 Data Flow and execution in the computer program solving a random diode circuit

Fully open circuit		Left end open, other shunted		Load I/V		Cyclical
I	I	I	V	V	I	C
0	0	0	0	Set of V's	0	Line blank

- Distributions and their parameters: use letter F and two numbers for uniform distribution in the format F, Mean, Maximum Deviation, or use G and two numbers for the Gaussian distribution in the format G, Mean, Standard Deviation.
 - Different seed values for random numbers (-1, -2...) will generate different sets of random numbers.
 - Initial values for diode voltages can, as a rule of thumb, be set twice as small as the average Voc to make iterations converging fast.
- Save file Input.txt.
 - Double click on DDG.exe to generate MdlPrm.txt and IniVlt.txt. *Note:* if needed the file MdlPrm.txt can be edited manually (and then saved). This may be useful in adding to the system some additional distinctive features, such as shunts at certain points, extremely bad diodes (beyond the statistical distribution limits, etc.).
 - Double click on DDV.exe to generate Solution.txt and DiodeV.txt. *Note:* the program writes over the latter files each time it runs. Therefore, to keep useful output do not forget to save it in a file with a unique name.

3.2.5 Examples

We consider below several examples of how the program can be used.

1) Electric potential and current fluctuations in an open circuit linear system are induced by a Gaussian distribution of V_{oc} , other parameters being fixed; the screening length ($L \sim 50$) is much smaller than the system size $N=500$. As is seen from Figs. 3.6 and 3.7 the following trends take place.

- (i) The electric potential fluctuates much less than V_{oc} , which is natural as the original V_{oc} fluctuations are suppressed by averaging out over the distances of the order of the screening length.
- (ii) The majority of the diode currents is uniformly negative (note the black background below the horizontal axis) and corresponds to the light-induced current components in the diodes. They are completely balanced by much less likely but very large positive local recombination currents, whose presence is strongly correlated with the appearance of weak V_{oc} in the system. This observation reintroduces the notion of weak diode in laterally nonuniform photovoltaics (earlier introduced in Ref.⁴⁶).

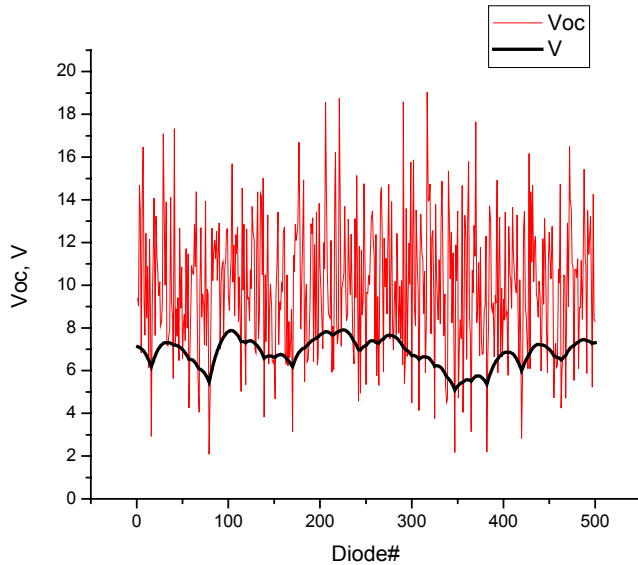


Fig. 3. 6. Spatial distributions of V_{oc} and electric potential V in a linear system of random diodes

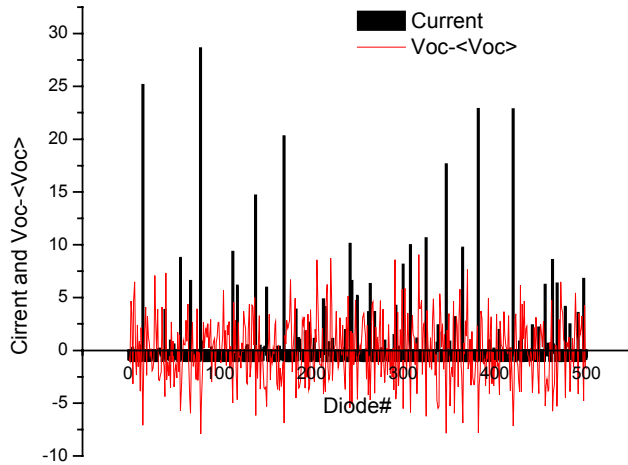


Fig. 3.7 Spatial distributions of Voc fluctuations and electric current in the same system.

- (iii) Modeling of this kind enables one to collect the statistics of different events, such as the shunting currents running through the weak diodes. This is illustrated in Fig. 3.8, where probabilistic distribution for the currents is determined based on the data in Fig. 3.7 and where solid line shows analytical approximation.

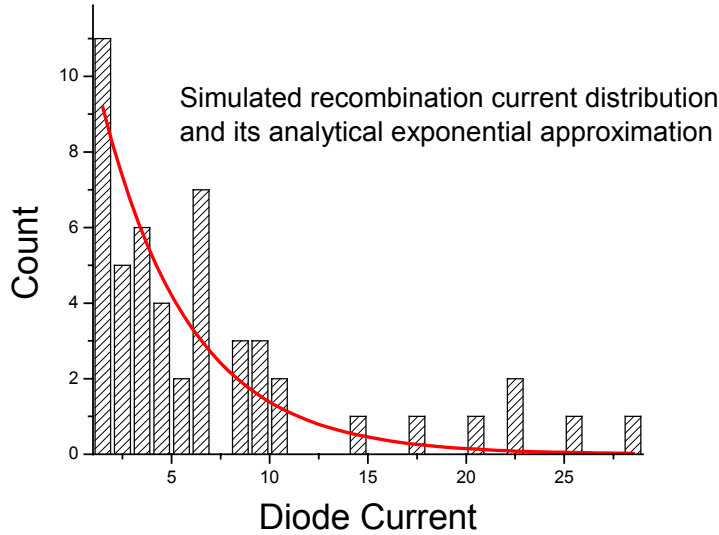


Fig. 3.8. Statistical distribution of recombination currents in a linear circuit of random diodes.

2) The next example shows how to model I/V characteristics of laterally nonuniform PV devices. The idea of modeling is illustrated in Fig. 3.9. As we fix voltage (V) at the left end the system generates currents in all its resistors including the first one (I) that connects the system to the voltage source; thus the desired characteristics $I(V)$ is defined.

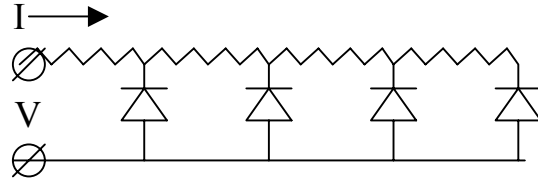


Fig. 3.9. Equivalent circuit for modeling I/V characteristics of nonuniform photovoltaics.

Shown in Figs. 3.10 and 3.11 are examples of simulated I/V curves. Following Ref. 44 we discriminate between the cases of small ($l \ll L$) and large ($l \gg L$) cells depending on the relationship between the cell size (l) and the screening length L . In the former case (usually implied in all the semiconductor device handbooks) bias is distributed in a uniform fashion over the cell length; in the latter case it is restricted to the region L , which itself is bias-dependent. In our examples we kept the average $\langle V_{oc} \rangle = 10$ and either considered uniform systems or allowed V_{oc} random fluctuations uniformly distributed in the interval from 5 to 15. The following trends are seen.

- (i) For small cells the disorder hits mostly the cell V_{oc} and fill-factor and does not affect the short circuit current. The way it acts depends on the disorder realization: different realizations (thus, different cells on a substrate) will show slightly different I/Vs.
- (ii) For large cells the disorder attacks V_{oc} , J_{sc} and fill-factor.

Of course, much more work is called up to study how I/V curves depend on the disorder characteristics. What seems to be obvious even at this stage though is that the effects of lateral disorder may be responsible for numerous deviations of the observed I/V curves from that of an ideal diode, which needs to be taken into account simultaneously with speculating about the diode structure in the direction perpendicular to the junction (typically by AMPS software).

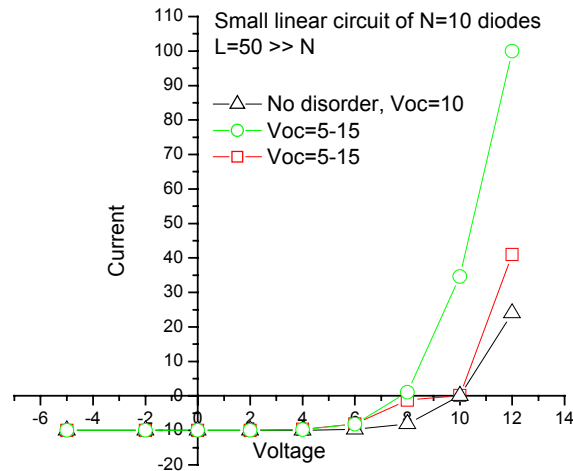


Fig. 3.10 Numerically simulated I/V curves of small cells with and without lateral nonuniformities.

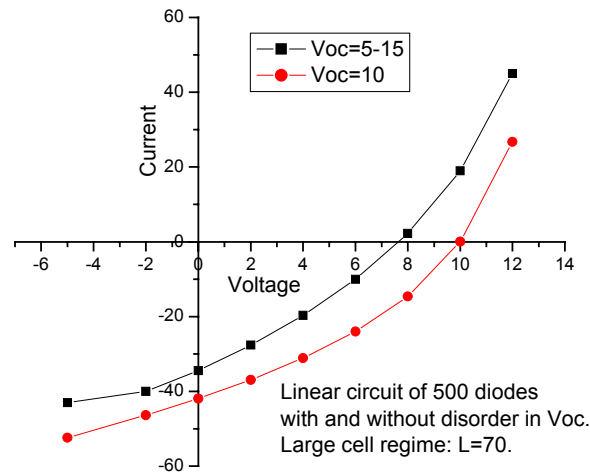


Fig. 3.11. Numerically simulated I/V curves of large cells with and without lateral nonuniformities.

3.3 Nonuniform degradation

We have carried out experiments where solar cells were made artificially nonuniform before putting them under light soak. In a set of roundish CdTe/CdS dot cells, each cell was half shadowed along its diameter. After one month light soak the screens were removed and the devices were scribed along their diameters, to make the former dark and light parts electrically disconnected. We have intentionally chosen devices with a broad range of deposition parameters: some of them degraded, others improved under limited time exposure. As a control we light-soaked a number of fully open cells.

The data shown in Fig. 3.12 reveal that there was no preference of the light over the dark halves in the amount of degradation. This is consistent with the concept that this is not the light per se, but rather its generated forward electrical bias, which is responsible for the device degradation. The light-generated screening radius $L > 1$ cm, estimated from our Eq. (2) turns out to be long enough to let the bias spread over the entire cell.

In addition, Fig. 3.12 b shows that, to the first approximation, the sum of the light and dark halves J_{sc} degradation is constant ($\sim 6-8\%$). The latter turns out to be larger by approximately a factor of two than that of our control fully open cells ($\sim 3-4\%$). This difference can be understood if J_{sc} degradation is significantly nonuniform and occurs in either half of the cell. Small current density degradation in the control cells is then explained by mistakenly relating the current degradation to the area that is overestimated by a factor of two (whole cell instead of half of a cell).

In general, the data in Fig. 3.12 reveal that there are degradation mechanisms of different length scales. In particular, V_{oc} degradation turns out to be more uniform than that of J_{sc} . This means that the bad diode contribution to the measured (average) V_{oc} is relatively immaterial, as opposed to the current, which is dominated primarily by the weakest diode in the system. This property of V_{oc} can be proven indeed by using the explicit (parabolic) coordinate dependence of the electric potential distribution caused by micro shunts.

The above experiments indicate that the cause for degradation is the light-generated forward bias and are consistent with the model of weak diodes responsible for nonuniform degradation. Weak microdiodes (of low open circuit voltage) were shown to affect

macroscopically large regions where they strongly reduce the device performance and induce its nonuniform degradation in several different modes.

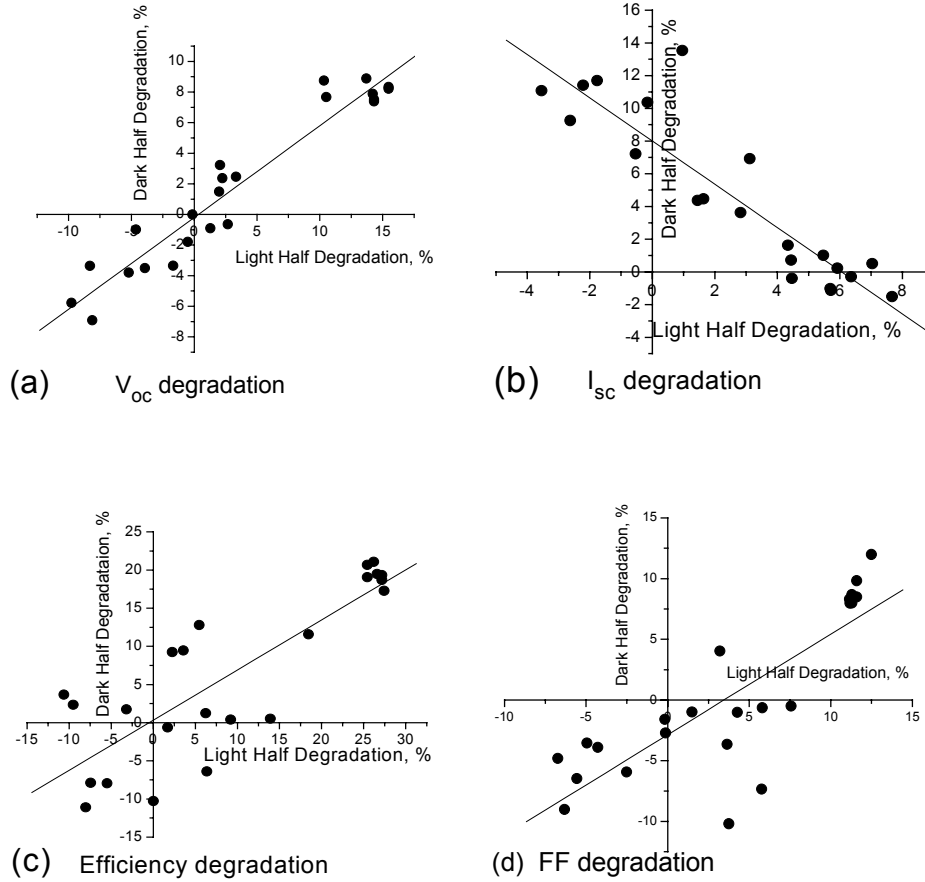


Fig. 3.12 Degradation of different parameters in a set of artificially nonuniform cells.

New experiments are now being designed to further verify the concept of nonuniform degradation. One such experiment is aimed at tracking nonuniformity in the cell corrosion, which process can start at weak micro-diodes to spread over the entire system. Also, smaller degraded cell partitioning (in 4, 8, etc. parts) will show nonuniformity in degradation of different cell parameters.

3.4 Nonlocal photovoltaic response

In many applications nonequilibrium electrons and holes in a p-n junction are created nonuniformly in the lateral direction. One example is a laser generated electron-hole plasma. Charge carrier generation by a uniform light in laterally nonuniform photovoltaics exhibits another such example. It is typically assumed in the above applications that the nonequilibrium carriers do not propagate far from their birthplace. This hypothesis of locality has numerous

implications. In particular, it underlies PL, micro-PL, EBIC, and OBIC mapping techniques of studying material local properties.

We have challenged the above hypothesis and have found, to the contrary, that light-generated electrons can travel in the lateral directions across very significant distances determined by the lateral conduction mechanism. We discriminated between the case of finished devices and that of devices before metallization. In the context of our study the main difference was that in the former device, lateral conduction is dominated by the TCO sheet resistance, as opposed to the latter where the TCO sheet resistance is relatively immaterial and the lateral conductance is due to CdTe layer sheet resistance (Fig. 6).

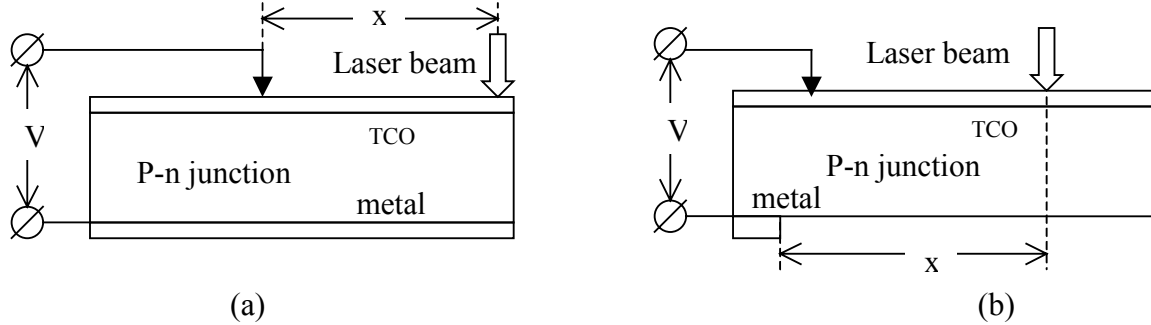


Fig. 3.13. Side view of the one-dimensional setup for studying voltage vs. distance (x) from the laser beam for the cases when the lateral spreading is dominated by (a) TCO, (b) the semiconductor layer. The total device thickness was in the range 3 – 4 μm . The drawing does not show a relatively thick (3 mm) glass substrate above the TCO.

We have measured the open circuit voltage (V_{oc}) vs. distance from the laser beam. Our typical data are shown in Figs. 3.14 and 3.15. The characteristic decay lengths are very different

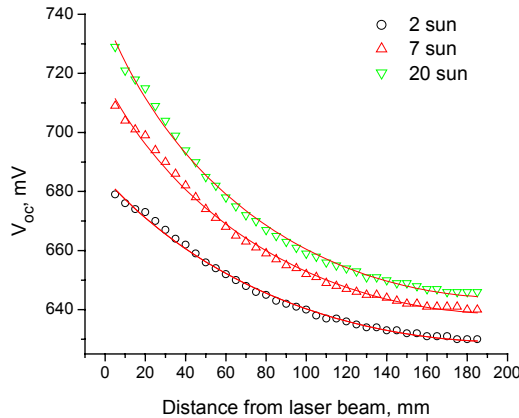


Fig. 3.14. Nonlocal V_{oc} vs. the distance from the laser beam in 1D cell with the TCO dominated lateral spreading for different excitation powers: data and theoretical fits.

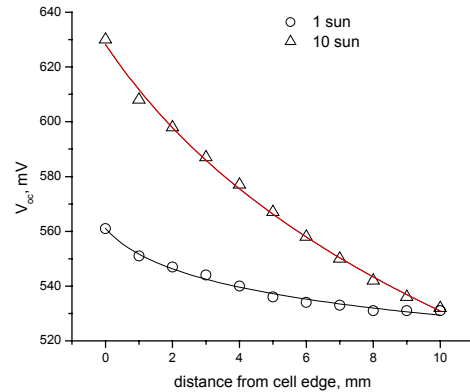


Fig. 3.15. V_{oc} vs distance from the 2D cell edge for semiconductor dominated lateral spreading for two different laser powers in comparison with theoretical fits. Excitation from the glass side with the laser of 752 nm wavelength.

for the above-mentioned two classes of devices. For the TCO dominated lateral conduction it turns out to be very large approaching 1m, while it remains in the range of tenths of mm for the semiconductor dominated lateral spreading. The decay shapes for one-dimensional (1D) and 2D

cells were found to be almost the same (Fig. 3.16), with practically no difference between the front- and back-wall excitations (Fig. 3.17). Magnetron-sputtered and VTD samples showed similar features, both demonstrating that ambient light has no effect on the observed decay (except the cutoff at the ambient V_{oc}). We have developed a theory¹³ that provides a good quantitative description of our data for the case of TCO-dominated lateral spreading and remains a reliable semiquantitative guide for the semiconductor-dominated lateral conductivity where effects of lateral micrononuniformity bring about some features beyond the theory. The theory explicitly takes into account that the recombination current between the electrons and holes is determined by the diode I/V characteristic, the latter being exponential. As a result, the lower the electron-hole pair concentration (far from the beam), the smaller the voltage across the film and thus exponentially lower the recombination rate. This leads to the voltage decaying logarithmically with the distance from the source (laser beam in our case); the agreement between the theory and experiment is illustrated in Figs. 3.14, 3.15, and 3.17-3.19 by solid lines.

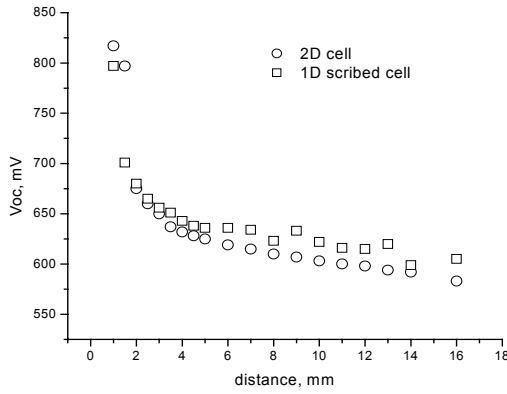


Fig. 3.16. V_{oc} spatial decay vs distance from the laser beam for a dot (2D) and a linear (1D) cell scribed from the 2D dot cell.

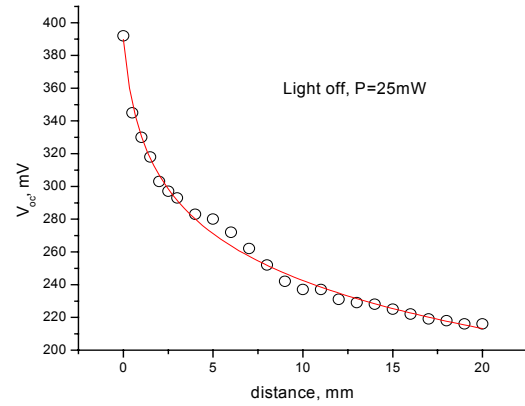


Fig.3.17. Spatial decay of surface voltage in the case of back wall excitation. Solid line represents theoretical fit.

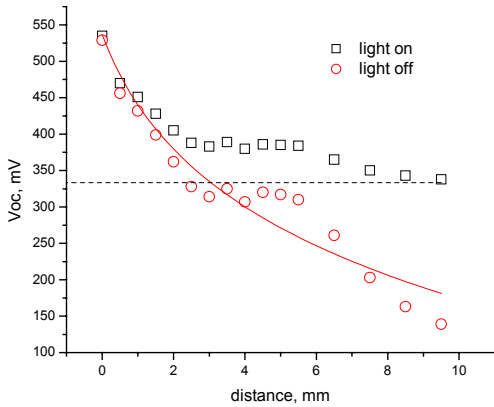


Fig. 3.18. V_{oc} vs. distance from the laser beam for ambient light on and off. Magnetron-sputtered sample. Dashed line shows the saturated V_{oc} for the sample under ambient light.

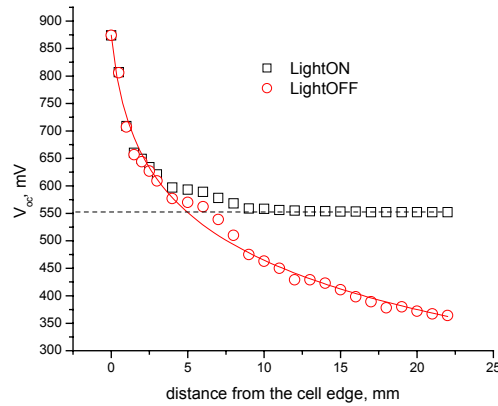


Fig. 3.19. Same as in Fig. 3.18 for a vapor-transport deposited sample.

As the laser-generated plasma spreads, not only does it produce voltage changes, it can also emit light from the areas beyond the beam spot. In particular, this may be evidenced in the difference between the same area photoluminescence (PL) maps measured at different excitation powers, 2 suns and 20 suns (Fig. 3.20 a, b). Note that the low intensity map shows the presence of the sample edge ($y=0$) at a distance of several millimeters, while it is not seen under the high intensity laser beam.

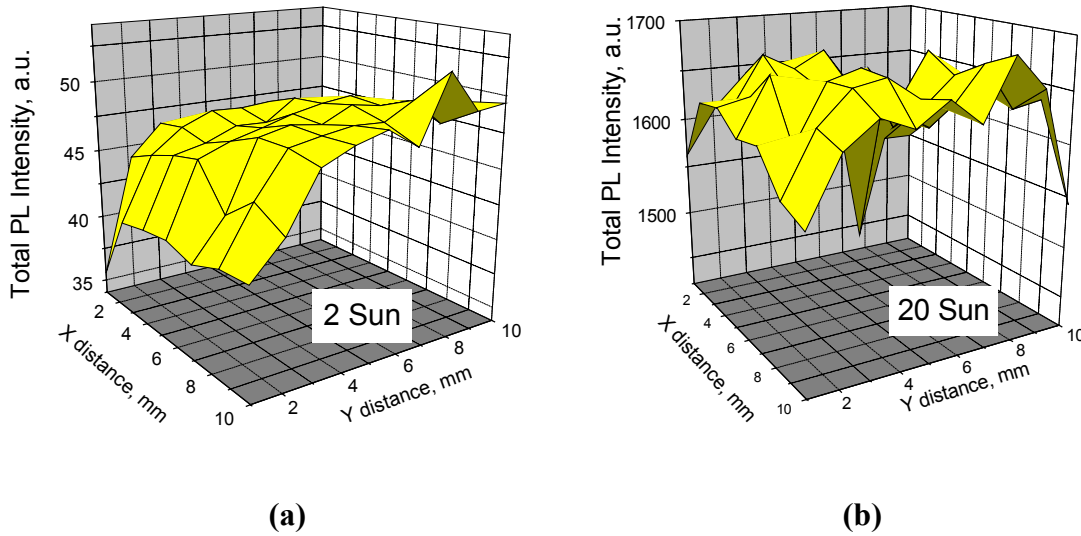


Fig. 3.20. PL maps corresponding to two different excitation powers show different: a) 2 sun, b) 20 sun.

Some practical implications of the above results are that (1) measuring the spatial decay of the open circuit voltage in a completed cell enables one to establish the dependence of the laser-generated current on the excitation power, which characterizes the device efficiency and recombination properties. (2) The same measurements can be used to estimate the TCO sheet resistance in a completed device. For the case of semiconductor-controlled lateral spreading, practical implications can be related to the established unexpectedly low semiconductor layer sheet resistance. A consequence of it may be current loss caused by semi-shunts, which are metal protrusions penetrating the semiconductor film partially from one of the contacts. (3) The spatial resolution of the photoluminescence mapping under open circuit conditions was shown to strongly depend on the excitation power.

3.5 Conclusion

In conclusion, we have shown that large-area semiconductor devices are intrinsically nonuniform, which makes their physics qualitatively different from that of microelectronics. The nonuniformity length scales cover a broad spectrum ranging from microns to meters. They show up in many different types of experiments and for the majority of thin-film semiconductors. We have also found a characteristic screening length that ranges from millimeters to meters and explains how a microscopic nonuniformity can affect macroscopically large areas in the film. Our theoretical model (of random diodes) explained some of the observed features. We described the electric current and potential fluctuations and their effect on the main parameters of thin-film

devices. Our consideration here has suggested certain ways of overcoming these nonuniformity effects.

Another closely related application should be mentioned where the concepts of nonuniformity and random diode arrays can be extremely important, which is the macroscopic circuitry of large area PV modules and their field arrays. A typical PV module is composed of a large number linear cells in series. Because of the cell diode nature, these series will be very sensitive to small variations in the cell parameters; hence, the problem of random diodes in series. Furthermore, in the field, photovoltaic arrays form more complex circuits where, for example, blocks of many modules in parallel are connected in series. Again, since the modules have slightly different characteristics, the latter systems will belong to the class of random diode systems. A relevant theoretical approach is needed to understand their physics and optimize the design.

References

- ¹ S. M. Sze, Physics of semiconductor devices, John Wiley & Sons, New York 1981.
- ² H. S. Ullal, K. Zweibel, and B. G. von Roedren, Polycrystalline thin-film photovoltaic technologies: from the laboratory to commercialization, *Proc. 28th IEEE Photovoltaic Specialists Conference*, Alaska, p. 418 (2000).
- ³ D. Eich, U. Hereber, U. Groh, U. Stahl, C. Heske, M. Marsi, M. Kiskinova, W. Reidl, R. Fink, E. Umbach, Lateral inhomogeneities of Cu(In,Ga)Se₂ absorber films, *Thin Solid Films*, Vol. 361-362, p. 258 (2000).
- ⁴ G. A. Medvedkin, L. Stolt and J. Wennerberg, Optoelectronic images of polycrystalline thin-film solar cells based on CuInSe₂ and CuInGaSe₂ obtained by laser scanning, *Semiconductors*, Vol. 33, p. 1037 (1999).
- ⁵ J. Ermer, R. Gay, D. Pier, and D. Tarrant, Challenges and progress in the scale up of CuInSe₂ thin film photovoltaic technology, *J. Vac. Sci. Technol.*, Vol. A11, p. 1888 (1993).
- ⁶ S. A. Galloway, A. W. Brinkman, K. Durose, P. R. Wilshaw, and A. J. Holland, A study of the effects of post-deposition treatments on CdS/CdTe thin film solar cells using high resolution optical beam induced current, *Appl. Phys. Lett.*, vol. 68, p. 3725 (1996).
- ⁷ P. R. Edwards, S. A. Galloway, and K. Durose, EBIC and luminescence mapping of CdTe/CdS solar cells, *Thin Solid Films*, Vol. 372, p. 284 (2000).
- ⁸ R. Harju, V. G. Karpov, D. Grecu, G. Dorer, Electron-beam induced degradation in CdTe photovoltaics. *J. Appl. Phys.*, Vol. 88, p. 1794 (2000).
- ⁹ T. J. McMahon and B. von Roedern, Effect of light intensity on current collection in thin-film solar cells, *Proc. 26th IEEE Photovoltaic Specialists Conference*, Anaheim, CA, p. 375 (1997).
- ¹⁰ I. L. Eisgruber, R. J. Matson, J. R. Sites, and K. A. Emery, Interpretation of laser scans from thin-film polycrystalline photovoltaic modules, *Proceeding of the 1st World Conference on Photovoltaic energy Conversion*, p. 283, Hawaii (1994).
- ¹¹ P. N. Gibson, M. A. Baker, E. D. Dunlop, M. E. Ozsan, D. Lincot, M. Froment, G. Agostinelli, Correlation of chemical and structural parameters with non-uniform cell performance in CdS/CdTe solar cells, *Thin Solid Films*, Vol. 387, p. 92 (2001).
- ¹² R. K. Ahrenkiel, B. M. Keyes, D. L. Levi, K. Emery, T. L. Chu, and S. S. Chu, Spatial uniformity of minority-carrier lifetime in polycrystalline CdTe solar cells, *Appl. Phys. Lett.*, Vol. 64, p. 2879 (1994).

-
- ¹³ Diana Shvydka, A. D. Compaan and V. G. Karpov, Nonlocal response in CdTe photovoltaics, *J. Appl. Phys.*, Vol. 91, p. 9059 (2002).
 - ¹⁴ I. M. Dharmadasa, C. J. Blomfield, C. G. Scott, R. Coratger, F. Ajustron, and J. Beauvillain, Metal/n-CdTe interfaces: a study of electrical contacts by deep level transient spectroscopy and ballistic electron emission spectroscopy, *Solid State Electronics*, Vol. 42, p. 595 (1998).
 - ¹⁵ C. F. Alonso, M. P. Hernandez, E. Cassiellas, and J. L. Pena, Determination of the barrier-height fluctuations based on parallel-noninteracting diode model, *Appl. Phys. Lett.*, Vol. 80, p. 3751 (2002).
 - ¹⁶ Diana Shvydka, A. D. Compaan and V. G. Karpov, unpublished.
 - ¹⁷ V. G. Karpov, R. Harju, and G. Dorer, Nonuniform power generation in polycrystalline thin-film photovoltaics, *Proc. 28th IEEE Photovoltaic Specialists Conference*, Alaska, p. 547 (2000).
 - ¹⁸ V. G. Karpov, A. D. Compaan, and Diana Shvydka, Effects of nonuniformity in thin-film photovoltaics, *Appl. Phys. Lett.* Vol. 80, p. 4256 (2002).
 - ¹⁹ A.O. Pudov, M. Gloeckler, S.H. Demtsu, and J.R. Sites, K.L. Barth, R.A. Enzenroth, and W.S. Sampath, Effect of back contact copper concentration on CdTe cell operation. , *Proc. 29th IEEE Photovoltaic Specialists Conference*, New Orlean (2002), to be published.
 - ²⁰ N. Sakikawa, M. Tamao, S. Mayazaki, and M. Hirose, Correlation between light-induced degradation and structural inhomogeneities in hydrogenated amorphous silicon prepared under high-rate deposition conditions, *Jpn. J. Appl. Phys.*, Vol. 37 p. 432 (1998); Structural inhomogeneity in hydrogenated amorphous silicon in relation to photoelectronic properties and defect density, *ibid.*, Vol. 38 p. 5768 (1999).
 - ²¹ U. K. Das, J. K. Rath, D. L. Williamson, and P. Chaudhuri, Correlation of Nanostructural Heterogeneity and Light Induced Degradation, *Jpn. J. Appl. Phys.*, Vol. 39, p. 2530 (2000).
 - ²² R. Baldner, H. Lautenschlager, C. Schetter, R. Schindler, W. Warta, Open circuit voltage losses in multicrystalline silicon: and investigation by mini solar cells, *25th IEEE Photovoltaic Specialists Conference*, Washington DC, p. 641 (1996).
 - ²³ I. Tarasov, S. Ostapenko, and J. P. Kalejs, Defect monitoring using scanning photoluminescence spectroscopy in multicrystalline silicon solar cell, *28th IEEE Photovoltaic Specialists Conference*, Alaska, p. 112 (2000).
 - ²⁴ B. Rezek, C. E. Nebel, and M. Stutzmann, Correlation of photoconductivity and structure of microcrystalline silicon thin films with submicron resolution, *Appl. Phys. Lett.* Vol. 75, p. 1742 (1999).
 - ²⁵ J. P. Boyeaux, A. Kaminski, N. Ferrer, S. Berger, and A. Laugier, Correlated light-beam induced current and infrared thermography mapping applied to the local characterization of large area multicrystalline solar cells, *28th IEEE Photovoltaic Specialists Conference*, Alaska, p. 319 (2000).
 - ²⁶ A. S. H. van der Heide, A. Schonecker, G. P. Wyers, W. C. Sinke, Mapping of contact resistance and locating shunts on solar cells using resistance analysis by mapping of potential (RAMP) techniques, *16th European Photovoltaic Solar Energy Conference*, Glasgow, 2000, p. 419.
 - ²⁷ O. Breitenstein, K. Iwig, and I. Konovalov, Evaluation of local electrical parameters of solar cells by dynamic (lock-in) thermography, *Phys. Stat. Sol. (a)*, Vol. 160, p. 271 (1997).

- ²⁸ I. E. Konovalov, O. Breitenstein, and K. Iwig, Local current-voltage curves measured thermally: a new technique of characterizing PV cells, *Solar Energy Materials and Solar Cells*, Vol. 48, p. 53 (1998).
- ²⁹ O. Breitenstein and M. Langenkamp, Quantitative local analysis of I-V characteristics of solar cells by thermal methods, 2nd World Conference on photovoltaic solar energy conversion, p. 1382, Vienna, Austria (1998).
- ³⁰ Kh. G. Naghmudinov and T. A. Polyanskaya, Current-voltage characteristics of Au/GaAs_{1-x}Sb_xGaAs in the light of fluctuation theory of thermal-field emission across Schottky barriers, *Sov. Phys. Semicond.*, Vol. 21, p. 1053 (1987).
- ³¹ L. E. Calvet, R. G. Wheeler, and M. A. Reed, Electron transport measurements of Schottky barrier inhomogeneities, *Appl. Phys. Lett.*, Vol. 80, p. 1761 (2002).
- ³² W. Monch, Barrier heights of real Schottky contacts explained by metal-induced gap states and lateral inhomogeneities, *J. Vac. Sci. Technol. V*, Vol. 17, p. 1867 (1999).
- ³³ A. A. Talin, R. S. Williams, B. A. Morgan, K. M. Ring, K. L. Kavanagh, Lateral variation in the Schottky barrier height of Au/PtSi/(100)Si diodes, *J. Vac. Sci. Technol., B*, Vol. 12, p. 2634 (1994).
- B. A. Morgan, K. M. Ring, K. L. Kavanagh, A. A. Talin, R. S. Williams, T. Yasuda, T. Yasui, Y. Segawa, Role of interface microstructure in rectifying metal/semiconductor contacts: ballistic electron emission observations correlated to microstructure, *J. Vac. Sci. Technol. B* Vol. 14, p. 1238 (1996).
- ³⁴ H. – J. Im, Y. Ding, J. P. Pelz, W. J. Choyke, Nanometer-scale test of the Tung model of Schottky-barrier height inhomogeneity, *Phys. Rev. B*, Vol. 64, p. 075310 (2001).
- ³⁵ R. T. Tung, Electron transport in inhomogeneous Schottky barriers, *Appl. Phys. Lett.* Vol. 58, p. 2821 (1992).
- ³⁶ M. E. Raikh and I. M. Ruzin, Transmittancy fluctuations in Randomly nonuniform barriers and incoherent mesoscopics, in: *Mesoscopic Phenomena in Solids*, Edited by B. L. Altshuller, P. A. Lee, and R. A. Webb, Elsevier (1991), p. 315.
- ³⁷ R. Tenne, V. Marcu, and N. Yellin, Evidence for nonuniform flow of charge carriers through semiconductor junction, *Appl. Phys. Lett.* Vol. 45, p. 1219 (1984).
- ³⁸ See papers in: *Modeling of film deposition for microelectronic applications*, Edited by S. Rossnagel and A. Ulman (Thin Films, Vol. 22), Academic Press, San Diego 1996.
- ³⁹ Mark Amman, Julie S. Lee, and Paul N. Luke, Electron trapping nonuniformity in high-pressure-Bridgman-grown CdZnTe, *J. Appl. Phys.*, Vol. 92, p. 3198 (2002).
- ⁴⁰ V. G. Karpov, Instability in the Classic Theory of Coarsening, *Phys. Rev. Lett.*, Vol. 74, p. 3185 (1995).
- ⁴¹ V. G. Karpov, G. Rich, A. V. Subashiev, and G. Dorer, Shunt screening and size dependent effects in thin-film photovoltaics, *J. Appl. Phys.*, Vol. 89, p. 4975 (2001).
- ⁴² G. Lukovsky, Photoeffect in nonuniformly irradiated p-n junctions, Vol. 31, p. 1088 (1960).
- ⁴³ R. H. Bube, *Photovoltaic Materials*, Imperial College Press, London 1998.
- ⁴⁴ V. G. Karpov, G. Rich, A. V. Subashiev, G. Dorer, *J. Appl. Phys.* 89, p. 4975 (2001).
- ⁴⁵ The computer program was written by Yu. Sosov (UT).
- ⁴⁶ V. G. Karpov, R. Harju, and G. Dorer, *Proc. 27th IEEE Photovoltaic Specialists Conference*, Alaska, p. 547 (2000); V. G. Karpov, A. D. Compaan and Diana Shvydka, *Appl. Phys. Lett.* **80**, p. 4256 (2002); V. G. Karpov, A. D. Compaan and Diana Shvydka, To be published in the 29th IEEE PVSC.

4. Characterization of materials and devices

4.1 Photo- and electro-luminescence studies

During the past year we have continued a variety of luminescence studies--including both photo-luminescence and electro-luminescence. For the review of the photoluminescence, we discuss separately 1) PL mapping carried out as part of the "Nonuniformity" subteam of the National CdTe Team, 2) PL decay (fatigue) measurements, 3) PL studies of ion-implanted samples, and 4) PL studies as part of the "Defect Chemistry/Materials Chemistry" subteam. Finally, 5) we discuss electroluminescence measurements at low drive levels and variable temperature.

4.1.1 Photoluminescence (PL) mapping

Our effort in studying the effects of nonuniformities included the National CdTe Team Meetings in Florida (March 2002) and in Golden (November 2002), where we coordinated projects in the "Micrononuniformity" topical sub-team. The sub-team presented results on PL-mapping, μ -EL, μ -PL, μ -LBIC, GIXRD, AFM, EBIC, CL.

PL mapping was aimed at characterizing the degree of device lateral uniformity in fresh and degraded samples with and without metal contacts. Room temperature PL was excited by a 752 nm laser with the beam spot size of $\sim 80 \mu\text{m}$ and step size $200 \mu\text{m}$ in line scanning. We used two laser intensities: ~ 2000 sun and ~ 200 sun. Both the changes in PL spectra and total PL intensity integrated from 1.38 to 1.62 eV were measured.

It was observed (Fig. 4.1.1) that the PL peak shifts to higher energy under the contact and, generally, the PL intensity is higher from the contact-free area, (first observed in Ref. [1]). While the latter observation was typical, some unusual samples were also found where applying metal did not have a noticeable effect on the PL intensity. Considerable ($\sim 80\%$) correlation was found between the maps corresponding to the two different excitation powers.

Light soaking typically increased the ratio of PL intensities between the contact and metal-free areas, leaving other features practically intact (Fig. 4.1.2b).

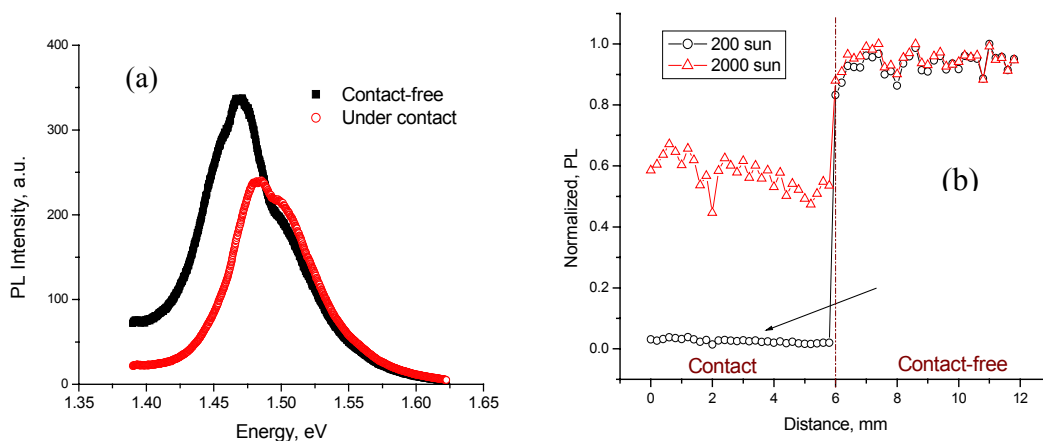


Fig. 4.1.1. Typical PL spectra (a) and integrated PL intensities (b) under the contact and in contact-free areas for VTD samples. Integrated PL intensities are shown for two different excitation powers in a fresh sample and are normalized to the maximum PL.

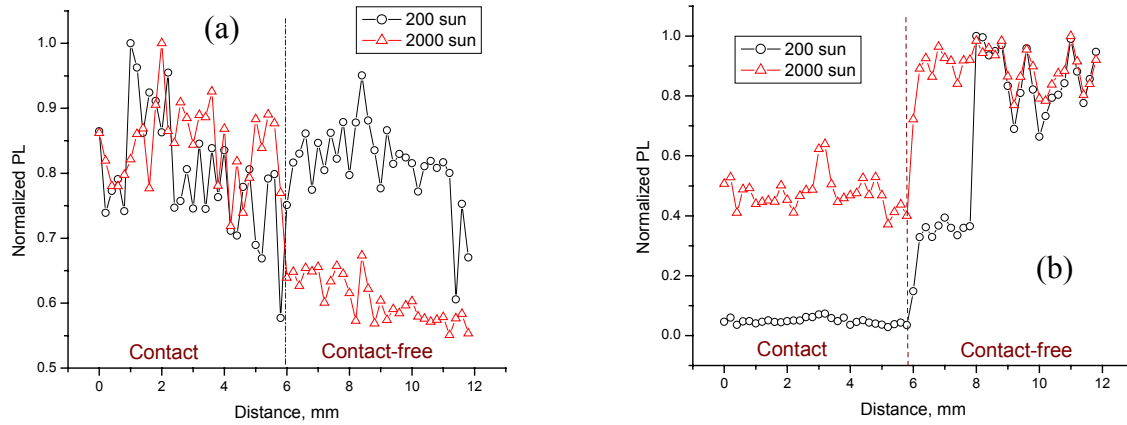


Fig. 4.1.2. PL scan of “unusual” VTD fresh sample (a) and typical 28-day light soaked VTD sample (b) for two excitation powers. Note suppressed zero in (a).

Our interpretation of the PL ratio between under-contact and contact-free areas is close to that of Levi, et al [1] and is illustrated in Fig. 4.1.3. The explanation assumes shunting pathways, whose influence extends greatly as the contact metal is applied, which turns the device into a short circuit (SC) regime. Without the metal the junction at the laser spot is largely under open-circuit (OC) conditions, making the nonequilibrium electrons and holes accumulate, which suppresses the built-in electric field. Because the weaker field is less efficient in spatially separating the electrons and holes, they recombine more readily, thus increasing the PL intensity.

An observation seemingly inconsistent with the above explanation was that the measured I/V curves did not exhibit characteristic shunting features. We therefore assume that shunting is due to weak micro-diodes^{2,3} rather than to the standard ohmic shunts.

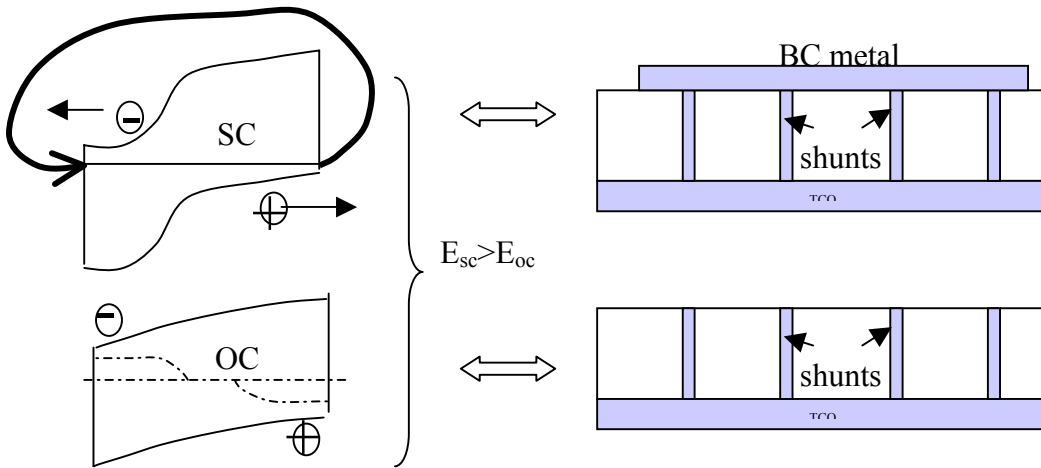


Fig. 4.1.3. Built-in electric field suppression by back-contact (BC) metal in a device with shunting pathways. The left side shows p-n junction band diagrams under short-circuit and open-circuit conditions. The right side illustrates short circuiting by a combination of shunting pathways and back-contact metal.

For the magnetron-sputtered samples the shift in the spectrum, under or away from the contact, was analogous to that of VTD samples (Fig. 4.1.1a), while the PL maps turned out to be somewhat different as is illustrated in Fig. 4.1.4. In interpreting the difference we take into account that in magnetron-sputtered samples the PL variations are due to a combination of two effects: (i) the presence of the metal contact and (ii) local Cu doping under the contact, as opposed to the VTD samples where both contact and contact-free areas are doped equally. Assuming Cu doping to increase PL efficiency, and the application of metal to do the opposite, the PL under the contact in magnetron-sputtered samples will be affected by the above opposing factors. This may result in the contact-free area PL intensity to be less than under the contact. One indirect confirmation for the above interpretation follows from the ‘rabbit-ear’ feature at the contact edge in Fig. 4.1.4, which can be interpreted as the positive effect of Cu doping (diffused slightly beyond the contact) in the absence of the negative effect of the contact metal.

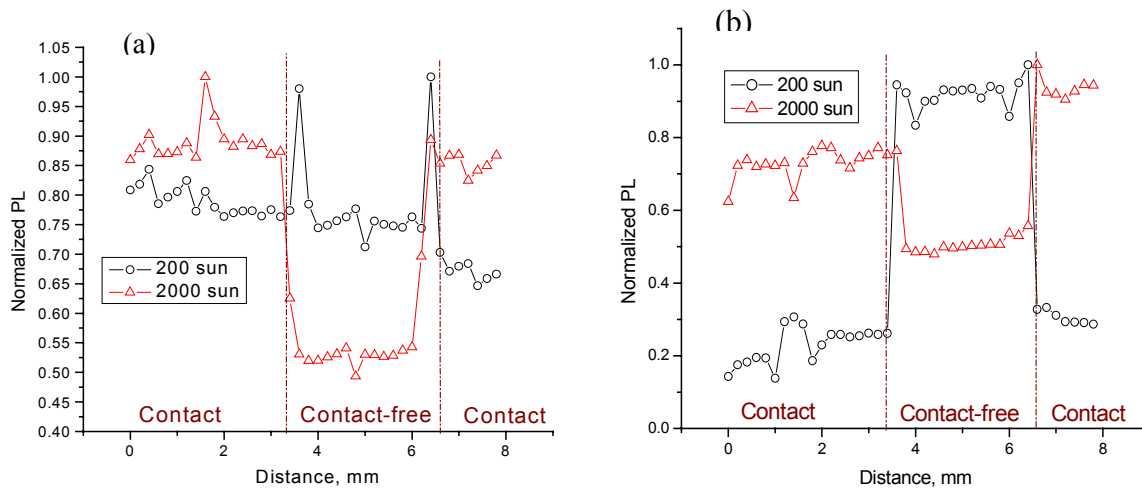


Fig. 4.1.4. PL mapping of magnetron-sputtered samples before (a) and after (b) 28-day light soak for two excitation powers.

In order to confirm the positive effect of Cu doping on the PL efficiency from CdTe, we deposited a thin layer of Cu on a piece of CdTe *single crystal* and diffused this sample for 30 min at 150 °C, following our standard Cu-Au contact diffusion procedure. We measured the PL signal *through the metal layer* before and after Cu diffusion and indeed observed an increase in the PL intensity after the diffusion (Fig. 4.1.5). Similar measurements on a metal-free area of the crystal showed no change in PL signal.

Shown in Fig.4.1.6 are typical PL maps of fresh and stressed samples. We observe that the PL intensity in the Cu-free area is not very sensitive to degradation. (These samples were prepared with the UT Cu-Au evaporation process and did not have a uniform Cu layer across the sample.) To the contrary, the PL intensity under the contact decreased considerably after light soak. However, as part of our team activity we studied cells fabricated at CSU (Colorado State). The CSU material with the CSU contacts shows the opposite trend to that of FS and UT material, namely that the PL intensity increases after light soak. One important observation is that the light soak increases the degree of non-uniformity, as is illustrated more quantitatively in Fig. 4.1.7 where we show the relative standard deviation (SD) of each scan line of about 250 points. For sputtered cells the SD rises from about 0.5 before, to 0.65 after 28 day light soak stress for PL

under the contact. The change in the SD is greater for the FS cell—from about 0.3 to 0.7 after stress. Note that scan lines near #6 are entirely under the contact. Scan lines near #17, for the FS, and #13 for the UT cell are entirely outside the contact. But for these circular contacts, intermediate scan lines are partly under and partly outside the contact area.

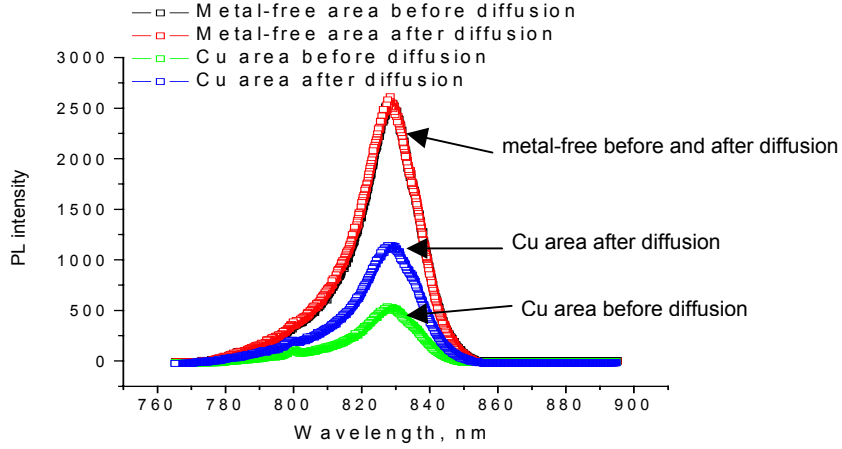


Fig.4.1.5. Comparison of PL spectra measured on CdTe single crystal before and after Cu diffusion. Signal from the metal-free area (largest peak) shows no change after diffusion.

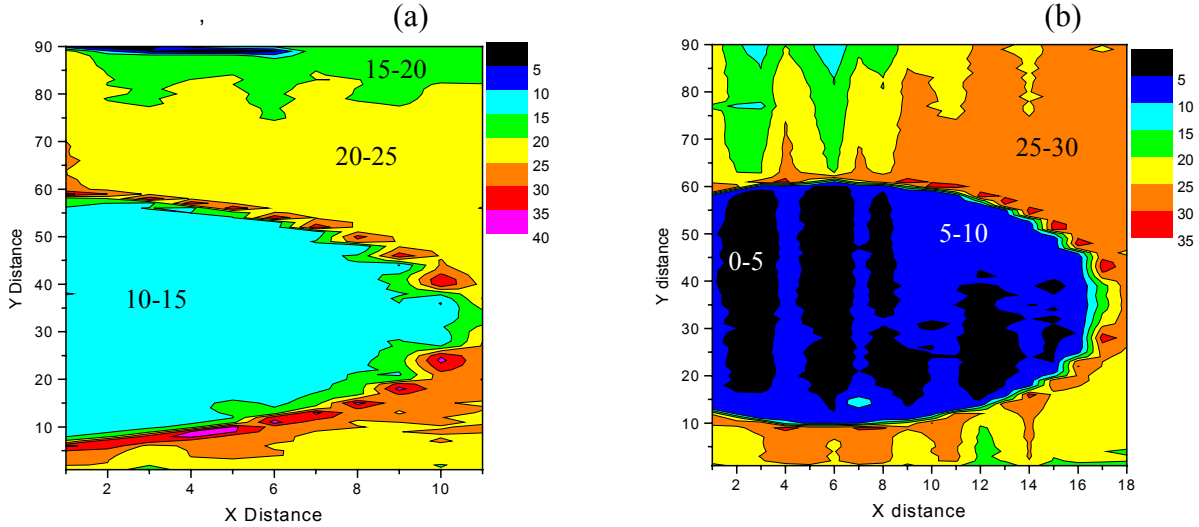


Fig.4.1.6. PL maps of two VTD cells with UT Cu-Au contact before (a) and after (b) light soak stress.

Our conclusions on PL mapping can be summarized as follows:

- (i) PL mapping shows significant nonuniformities in both VTD and rf-sputtered as well as in fresh and stressed devices.
- (ii) The PL map topology generally depends on excitation power.
- (iii) There are substantial differences in PL intensities, spectra, and topologies between the contacted and contact-free areas.

- (iv) The ratio of PL intensities from the contacted and contact-free areas varies between samples.
- (v) There is no significant difference in PL spectra and degree of PL nonuniformity between fresh and stressed samples for the contact-free area. However, such difference was observed for PL intensity from under the contacted areas.
- (vi) Nonuniformities of different scales can be observed.

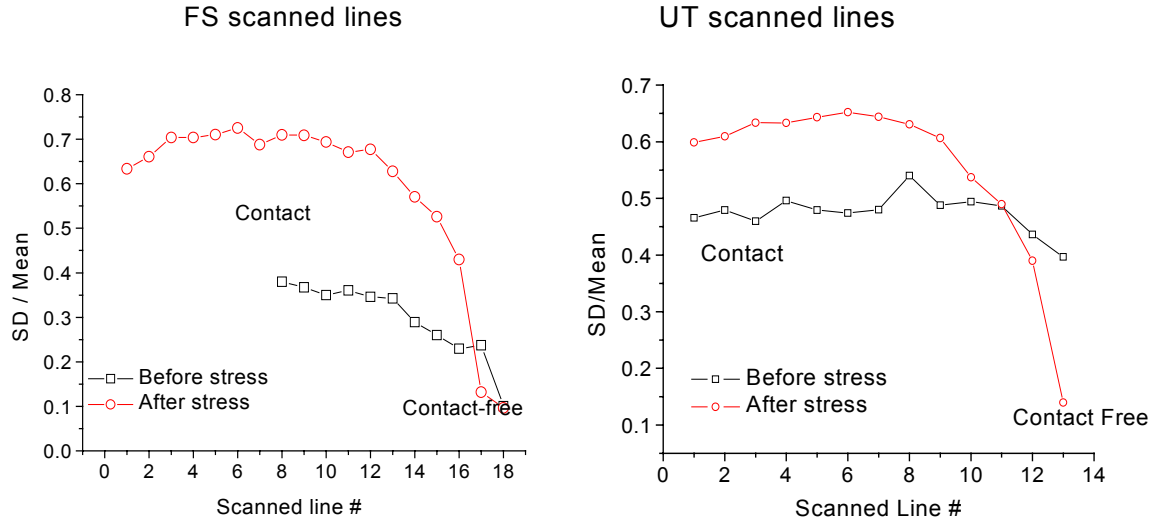


Fig.4.1.7. Relative Standard Deviation (SD) for each scan line as a measure of nonuniformity: each datum point represents the relative SD for one scan (about 15 mm and ~250 points). Relative SD is measured on both stressed and unstressed devices.

We plan to further extend the PL mapping technique capabilities by (1) studying it under applied bias, and (2) by developing a more quantitative interpretation.

4.1.2 PL intensity degradation (fatigue) measurements

In this section we describe our preliminary results on PL intensity degradation under steady-state laser excitation. We believe that studying this phenomenon will improve our understanding of the light-induced degradation mechanisms in solar cells and can potentially be used as an accelerated life-testing tool.

A decrease in photoluminescence intensity under constant laser beam illumination was reported in the literature for several different systems, such as chalcogenide glasses,⁴ porous⁵ and a-Si,⁶ GaAs crystals,^{7,8} etc. It is also referred to as PL decay or PL fatigue. In each case an explanation of this decay was related to particularities of the material studied. We have observed the same phenomenon in CdTe solar cells under Kr laser (752 nm) illumination and studied the temperature and laser intensity dependence of the decay rate. Extending our bias-dependent PL model,⁹ we interpret our data in terms of defects created by light-generated charge carriers.

Typical normalized decay curves for three different temperatures are shown in Fig.4.1.8 for high (a) and low (b) laser intensities. We were able to discriminate between two independent mechanisms: short-time PL decrease due to local laser heating and more gradual change related to the material degradation (PL fatigue). PL fatigue was more profound at higher temperatures and higher laser beam powers. Its observed value in some cases was as large as 80 percent in two hours. However at low temperatures and low beam powers it saturated rather quickly, not exceeding 10 percent of the initial PL intensity. PL fatigue showed substantial variations between different spots on the sample.

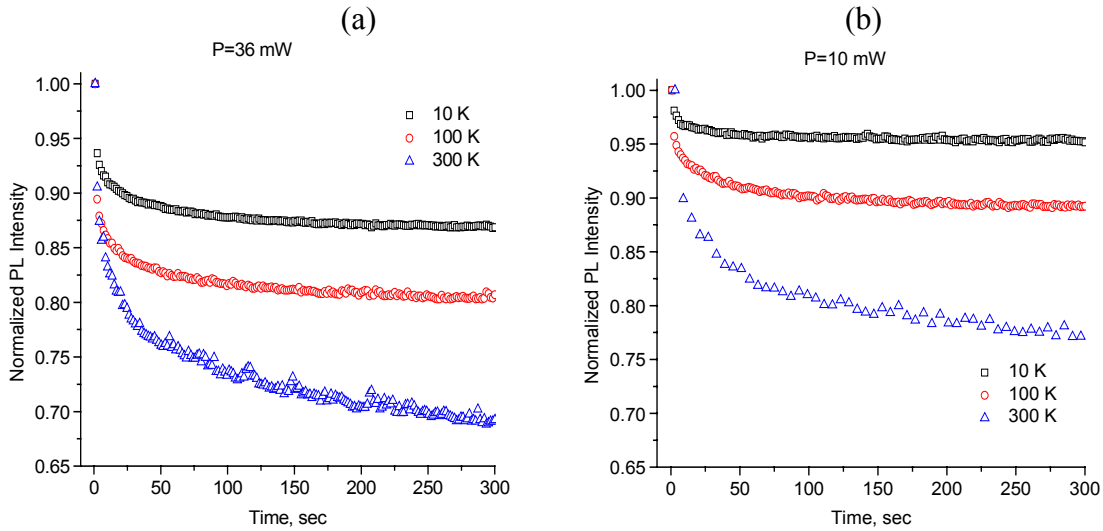
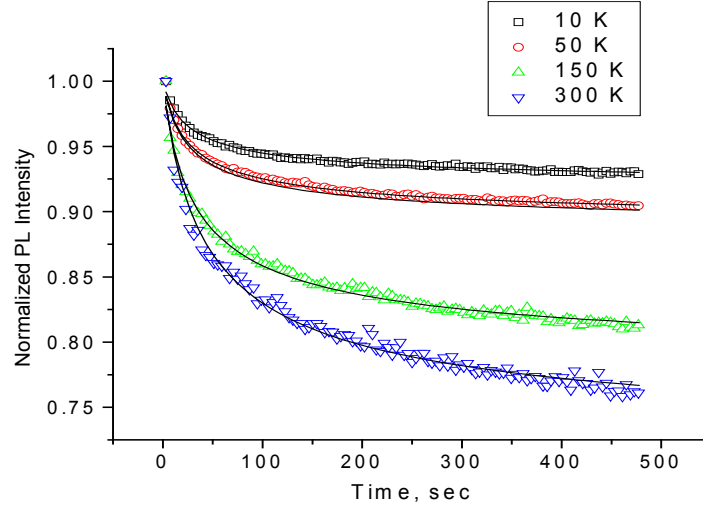


Fig.4.1.8 Typical PL decay data from under-contact area for three different temperatures and two laser powers (a) 36 mW; (b) 10 mW.

Shown in Fig.4.1.8 are typical data corrected for the effect of heating. These curves represent the true PL fatigue. Our interpretation of the observed decay is that the laser-generated electrons and holes create defects. As was shown in our paper on bias-dependent PL,⁹ when the defect concentration is high enough they dominate the PL intensity. That is why, in the course of illumination, the PL shows fatigue as defect-assisted nonradiative recombination increases.

Fig.4.1.9. Normalized PL fatigue in a CdTe solar cell for four different temperatures corrected for the effect of heating. Solid lines represent fits by Eq. (1).

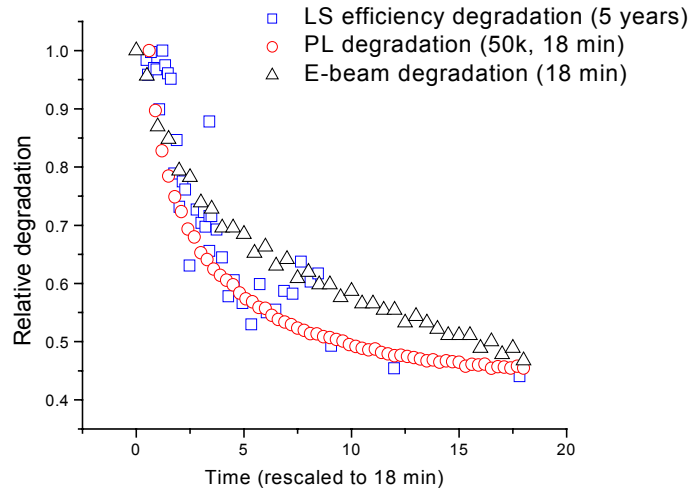


Following the approach in [Ref. ¹⁰] we derived the normalized PL intensity vs. time in the form:

$$I = \left(1 + A \left(\left(1 + \frac{t}{\tau} \right)^{-0.5} - 1 \right) \right)^2, \quad (1)$$

where A is a fitting parameter and τ is the characteristic decay time that depends on excitation power and temperature. Eq.(1) implies PL intensity quadratic in the carrier concentration. The latter decays with time due to defect accumulation and corresponding decrease in the lifetime. The fits shown in Fig.4.1.9 following Eq. (1) are in satisfactory agreement with the data.

Fig. 4.1.10. Normalized relative degradation data for PL intensity, EBIC and solar cell efficiency under light soak. Light soak data are rescaled to the time interval of PL intensity decay.



The above hypothesis of the electron and hole generated defects is, in fact, very general. That is why one can expect the same mechanism to underlie degradation in other physical quantities, such as cell I/V parameters, EBIC, etc. The latter suggestion is verified in Fig. 4.1.10, where we have compared the degradation in seemingly different parameters: PL fatigue from the present work, EBIC ¹⁰ and cell efficiency under light soak ¹¹. We observe that as properly scaled all three quantities degrade with time in similar fashion. This allows us to generalize our model to all mentioned phenomena. From a practical standpoint, PL decay in CdTe photovoltaics then becomes a promising candidate for a nondestructive accelerated life testing tool.

4.1.3 Ion implantation and PL studies of CdTe

Photoluminescence and electroluminescence are convenient and powerful methods to probe the material properties of an operating solar cell and to investigate the defect states in the active semiconductor material. PL and EL are particularly convenient for studies of the junction region. However, the unambiguous identification of the transitions responsible for the light emission, particularly in polycrystalline thin films has been elusive. Partly to address this difficulty of identification, we have started a series of measurements on single crystals and thin films which have received calibrated doses of known atoms from ion implantation. The disadvantage of ion implantation is that large numbers of defects are created for each atom implanted, typically 1000 displacements for each implant. In our Final Report from the previous award,¹² we showed, by studies on Te-implanted CdTe, that a 30-minute anneal at 400 °C in N₂ atmosphere, using a CdTe film as a proximity cap, allowed the implantation-induced damage to be removed. Fig. 4.1.11 is taken from that report and shows the 10K PL spectra taken after implantation with a $1.25 \times 10^{13} \text{ cm}^{-2}$ dose of Te ions at an energy of 880 keV. PL data were taken with excitation at 488 nm to match the projected range of the implant and damage. The as-implanted sample shows no PL; the successive anneals at 375, 400, and 425 °C show an increasing PL peak at 1.538 eV with a phonon replica at 1.518 eV. A deep-center band in the region from 1.42-1.47 eV reaches a maximum after the 400 °C anneal. As discussed in our Final Report, the PL from the virgin crystal showed a strong peak at 1.547 eV with a replica at 1.526 eV. This suggests that after the Te implant and anneal the 1.538 eV peak arises from a Cd-vacancy defect. Whether this peak is due to an exciton bound to this defect or from a donor-acceptor pair in which the Cd-vacancy serves as the acceptor, is not yet clear.

The ion-implant-doped studies continued during the present year but were slowed due to some equipment problems. However, a study of Cu implants was accomplished. The ion

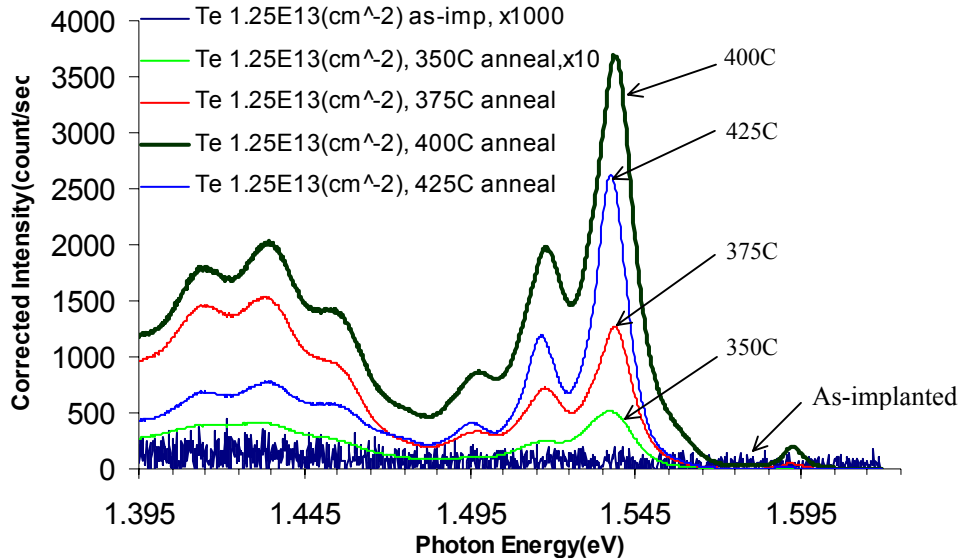


Fig. 4.1.11. PL obtained with 1.2 mW at 488 nm from crystalline CdTe and from regions implanted with 880 keV Te⁴⁺ to 10^{13} ions/cm² and annealed successively at 350, 375, 400 and 425 °C. For visibility, data have been multiplied by 1000 and 10 for the lowest traces.

implantation is done through collaboration with the atomic physics group at the University of Toledo on the accelerator in the Physics and Astronomy Department. The Cu^{++} ions were implanted into crystalline CdTe at 3 different energies: 440, 220 and 100 keV to obtain total doses of 2.8×10^{11} , 2.8×10^{12} and $2.8 \times 10^{13}/\text{cm}^2$. The project range and range straggling are, respectively, 0.1784 and 0.099 μm from Monte Carlo calculations using “SRIM”--- The Stopping and Range of Ions in Matter).¹³ These energies were chosen, again, to match the absorption length of the 488nm PL excitation laser. Annealing at 400°C in N_2 was done to remove most of the vacancies and interstitials produced by the implanted ions.

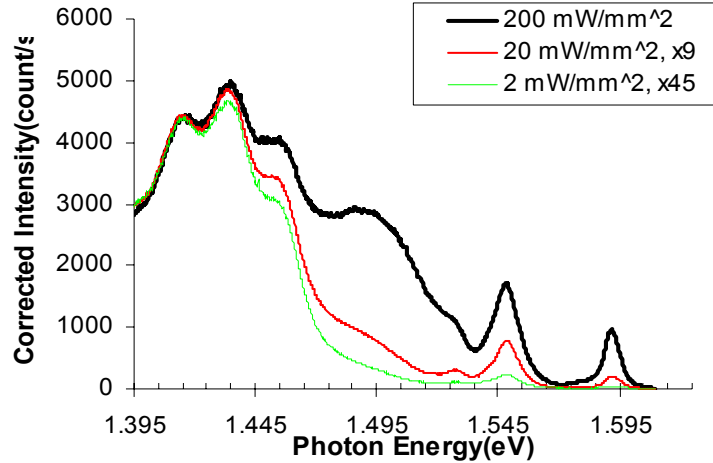


Figure 4.1.12 10 K power-dependent PL on $2 \times 10^{13} \text{ cm}^{-2}$ a Cu-implanted sample. The broad peak at 1.49 eV shifts to higher energy with laser power.

PL from the implanted and annealed crystalline CdTe was studied at excitation power densities of approximately 2, 20 and 200 mW/mm^2 (~ 2 , 20, and 200 suns) to help identify the origin of the various features. For example, the bound exciton peak near 1.593 increases superlinearly with laser intensity whereas the deep donor-acceptor pair transitions near 1.44 eV are sublinear in excitation intensity. This Cu-implanted crystal has a new peak at $\sim 1.49 \text{ eV}$ which shows a characteristic shift toward higher photon energies with increasing excitation intensity. This helps to identify this peak as arising from a spatial distribution of donor-acceptor pairs. (See discussion in Section 4.1.4 below.) We suggest that this peak arises from a Cu acceptor substitutional on a Cd site together with an as yet unknown donor. Further discussion is provided in the next section.

This effort on ion-implanted CdTe crystals and films is continuing with the implantation of other atomic species, particularly those anticipated to be important as acceptors and donors in CdTe cells.¹⁴

4.1.4 Defect chemistry studies

As a part of the National CdTe team we participated in the Defect/Materials Chemistry sub-team activity. Our task was to perform low-temperature PL measurements on VTD cells which had been light soaked under different bias conditions and to try to identify defects formed during the stress. The sub-team leader – First Solar, provided these samples. We presented the initial results of our study during the CdTe teaming meeting in Golden (November, 2002).

The PL signal was excited from the solar-cell junction with the 752 nm (1.6488 eV) line of a Kr laser focused to a ~ 200 μm diameter spot. The spectrum was detected in the below-band-gap range from 1.38 eV to 1.62 eV at 10K. The first set of samples we studied consisted of 6 samples stressed at 1 sun illumination for 77 days at ~ 60 $^{\circ}\text{C}$ under the following bias conditions: -2V, -1V, -0.5V, short circuit (SC), open circuit (OC) and resistive load (RL). We also included a reference sample (unstressed but from a different batch) for comparison. We found that all samples stressed under reverse bias and SC produced very similar spectra, while OC and RL spectra were a little different. Typical PL spectra are shown in Fig. 4.1.13.

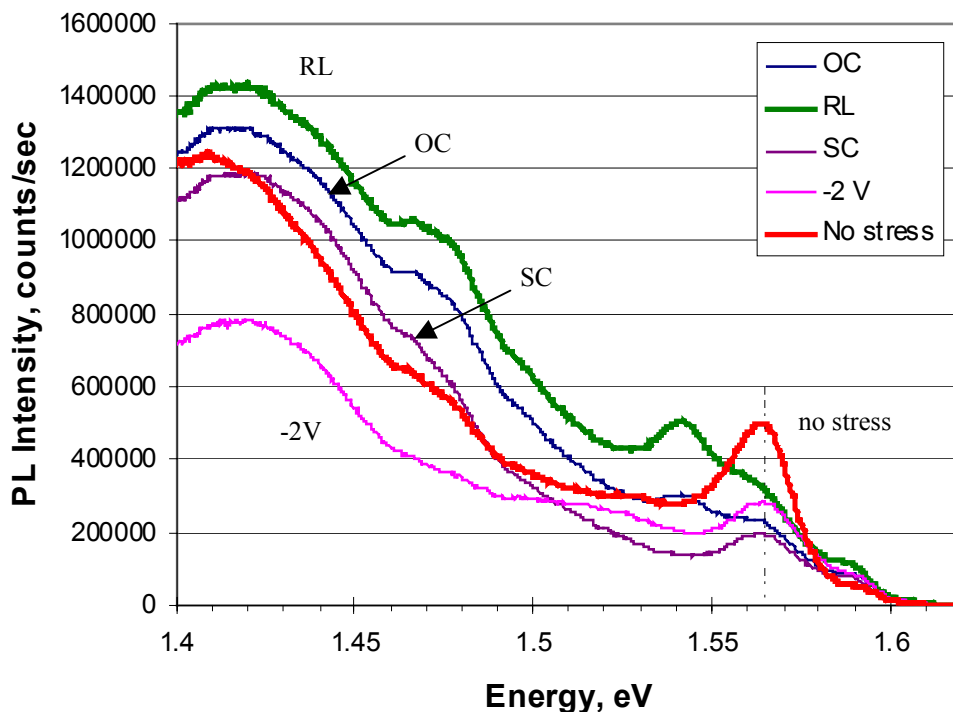


Fig.4.1.13. Low-temperature junction PL spectra for the first set of samples stressed at 60 $^{\circ}\text{C}$ under four different bias conditions for 77 days followed by 30 days of recovery in ambient light and room temperature. Laser intensity ~ 100 mW/mm^2 .

All cells show a bound exciton peak at ~ 1.59 eV, a peak at about 1.563 eV (possibly a more deeply bound exciton), and a broad band from 1.4 to 1.47 eV probably related to a deep donor-acceptor pair. The cells stressed at open circuit and resistive load exhibit a peak at ~ 1.54 eV. The unstressed cell and that stressed at -2V show evidence of a broad peak near 1.52 eV.

For the second round of measurements we received a set of three samples: a reference sample, and two samples light-soaked at $-2V$ and OC bias conditions at one sun for six days. We observed a prominent peak at 1.52 eV in the sample stressed at $-2V$ for 6 days (see Fig.4.1.14). Power-dependence analysis of this peak allowed us to identify it as donor-acceptor pair recombination feature. (It shifts to higher photon energy as the excitation power is increased.) Note, however, that for 77 days of stress, this peak is not observed.

In order to identify different features in the PL spectra we did our measurements at different laser powers in a range from 0.4 to 12 mW (corresponding to power densities from about 10 sun to 300 suns). These results are shown as Fig. 4.1.14 in a panel of three figures for the unstressed, light-soaked-at-open-circuit, and light-soaked-at- $2V$ -negative-bias cells. For the light-soaked samples, the measurements were performed within one day after removal from the light-soak station. The highest power data (12 mW) show evidence of sample heating with a red-shift of the features by about 3.5 meV.

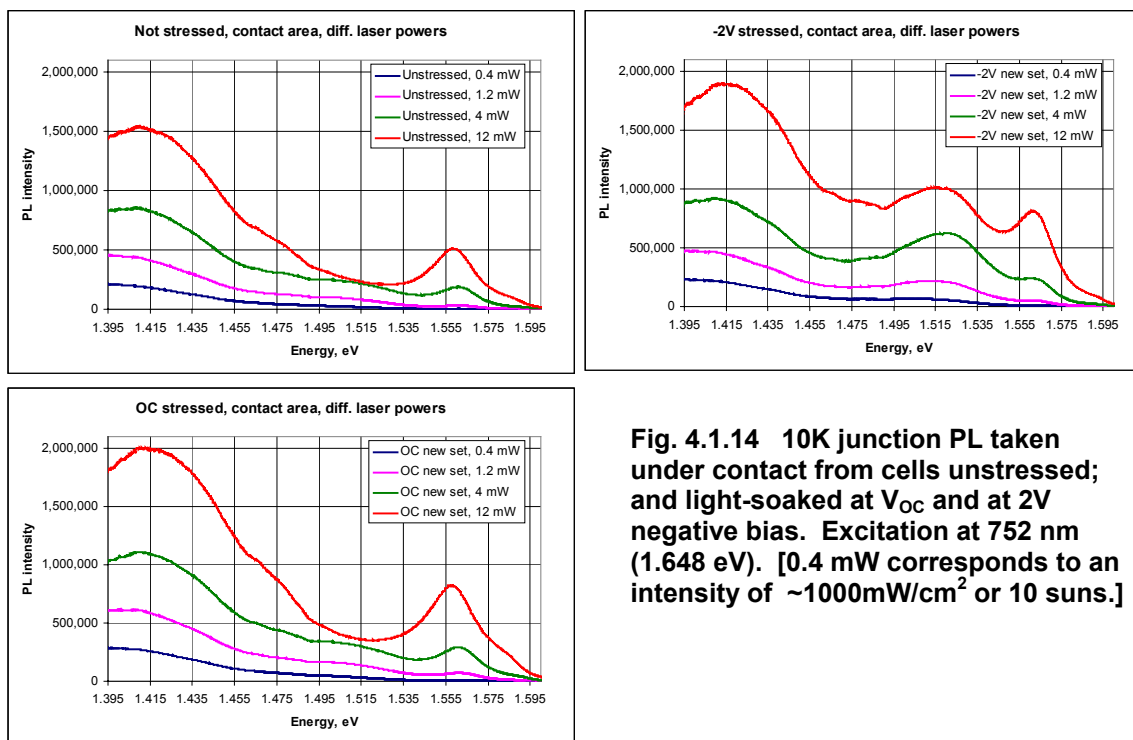


Fig. 4.1.14 10K junction PL taken under contact from cells unstressed; and light-soaked at V_{OC} and at $2V$ negative bias. Excitation at 752 nm (1.648 eV). [0.4 mW corresponds to an intensity of $\sim 1000 \text{ mW/cm}^2$ or 10 suns.]

For this second round we also studied the sample recovery behavior. Shown in Fig. 4.1.15 is the spectrum from the same sample after 5 days of recovery in the dark at V_{OC} and room temperature. The significant change in the “recovered” spectrum demonstrates that defect states created during stress may have very short lifetimes. The sample stressed under V_{OC} did not show any significant recovery in 5 days.

Since all defect peaks in the PL spectra of polycrystalline CdTe are broad and prone to change a little from sample to sample and with time, one has to be very careful about their identification. (We plan to do additional PL measurements on samples from different deposition batches, stressed at different bias conditions.) However, we suggest that this peak observed at 1.52 eV (lower energies at lower powers) from the junction in the polycrystalline films is consistent with the peak seen at 1.49 eV in the single crystal, ion implanted with copper (See Fig. 4.1.12.)

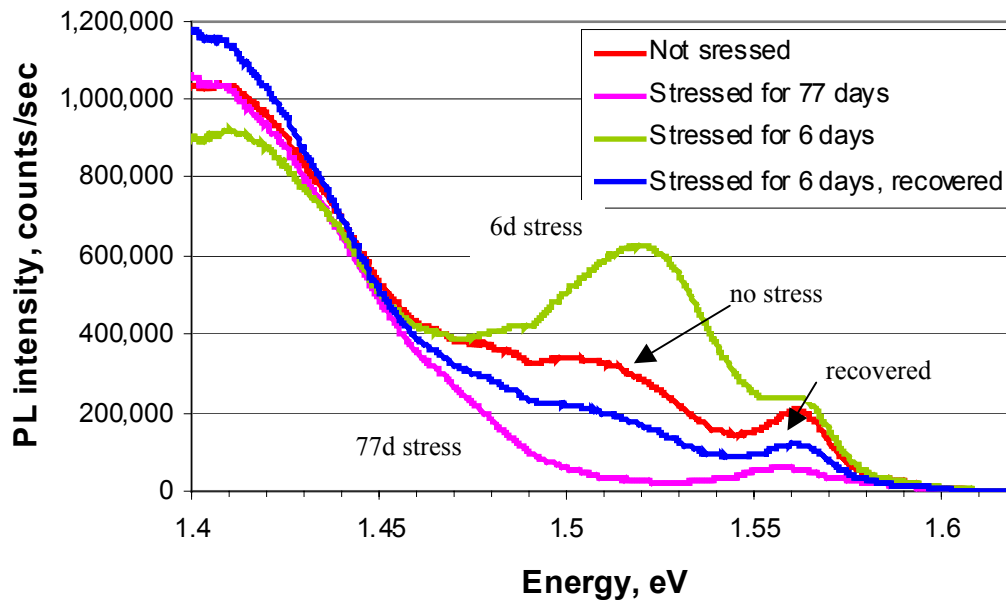


Fig.4.1.15. 10K junction PL spectra for the sample stressed under -2V bias conditions for 6 days, measured immediately after stress and after 5 days of recovery. Spectrum for sample stressed for 77 days included for comparison. Excitation at ~100 suns equivalent.

Discussion--The identification of the particular defect states (e.g., donor and acceptor levels) based on photoluminescence transitions requires considerable care for several reasons.¹⁵ First, although the exciton energy in CdTe is well-known ($E_g - E_b = 20$ meV), in most situations at low temperature, bound-exciton transitions dominate the free exciton transitions since the energy is lowered by an additional binding to the defect. Thus the neutral-donor-bound exciton or neutral-acceptor-bound excitons will have an additional binding energy of 50 to 100 meV or so, depending on the defect specie.

The donor-acceptor pair transitions are complicated by the fact that there is a large coulomb interaction in the final state which adds energy to the emitted photon. This process is sketched in Fig. 4.1.16. Thus, photo-excitation provides abundant free electrons and holes which neutralize the donors (D^0) and acceptors (A^0). Among these will be relatively near-neighbor pairs ($D^0 - A^0$). If their separation is close enough to provide some overlap of the electron and hole wavefunctions on the two separated centers, electron-hole annihilation will occur leaving the ionized pair ($D^+ - A^-$) with its strong coulomb interaction which will contribute energy to the outgoing photon. This coulomb interaction will be inversely proportional to the D-A pair separation. (For typical separations equal to the sum of donor and acceptor radii, this coulomb energy will be about 50 meV.)

Furthermore, the transition probability will increase with increasing wavefunction overlap (decreasing separation) even as the final state interaction energy increases (negatively) so that the nearest neighbor pairs will have the highest transition rate and yield recombination photons of the highest energy. Thus, relatively distant pairs, with lowest energy recombination transitions, will be most abundant (since the probability of their occurrence increases like the square of their separation) and will dominate the PL spectrum at low excitation powers. However, because their recombination rate is small, these transitions saturate as the excitation power increases and the nearer-neighbor pairs will dominate the spectrum at higher excitation

powers. Thus, a key signature of D-A pair transitions is that the band shifts to higher energy as the excitation power increases.¹⁶ The spectra at four different powers seen in Fig. 4.1.14 show this behavior for both the 1.4-1.46 eV band and the 1.49-1.53 eV band. We take this behavior as evidence of the D-A pair nature of the transitions. By contrast, the bound exciton lines at 1.59 eV and 1.56 eV do not shift with excitation power.

The dependence of the PL line *intensities* on the excitation power also provide signatures of the different types of recombination transitions. When the photogenerated electron and hole densities both exceed the majority carrier density, the free exciton and the bound exciton lines should increase super-linearly with excitation power (with exponent between 1 and 2). By contrast, the D-A pair transitions and other defect transitions will increase sublinearly with power as the finite number of pairs and defects is fully utilized in recombination transitions. This power dependence is clearly evidence also in Fig. 4.1.14 as the bound-exciton lines at 1.56 and 1.59 eV become relatively stronger compared especially with the D-A pair band at 1.4 – 1.47 eV.

If we take the transition energy of what appears to be a Cu-related defect at 1.49 eV seen in the Cu-implanted single crystal CdTe (Fig. 4.1.12), and assume the final state coulomb energy to be 50 meV, then the neutral donor-acceptor pair energy would be 1.54 eV. It is generally accepted that the donor states in CdTe will be “effective-mass-like,” due to the low effective mass in the conduction band, so that the donor binding energy can be estimated as ~20 meV. With a band gap of 1.600 eV at 10K, this would place the acceptor energy for this Cu-related D-A transition at an energy of $1.600 - 1.540 - 0.020 = 0.040$ eV = 40 meV. This conflicts with the calculated value of $E_v + 220$ meV of the substitutional Cu_{Cd} acceptor calculated by Wei and Zhang.¹⁴ In the extensive work of Molva, *et al*,¹⁷ the $1S_{3/2}$ ground state of the Cu_{Cd} acceptor is identified at $E_v + 146$ meV and the $2S_{3/2}$ excited state is identified at $E_v + 21.6$ meV. Thus it is possible that this Cu-related transition involves an excited state of the acceptor. However, it is also quite possible that this defect state involves not only a Cu defect but also a Cl defect. Further work is in progress with both CdTe crystals and polycrystalline thin films.

Donor-acceptor pair transitions in CdTe:

For radiative e-h annihilation, the transition is $D^0 A^0 \rightarrow D^+ A^-$

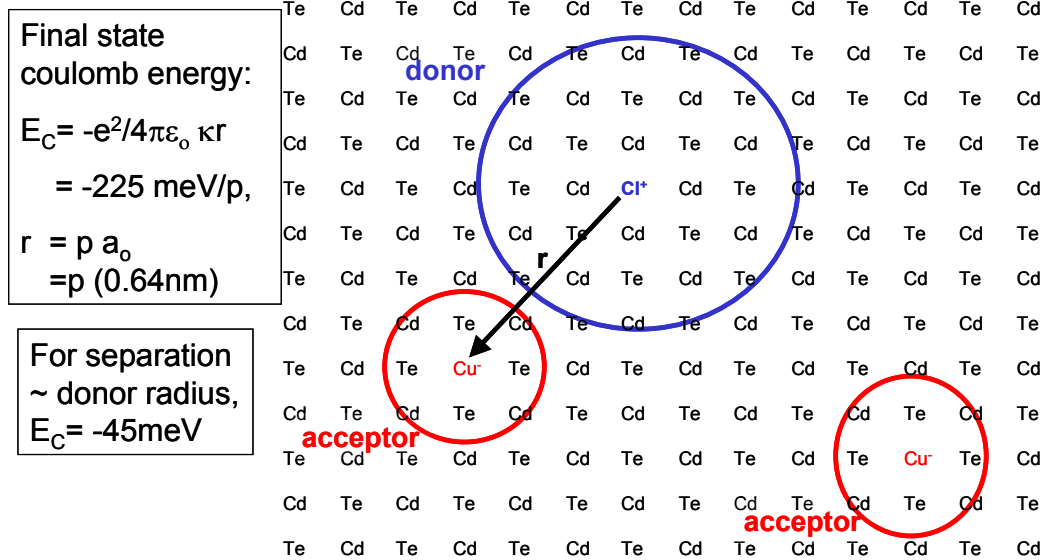


Fig. 4.1.16 Sketch of a donor-acceptor pair in CdTe with radii approximating effective-mass values in CdTe.

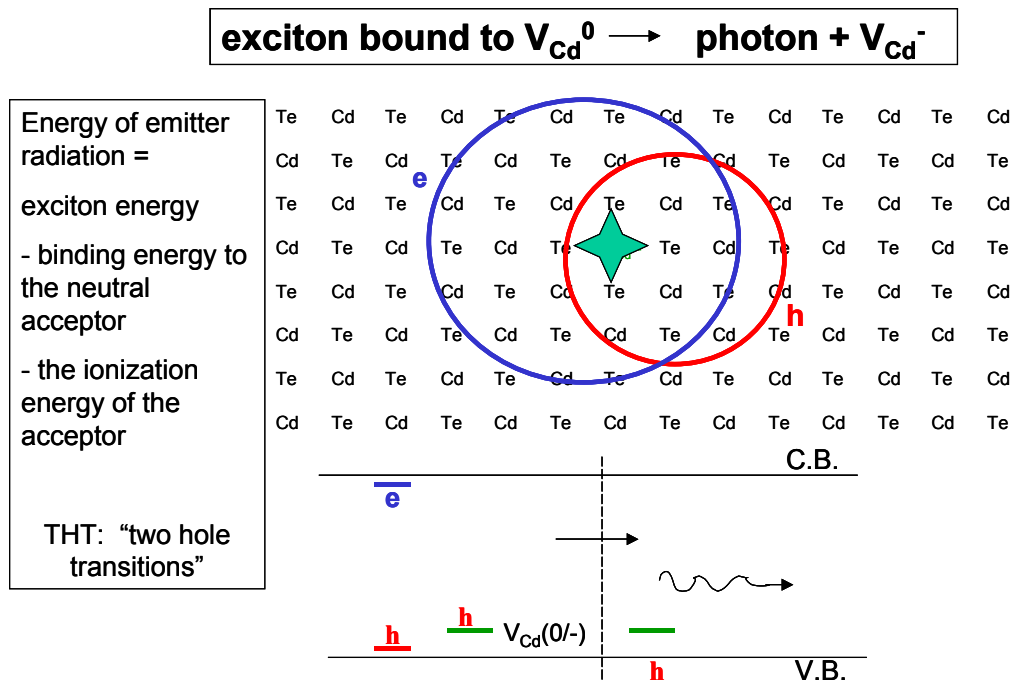


Fig. 4.1.17 Sketch of a two-hole transition in which a D-A pair, together with a nearby acceptor can yield a photon energy reduced by the ionization energy of the hole.

4.1.5 Electroluminescence at low drive levels and low temperature

Our studies of electroluminescence (EL) from CdTe/CdS solar cells were started in the summer of 2001 and some results have been reported earlier.¹⁸ We have shown that the EL spectrum at room temperature is very similar to the PL spectrum and does not change shape with changing applied voltage. Figure 4.1.18 compares the EL from a standard sputtered UT Cu/Au contacted CdTe/CdS cell with PL from the same device. The PL was excited with 4 mW of 752 nm light from a Kr laser focused to a ~0.5 mm spot at the CdS/CdTe junction through the glass/TCO/CdS. The 752 nm light penetration depth is ~0.3 μm in CdTe. The EL, observed through the glass superstrate, was excited by a forward bias voltage of 2 V resulting in a current of 12 mA/cm² over a 0.15 cm² contact dot. The similarity of the two spectra indicate that the EL results from electron-hole recombination in CdTe near the CdTe/CdS junction. A rough calculation taking into account relative collection efficiency of the PL and EL emission indicates that the relative power efficiencies of the EL and PL are approximately the same. The relative PL power efficiency at the spectral peak is ~7000 counts/mW of incident light power, while the EL efficiency at 1.4 V applied bias is ~10,000 counts/mW of electrical power. (The collection optics for the EL imaged less than a 0.5 mm x 4 mm slice of the 0.15 cm² contact or about 13% of the contact area. The EL in Fig. 4.1.18 was multiplied by 20 before plotting.)

The initial EL study also found that the EL intensity varied as a power-law function of current:

$$I_{EL} = a J^b, \quad (1)$$

where I_{EL} is the EL intensity, J is the current density, and a and b are constants. The exponent b was found to vary from sample to sample and to have a value between 1 and 3.

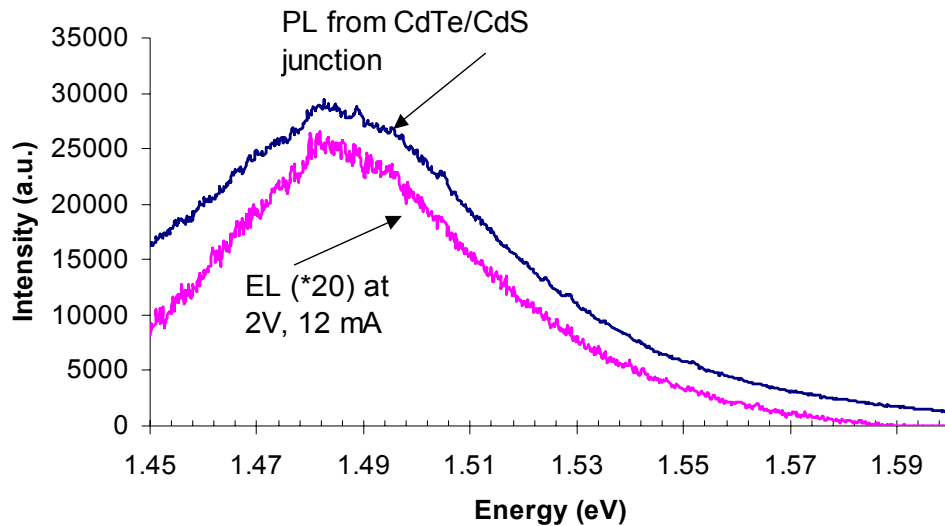


Figure 4.1.18: Room temperature EL and PL spectra from a 0.15 cm² CdTe/CdS device.

In the present studies, we have used a photomultiplier mounted approximately 7 cm from the solar cell which was mounted on the cold finger of a liquid nitrogen cryostat. Using high (frequency)-pass and low-pass filters we confirmed that the EL detected in this way originates from the 1.35 to 1.6 eV spectral region—the near-band-edge region of CdTe. This system is

much more sensitive and thus permitted detection of the EL signal to much lower current densities.

We find that for temperatures from $-50\text{ }^{\circ}\text{C}$ to $+50\text{ }^{\circ}\text{C}$, the power-law function of current density shown in Equation (1) adequately describes the data. See Figure 4.1.19. Note that for electron and hole injection across the CdS/CdTe junction, electron-hole pair recombination in the depletion region would lead, in first order, to EL intensity proportional to the square of the injected current. The data from this cell at the two temperatures shown yield the exponential, $b = 1.7$ at $24\text{ }^{\circ}\text{C}$ and $b=2.25$ at $-30\text{ }^{\circ}\text{C}$.

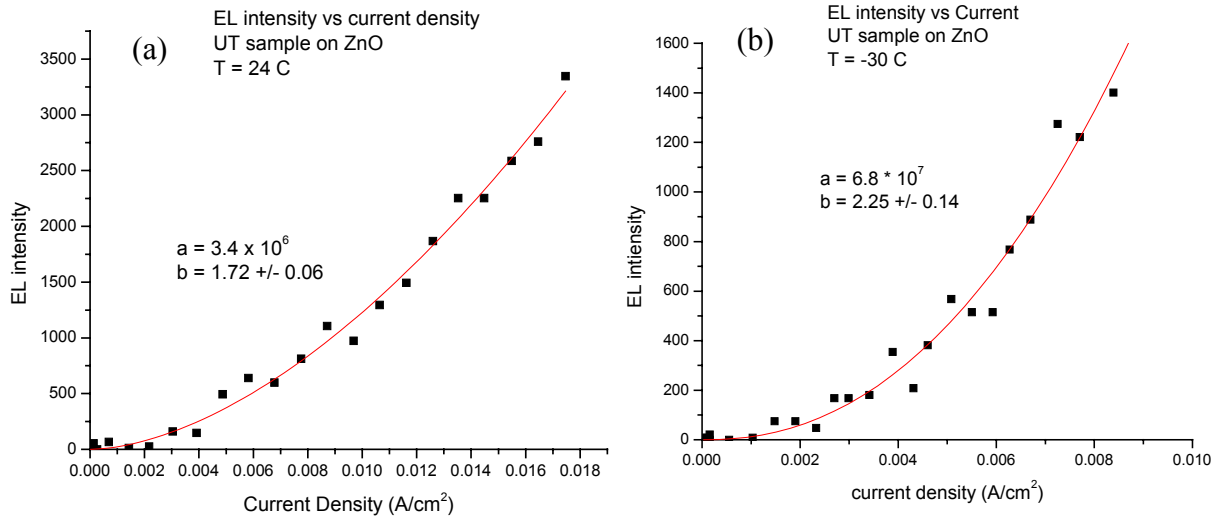


Figure 4.1.19: EL intensity vs current density for a sputtered cell with ZnO TCO a) at $24\text{ }^{\circ}\text{C}$ and b) $-35\text{ }^{\circ}\text{C}$. Note that the amplitude factor, a , increases by x 20 at low temperature and the exponent increases slightly. Lines follow Eq. (1) with fit constants, a and b , shown.

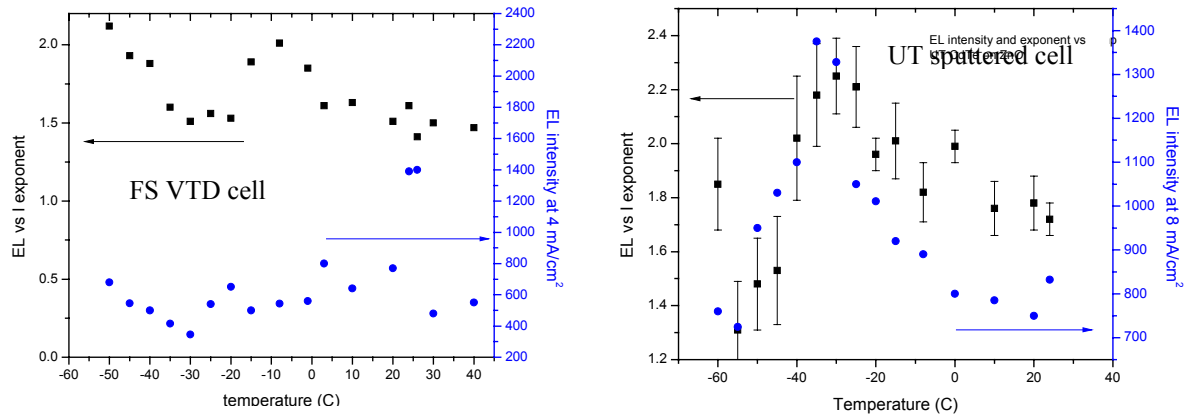


Figure 4.1.20: Exponent b (squares, left abscissas) and EL intensity at constant current (circles, right abscissas) for a 1.1 cm^2 First Solar VTD cell and a 0.15 cm^2 UT cell.

More detailed data on the temperature dependence of both the exponent, b , and the amplitude factor, a , for two different types of cells (sputtered and VTD-deposited) are shown in Fig. 4.1.20. From approximately $-50\text{ }^{\circ}\text{C}$ to $+50\text{ }^{\circ}\text{C}$, the EL intensity at constant current is relatively constant for the VTD cell. The intensity behavior of the sputtered cell is more

complex. From room temperature the intensity increases to a maximum at $-45\text{ }^{\circ}\text{C}$ and then decreases to $-60\text{ }^{\circ}\text{C}$ (see Figure 4.1.20). This is in contrast to the PL from similar samples: PL intensity monotonically increases as the temperature decreases from $+50\text{ }^{\circ}\text{C}$ to $-60\text{ }^{\circ}\text{C}$.

The temperature dependence of the exponent, b , is similarly complex and dependent on the cell type (see Fig. 4.1.20). It is known that as temperature is decreased below room temperature, the effects of a back barrier dominate the I-V performance of CdTe cells.¹⁹ For this reason we have analyzed the data as a function of current density rather than bias voltage, to try to control for the contact influence. However, we cannot at this point exclude the possibility that the temperature dependence is influenced by artifacts of this temperature-dependent back barrier. It is also plausible that some of these effects are related to micrononuniformity effects which may increase in importance at low temperature. Further work is in progress to elucidate these effects.

4.2 Deposition and characterization of ZnO films

ZnO:Al films have been grown with room temperature resistivities in the range 0.3–0.6 m Ω -cm. The resistivity near the edge of the deposition of sample ZO-48 (Fig. 4.2.1) has a temperature dependence which is typical of our samples. The room temperature mobility of this sample is about 43 cm²/V-s with a carrier density of 4.2E+20 /cm³. Since the carrier density changes by less than 5% over the temperature range studied for this sample and shows no detectable trend with temperature, we have assumed a degenerate semiconductor and calculated the mobility using the average value for the carrier density (Fig. 4.2.1). The error bars in mobility are $\pm 5\%$. The mobility appears to be dominated by impurity and/or grain boundary scattering with some evidence of a phonon contribution above about 200 K.

These transport results are similar to those of Zafar, et al²⁰ who were able to achieve, with DC reactive sputtering of ZnO:Al, somewhat lower resistivities ($1.7 \times 10^{-4} \Omega$ -cm), carrier concentrations up to $8 \times 10^{20} \text{ cm}^{-3}$, and mobilities up to 30 cm²/V-s. Pei, et al²¹ similarly found temperature-independent mobility above $\sim 200^\circ\text{C}$ although their DC reactively sputtered films generally had lower carrier density and mobility.

The x-ray diffraction data, taken in a θ -2 θ configuration, show a highly oriented film with c-axis perpendicular to the surface. For growth temperatures from 100 $^\circ\text{C}$ to 350 $^\circ\text{C}$ the 2 θ positions lie within 0.12 degrees of each other showing a lattice constant independent of the glass substrate temperature.

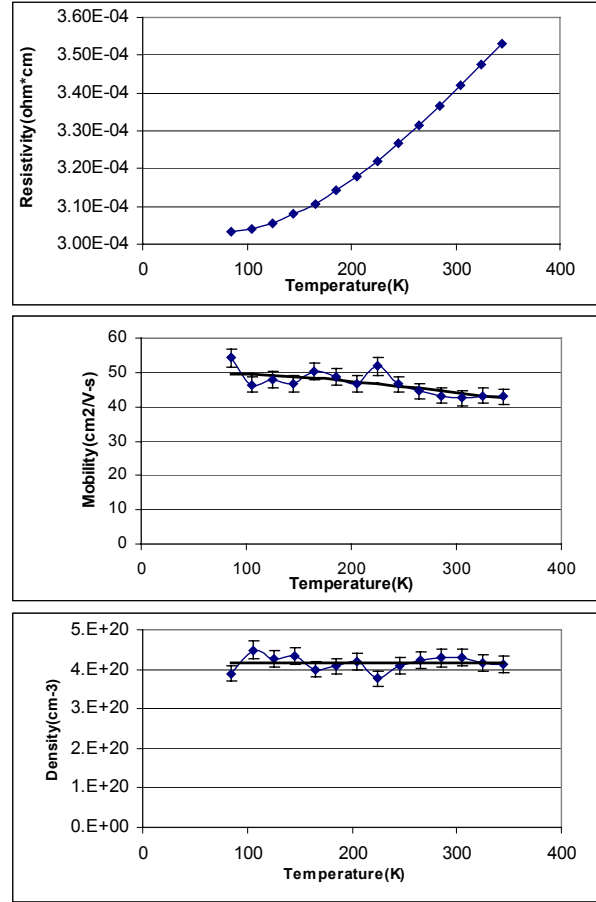


Fig. 4.2.1 Resistivity, mobility, and carrier density of an rf-magnetron-sputtered ZnO:Al film, measured near the edge.

4.3 Admittance spectroscopy

Frequency-dependent capacitance measurements have been extensively used for semiconductor junction analysis.²² Properties such as carrier concentration, density and spatial distribution of traps can be extracted in principle from this type of measurement, depending on the model used for the data interpretation. We performed capacitance measurements on our CdTe solar cells at frequencies ranging between 10^{-1} Hz and 100 kHz and temperatures varying between -25°C and 55°C. The extended range of frequencies allows the study of long-lived deep traps, which are important in understanding the physical processes in CdTe devices.

Our data are consistent with the model where defects have continuous, energy dependent density of states (DOS) in the forbidden gap. We introduce the concept of a single defect capacitance and pay special attention to interpreting the temperature dependence of our data. To ensure the interpretation where DOS is temperature independent we take into account the multiphonon character of the trapping-detrapping electron transitions.

We also apply our techniques to study the effects of degradation on the defect DOS in CdTe device. The DOS was found to change in the course of device degradation. This observation may help to establish the relation between the formation of deep traps and possible degradation mechanisms.

This work was described in more detail in the 1st quarter report and presented at the 29th IEEE PVSC Conference.²³

4.4 Synchrotron x-ray studies of CdTe films

Through a collaborative arrangement with colleagues at the Advanced Photon Source at Argonne National Lab, we have explored the use of the high brightness synchrotron x-ray source for studies of copper doping in CdTe crystals and films. With x-ray absorption near edge structure (XANES) and extended x-ray absorption fine structure (EXAFS) it is possible to obtain information on the lattice location of individual atomic species in crystals and films²⁴ of, e.g., CdTe and CdS. In particular, Drs. Jeff Terry and Nadia Leyarowska of the MR-CAT group at the APS, have assisted us in designing and running experiments that use their beam line and the 13-element high purity germanium detector to study copper in CdTe. This unique facility allows one to study the k-shell x-ray absorption edge of small amounts of Cu in CdTe by monitoring the Cu- k_{α} x-ray fluorescence with the 13-element high purity Ge detector.

The experiments, which are continuing, are designed to study the lattice location(s) of the Cu in CdTe and CdS crystals, films, and solar cells and the changes in these locations which may occur due to CdCl₂ treatment or light-soak stress. An overview of these studies is provided here.

X-ray fluorescence—In the process of setting up the XANES and EXAFS experiment, we found that the Cu- k_{α} fluorescence signal itself could yield a determination of residual levels of Cu in CdTe and related materials used for solar cells. The technique is very sensitive because the synchrotron x-ray beam can be tuned in energy slightly above the Cu k-absorption edge and the Cu fluorescence signal observed with the detectors isolating the k_{α} fluorescence. Examples of the fluorescence spectra are shown in Fig. 4.4.1. The signal at about 9.5 keV is scattered photons from the beam. The k_{α} and k_{β} peaks are seen at 8.0 and 8.7 keV as well as fluorescence from Cd and Te L-shells. Unfortunately, we found that considerable Cu-fluorescence signal can arise from residual copper in glass substrates as well as in surrounding sample holders and other

equipment in the experiment hutch. Thus we have not made a final estimate of residual Cu in our films and CdTe crystals. We are making a comparison of Cu concentrations as determined with this synchrotron x-ray fluorescence method with the more traditional inductively coupled plasma spectroscopy technique which we have available at UT.

The high resolution absorption-edge spectroscopy method used here involves setting an energy window for the Ge detector array at the Cu- k_α fluorescence and scanning the synchrotron-produced x-rays (via the undulator and monochromator) across the Cu-absorption edge from about 8800 to 9100 eV. Examples of XANES absorption spectra are shown in Fig. 4.4.2. The k-absorption edge at about 8980 eV varies with the bonding and near neighbor environment producing distinct fingerprint spectra for Cu in the different materials. We have found that Kapton polyimide film and fused silica are advantageous to use as substrates to avoid significant background signal. We have obtained spectra from several cells and films with and without additional copper. We will be making at least one additional experimental run before final analyses, but the present data indicate that most of the Cu in CdTe films resides in an environment similar to that of the compound Cu_2Te although some changes are observed after CdCl_2 treatments.

One concern about these types of measurements using high fluence x-ray beams is whether the beam itself induces changes in the films and particularly in the bonding arrangement of the Cu in CdTe. To help understand these issues we have compared XANES spectra of a sputtered CdTe film diffusion doped with Cu using a fixed beam spot for the eight hour run and a spectrum obtained by rastering the beam after each datum point (10 sec dwell time). In fact there are some slight differences. Further, after the x-ray measurements we have studied the band-edge photoluminescence (PL) using a Kr laser with PL mapping techniques to search for residual effects of the x-ray irradiation. Again we can observe some changes. These issues are being addressed in the next round of experiments.

We expect to be able to provide an analysis of these effects in the next annual report.

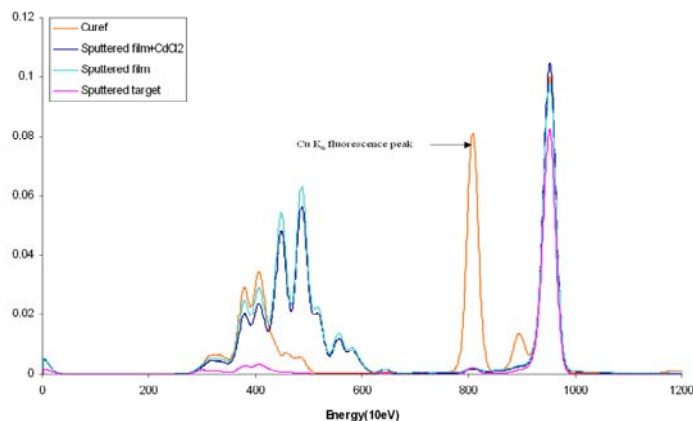


Fig. 4.4.1 Cu k_α fluorescence spectra from a sputtered film before and after treatment with CdCl_2 , from a Cu foil and from a CdTe sputter target.

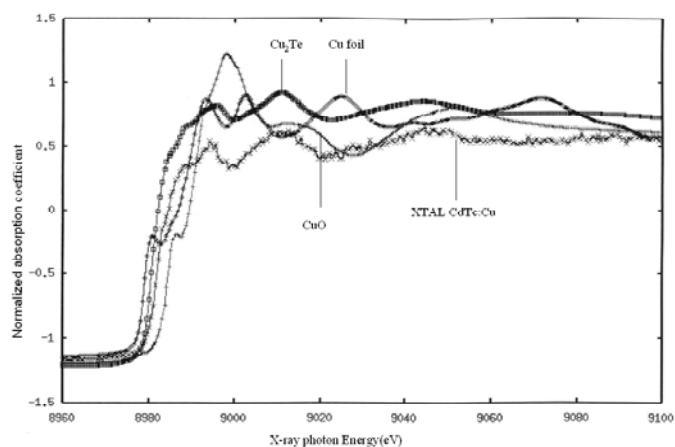


Fig. 4.4.2 XANES absorption spectra of Cu foil, CuO , Cu_2Te , and a Cu-doped CdTe film.

4.5 Laser scribing of stannates

In previous work we have evaluated the suitability of various lasers for scribing of materials involved in thin-film photovoltaics.²⁵ We evaluated the threshold for onset of film damage and also the scribing efficiency in terms of thickness removed per energy per pulse. This earlier work included the evaluation of SnO₂:F and ZnO. Recently we were approached by Dr. Xuanzhi Wu to evaluate the scribing conditions for the stannates, Cd₂SnO₄ and Zn₂SnO₄. This is an overview of that evaluation.

Wu and the NREL group recently used a bilayer structure of cadmium and zinc stannates (Cd₂SnO₄ and Zn₂SnO₄) to fabricate record efficiency (16.5%) CdTe solar cells.²⁶ Thus, in our evaluation, we have studied single layers as well as bilayers. The full range of lasers used earlier was no longer available, but we used two types of pulsed Nd:YAG lasers for the scribing study, one with a long pulse and relatively high repetition rate operating at the fundamental wavelength (Quantronix-416 (1064 nm, 600 ns)), and the other with a short pulse and low repetition rate operating frequency doubled (Molelectron MY 32-10 (532 nm, 12-15 ns)). Results on commercial tin oxide and our own sputtered zinc oxide are provided for comparison.

In previous work, we have found it convenient to identify the threshold for surface damage to provide a point of reference for energy density calibrations. The new results are listed in Table 4.3.1. It should be kept in mind that these TCOs are nominally transparent at the two wavelengths used although the scribing process can initiate from absorption through defect states, through free-carrier absorption, or by non-linear, multiple-photon absorption. Here we are not so much interested in the exact mechanism but rather in providing an empirical measure of the ease of scribing.

Zinc stannate has a fairly high threshold power density (70 J/cm²) at 1064 nm, probably due to a lack of midgap defect states at the laser fundamental (1.17 eV) and very low free carrier absorption. The high conductivity cadmium stannate has a low threshold at 1064 nm and somewhat higher at 532 nm consistent with a free-carrier absorption mechanism. At 532 nm, the threshold value for the bilayer structure is less than half that of either one of the individual stannate films; this may indicate interfacial defects and/or cadmium and zinc intermixing effects.

Table 4.5.1. Surface damage thresholds for stannates.

Material	Sample ID	Sheet resistance (Ω/□)	Thickness (nm)	Laser type and damage threshold	
				1064 nm 600 ns (J/cm ²)	532 nm 15 ns (J/cm ²)
Tin Oxide	TEC - 7	7	500	3	4
Zinc Oxide	ZnO - 16	10	500	3	20
Cadmium Stannate	CTO - 538	15	150	3	10
Zinc Stannate	ZTO - 697	10000	200	70	20
Bilayer	537/699	25	350		4

Highly isolating scribe lines of good morphology were obtained on Cd₂SnO₄ at 1064 nm and on Zn₂SnO₄ and bilayer structures with 532 nm (Table 4.3.2). Profilometer traces show that there are no ridges on the sides of the scribe lines.

Table 4.5.2. Details on scribe lines. (Beam incident on the film side except where noted. Energy density values are for the center of the beam).

Entry #	Material	Laser	Energy density (J/cm ²)	Repetition rate (pps)	Translation speed (mm/s)	Scribe width (μm)	Resistance (across 1.5" line) (kΩ)	Notes
1	Cadmium Stannate	1064 nm, 600 ns	70	100	1.2	40	20	double pass
2	Cadmium Stannate	1064 nm, 600 ns	70	100	1.2	40	100	
3	Zinc Stannate	532 nm, 12 ns	1700	10	0.62	110	>40000	
4	Bilayer	532 nm, 12 ns	1500	10	0.27	120	3000	glass-side
5	Bilayer	532 nm, 15 ns	4	10	0.47	140	>30000	

For glass-side scribing, the laser beam enters the substrate on the side opposite the film. The ablation then begins at the glass-film, not the film-air interface. In this case it is fairly easy to damage the glass (in the form of microcracks) at the focal spot. This happens at energy densities above 30 J/cm². Entries # 1-4 in Table 2 (film-side scribing) were done at the tightest focus conditions (Gaussian beam profile, energy density values for the center of the spot), while for the glass-side scribing (entry #5) the lens was moved 5 mm closer to the sample. The defocusing yielded a “top-hat” profile and much lower required energy density.

We think that either the 1064 nm or 532 nm lasers with pulse durations from 10 to 1000 ns would provide acceptable quality scribing on either of the stannates and on bilayer structures. Since CdTe has a still lower damage threshold (less than 1 J/cm²),²⁶ a self-limiting scribe of the CdTe without harming the stannate TCO should be possible.

References

- ¹ D.H. Levi, L.M. Woods, D.S. Albin, T.A. Gessert, R.C. Reedy, and R.K. Ahrenkiel, presented at the 2nd World Conference on Photovoltaic Solar Energy Conversion, 1998, Vienna, Austria.
- ² V. G. Karpov, A. D. Compaan and Diana Shvydka, Effects of Nonuniformities in Thin-Film Photovoltaics, Appl. Phys. Lett. **80**, p. 4256 (2002).
- ³ V. G. Karpov, A. D. Compaan and Diana Shvydka, Micrononuniformity Effects in CdTe Photovoltaics, To be published in the 29th IEEE PVSC.
- ⁴ T. N. Mamontova and A. V. Chernyshev, “Photoluminescence “fatigue” and structural disorder of As₂Se₃”, Soviet Physics - Semiconductors **18**, pp. 332-333 (1984).
- ⁵ R. Laiho, A. Pavlov, and O. Hovi, T. Tsuboi, “Time dependence and optical quenching of photoluminescence in porous silicon”, Appl. Phys. Lett. **63**, pp. 275-277 (1993).
- ⁶ R.A. Street, “Recombination in amorphous semiconductors”, Phys. Rev. B **17**, pp.3984-3995 (1978).
- ⁷ D. Guidotti, Eram Hasan, H.J. Hovel, and Marc Albert, “Degradation of band-gap photoluminescence in GaAs”, Appl. Phys. Lett. **50**, pp. 912-914 (1987)
- ⁸ M.Y.A. Raja, S.R.J. Brueck, M. Osinski, and J. McInerney, “Laser-induced degradation of GaAs photoluminescence”, Appl. Phys. Lett. **52**, pp. 625-627 (1988).
- ⁹ Diana Shvydka, V. G. Karpov and A. D. Compaan, “Bias-dependent photoluminescence in CdTe photovoltaics”, Appl. Phys. Lett., **80**, 3114-3116, (2002).
- ¹⁰ R. Harju, V. G. Karpov, D. Grecu, G. Dorer, “E-beam induced degradation in CdTe photovoltaics”, J. Appl. Phys., **88**, 1794 (2000).

-
- ¹¹ We appreciate FS, LLC sharing this data for unspecified back contact cell which degradation was tracked for 5 years.
- ¹² A.D. Compaan, X. Deng, and R.G. Bohn. "High Efficiency Thin Film CdTe and a-Si Based Solar Cells," Final Technical Report for the Period, March 4, 1998 to October 15, 2001, Contract No. ZAF-8-17619-14
- ¹³ James Ziegler, SRIM, the Stopping and Range of Ions in Matter, <http://www.srim.org/>
- ¹⁴ S-H. Wei, S.B. Zhang, and A. Zunger, J. Appl. Phys. **87**, 1304 (2000).
- ¹⁵ P.Y. Yu, M. Cardona, *Fundamentals of semiconductors*, Springer-Verlag, Berlin (1996), pp. 333-361.
- ¹⁶ D.G. Thomas, J.J. Hopfield, W.M. Augustiniak, Phys. Rev. **140**, A202 (1965).
- ¹⁷ E. Molva, J.L. Pautrat, K. Saminadayar, G. Milchberg, and N. Magnea, Phys. Rev. B, **30**, 3344 (1984)
- ¹⁸ A. Gupta, A.D. Compaan, K. Price, A. Vasko, K. Hinko, X. Liu, M. Fritts, N. Leyarovska, J. Terry, "Visible and x-ray spectroscopy studies of defects in CdTe," 29th IEEE Photovoltaic Specialists Conference-2002, paper 2O1.3, New Orleans, May 24, 2002. (to be published)
- ¹⁹ A. L. Fahrenbruch, "Modeling results for CdTe solar cells," available at: <http://www.colostate.edu/orgs/pvlab/PDFs/ModCdTe2.pdf>
- ²⁰ S. Zafar, C.S. Ferekides, and D. L. Morel, J. Vac. Sci. Technol. A **13**, 2177 (1995)
- ²¹ Z.L. Pei, C. Sun, M.H. Tan, J.Q. Xiao, D.H. Guan, R.F. Huang, and L.S. Wen, J. Appl. Phys, **90**, 3432 (2001).
- ²² P. H. Mauk, H. Tavakolian, and J. R. Sites, IEEE Transactions of Electron Devices **37**, 1990, p.422.
- ²³ Diana Shvydka, U. Jayamaha, V. G. Karpov, and A. D. Compaan, "Capacitance-Frequency Analysis of CdTe Photovoltaics". To be published in the 29th IEEE PVSC.
- ²⁴ *X-ray absorption : principles, applications, techniques of EXAFS, SEXAFS, and XANES*, edited by D.C. Koningsberger and R. Prins New York, Wiley, c1987
- ²⁵ A.D. Compaan, I. Matulionis, and S. Nakade, "Laser Scribing of Polycrystalline Thin Films," Optics and Lasers in Engineering, **34**, 2000.
- ²⁶ X. Wu, J.C. Keane, R.G. Dhere, C. DeHart, D.S. Albin, A. Duda, T.A. Gessert, S. Asher, D.H. Levi, and P. Sheldon, 17th European Photovoltaic Solar Energy Conference, Munich, Germany, 2001.

5.0 Publications

5.1 Refereed papers published or in press (9/1/01 – 8/31/02):

1. Diana Shvydka, V.G. Karpov, and A.D. Compaan, "Bias-dependent photoluminescence in CdTe photovoltaics," *Appl. Phys. Lett.* **80**, 3114 (2002).
2. Diana Shvydka, A.D. Compaan, and V.G. Karpov, "Nonlocal response in CdTe photovoltaics," *J. Appl. Phys.* **91**, 9059 (2002).
3. V. G. Karpov, A. D. Compaan, and Diana Shvydka, "Effects of nonuniformity in thin-film photovoltaics," *Appl. Phys. Lett.*, **80**, 4256 (2002).
4. J. Drayton, C. Taylor, A. Gupta, R.G. Bohn, G. Rich, A.D. Compaan, B.E. McCandless, and D. Rose, "Properties of reactively sputtered ZnTe:N and its use in recombination junctions," 29th IEEE Photovoltaic Specialists Conference-2002, paper 2O2.6 New Orleans, May 24, 2002. (to be published)
5. A. Gupta, A.D. Compaan, K. Price, A. Vasko, K. Hinko, X. Liu, M. Fritts, N. Leyarovska, J. Terry, "Visible and x-ray spectroscopy studies of defects in CdTe," 29th IEEE Photovoltaic Specialists Conference-2002, paper 2O1.3, New Orleans, May 24, 2002. (to be published)
6. D. Shvydka, U. Jayamaha, V.G. Karpov, and A.D. Compaan, "Capacitance-frequency analysis of CdTe photovoltaics," 29th IEEE Photovoltaic Specialists Conference-2002, paper 2P3.12, New Orleans, May 24, 2002. (to be published)
7. V.G. Karpov, A.D. Compaan, and Diana Shvydka, "Micrononuniformity effects in thin-film photovoltaics," 29th IEEE Photovoltaic Specialists Conference-2002, paper 2P2.14, New Orleans, May 24, 2002. (to be published)
8. Diana Shvydka, A.D. Compaan, V.G. Karpov, "External bias effect on junction photoluminescence in CdS/CdTe solar cells," 29th IEEE Photovoltaic Specialists Conference-2002, paper 2P2.15, New Orleans, May 24, 2002. (to be published)

5.2 Poster or oral presentations published on CDROM and the NREL Web site

1. J. Drayton, C. Taylor, A. Gupta, R.G. Bohn, A.D. Compaan, B.E. McCandless, and D. Rose, "Optical, structural and transport properties of reactively sputtered ZnTe:N," National Center for Photovoltaics Program Review Meeting, Denver, Oct. 14-17, 2001.
2. A.D. Compaan, Diana Shvydka, K.J. Price, A. Vasko, V.G. Karpov, "Bias-dependent Luminescence in CdS/CdTe Cells," National Center for Photovoltaics Program Review Meeting, Denver, Oct. 14-17, 2001.
3. Diana Shvydka, A.D. Compaan, and V.G. Karpov, "Nonlocal Optical Response in CdTe Photovoltaics," National Center for Photovoltaics Program Review Meeting, Denver, Oct. 14-17, 2001.

5.3 Contributed oral or poster presentations (no published manuscript)

1. Xiangxin Liu, Akhlesh Gupta, Alvin D. Compaan (Dept. of Physics and Astronomy, University of Toledo), Nadia Leyarovska (Biological, Chemical, and Physical Sciences,

Illinois Institute of Technology), Jeff Terry (Dept. of Physics, University of Notre Dame), The Materials Research Collaborative Access Team “K-edge EXAFS and XANES studies of Cu in CdTe thin-film solar cells” (Presentation B28.015, Am. Phys. Soc. Mtg, March 2002, Indianapolis, IN)

2. Jennifer A. Drayton, Alvin D. Compaan (The University of Toledo, Department of Physics and Astronomy) “Spectroscopy of molecular nitrogen during reactive sputtering of ZnTe:N” (Presentation C33.156, Am. Phys. Soc. Mtg, March 2002, Indianapolis, IN)
3. Ilvydas Matulionis, Akhlesh Gupta, Jennifer A. Drayton, Alvin D. Compaan “Substrate Configuration Cadmium Telluride Solar Cells” (Presentation H33.106, Am. Phys. Soc. Mtg, March 2002, Indianapolis, IN)
4. Jennifer A. Drayton, Alvin D. Compaan (The University of Toledo, Department of Physics and Astronomy) “Spectroscopy of molecular nitrogen during reactive sputtering of ZnTe:N” (Presentation C33.156, Am. Phys. Soc. Mtg, March 2002, Indianapolis, IN)
5. Ilvydas Matulionis (Dept. of Physics and Astronomy, The University of Toledo, Toledo, Ohio 43606, USA), Akhlesh Gupta, Jennifer A. Drayton, Alvin D. Compaan “Substrate Configuration Cadmium Telluride Solar Cells” (Presentation H33.106, Am. Phys. Soc. Mtg, March 2002, Indianapolis, IN)
6. Brian Sunderland (Colorado College, Colorado Springs, Colorado 80903-3298), Akhlesh Gupta, Alvin D. Compaan (University of Toledo, Department of Physics and Astronomy, Toledo, Ohio 43606-3390) “Nickel Phosphide as a Copper Free Back Contact for CdTe-Based Solar Cells” (Presentation S17.013, Am. Phys. Soc. Mtg, March 2002, Indianapolis, IN)
7. Kathleen Hinko (University of Toledo) “Photoluminescence of magnetron sputtered CdTe films: dependence on target purity, substrate, and annealing conditions,” (Presentation D31.013, Am. Phys. Soc. Mtg, March 2002, Indianapolis, IN)

5.2 Annual Subcontract Reports:

A.D. Compaan, Xunming Deng, and Randy G. Bohn, “High Efficiency Thin Film CdTe and a-Si Based Solar Cells,” final technical report for the period March 4, 1998 to October 15, 2001.

5.3.1 Annual Contract Summary published in U.S. Dept. of Energy Photovoltaic Energy Program Contract Summary, FY 2001 :

A.D. Compaan and V.G. Karpov, “The Fabrication and Physics of High Efficiency Cadmium-Telluride Thin-Film Solar Cells.”

6.0 Project Personnel

6.1 Research professor/summer faculty visitor

Akhlesh Gupta (Ph.D. Indian Institute of Technology, Delhi)(50% time, 9/1/01--)
Kent Price (Ph.D., U. of North Carolina) (6/01-7/01)

6.2 Postdoctoral Associates:

Shanli Wang (Ph.D. Shanghai Inst. Of Technical Physics, 97)(6/02--)(50% time)
Diana Shvydka (Ph.D., U. of Toledo, 5/2002)(9/02--)

6.3 Graduate Students (with Principal Advisor)(some students received support from other sources but made significant contributions to this work):

Ilvydas Matulionis (Compaan)
M.S. completed 1997 (non thesis)
Ph.D. May 2002 “Sputter Deposition and Laser Integration of Thin-Film Solar Cells”

Diana Shvydka (Compaan)
M.S. completed 1999 (non thesis)
Ph.D. May 2002 “Physical Characterization of CdTe/CdS Photovoltaics: defects, Fields, and Micrononuniformities”

Jennifer Drayton (Compaan)
Ph.D. in progress

Catherine Taylor (Bohn)
M.S. in progress

Yujun Chen (Karpov)
M.S. in progress

Yuriy Sosov (Karpov)
Ph.D. in progress

Xiangxin Liu (Compaan)
M.S. and Ph.D. in progress

Todd Osborn (Giolando)
M.S. and Ph.D. in progress

Anthony Vasko (Compaan)
M.S. and Ph.D. in progress

Viral Parikh (Compaan)
M.S. and Ph.D. in progress

Karthikeya Allada (Compaan)
M.S. and Ph.D. in progress

6.4 Undergraduate students

Levi Gorrell, part-time during academic years 01-01 and 02-03

NSF Research Experiences for Undergraduates (REU) Summer 2002:

Levi Gorrell, Univ. of Toledo “Electroluminescence with CdTe Solar Cells”

Melissa Haugen, Gustavus Adolphus College “Raman Scattering in Thin Films”

Christopher Verzella, College of New Jersey “PL Degradation across the CdTe/CdS
Junction in CdTe Solar Cells”

6.5 Technical Assistants

Robert Burmeister (4/96-) (25% time)

Matt Fritts (10/01—9/02) (50% time)